

Active Control of High Reynolds Number Supersonic Jets Using Plasma Actuators

Professors Mo Samimy and Igor Adamovich
Department of Mechanical Engineering
The Ohio State University
GDTL/AARL/OSU
Columbus, Ohio 43235
samimy.1@osu.edu
614-292-5012
614-292-5552 (Fax)

Final Report
FA9550-07-1-0173
March, 2007 – November 30, 2009

February 2010

Report Documentation Page			Form Approved OMB No. 0704-0188		
Public reporting burden for the collection of information is estimated to average 1 hour per response, including the time for reviewing instructions, searching existing data sources, gathering and maintaining the data needed, and completing and reviewing the collection of information. Send comments regarding this burden estimate or any other aspect of this collection of information, including suggestions for reducing this burden, to Washington Headquarters Services, Directorate for Information Operations and Reports, 1215 Jefferson Davis Highway, Suite 1204, Arlington VA 22202-4302. Respondents should be aware that notwithstanding any other provision of law, no person shall be subject to a penalty for failing to comply with a collection of information if it does not display a currently valid OMB control number.					
1. REPORT DATE 04 FEB 2010		2. REPORT TYPE		3. DATES COVERED 01-03-2007 to 30-11-2009	
4. TITLE AND SUBTITLE Active Control of High Reynolds Number Supersonic Jets Using Plasma Actuators			5a. CONTRACT NUMBER		
			5b. GRANT NUMBER		
			5c. PROGRAM ELEMENT NUMBER		
6. AUTHOR(S)			5d. PROJECT NUMBER		
			5e. TASK NUMBER		
			5f. WORK UNIT NUMBER		
7. PERFORMING ORGANIZATION NAME(S) AND ADDRESS(ES) Department of Mechanical Engineering, The Ohio State University, GDTL/AARL/OSU, Columbus, OH, 43210-1016			8. PERFORMING ORGANIZATION REPORT NUMBER		
9. SPONSORING/MONITORING AGENCY NAME(S) AND ADDRESS(ES)			10. SPONSOR/MONITOR'S ACRONYM(S)		
			11. SPONSOR/MONITOR'S REPORT NUMBER(S)		
12. DISTRIBUTION/AVAILABILITY STATEMENT Approved for public release; distribution unlimited					
13. SUPPLEMENTARY NOTES					
14. ABSTRACT					
15. SUBJECT TERMS					
16. SECURITY CLASSIFICATION OF:			17. LIMITATION OF ABSTRACT Same as Report (SAR)	18. NUMBER OF PAGES 64	19a. NAME OF RESPONSIBLE PERSON
a. REPORT unclassified	b. ABSTRACT unclassified	c. THIS PAGE unclassified			

Table of Contents

Active Control of High Reynolds Number	1
ABSTRACT.....	3
1. INTRODUCTION.....	4
1.1 Jet instabilities.....	4
1.2 Heated jet	5
1.3 Objectives of the research	6
2. EXPERIMENTAL FACILITY AND TECHNIQUES	8
2.1 Nozzle and Air Supply System	8
2.2 Boundary Layer Conditions near the Nozzle Exit	9
2.3 Plasma Actuator	11
2.4 Flow Field Measurements.....	11
3. RESULTS.....	14
3.1 Mach 0.9 Cold Subsonic Jet.....	14
3.1.1 Effects of Duty Cycle of Input Signal.....	14
3.1.2 Effects of Forcing Strouhal Number on Overall Jet Spreading	16
3.1.3 Effects of Azimuthal Mode.....	19
3.1.4 Effects Forcing on Turbulence Statistics	21
3.1.5 Vortex Dynamics and Its Role in the Jet Development.....	23
3.1.6 Convection Velocity of Large-Scale Structures	29
3.2 Mach 1.3 Cold Supersonic Jet	30
3.2.1 Effects of Forcing Strouhal Number on Overall Jet Mixing.....	31
3.2.2 Effects of azimuthal modes.....	35
3.2.3 Effects of Forcing on Turbulence	39
3.2.4 Large-Scale Structures and their role in the Jet Development.....	40
3.3 Mach 0.9 Heated Subsonic Jet.....	48
3.3.1 Mean Flow Results	48
3.3.2 Conditionally-Averaged Results	52
3.4 Mach 1.65 Cold Jet	58
4. CONCLUDING REMARKS	60
REFERENCES.....	62

ABSTRACT

Active flow control of jets with Localized Arc Filament Plasma Actuators (LAFPA) is conducted over a wide range of the fully expanded jet Mach numbers (M_J or simply jet Mach number). The jet Mach numbers covered in the present research are 0.9 (with a converging nozzle), 1.2 (overexpanded), 1.3 (perfectly expanded), and 1.4 (underexpanded) with a design Mach number 1.3. Additionally, limited experiments are carried out for an $M_J = 1.65$ perfectly-expanded jet. The exit diameter is 2.54 cm (1 inch) for all cases and eight LAFPA are equally distributed on the perimeter of a boron nitride nozzle extension. The jet spreading is strongly dependent on duty cycle, forcing frequency, and azimuthal modes. The performance of LAFPA for jet spreading is investigated using two-dimensional particle image velocimetry (PIV). There is an optimum duty cycle, producing maximum jet spreading, for each forcing frequency. A relationship between the optimum duty cycle and forcing frequency is determined from the extensive results in the M_J 0.9, and this relation is used for all experiments. The effect of forcing frequency is investigated for a wide range of forcing Strouhal numbers ($St_{DF} = f_F D / U_e$, where f_F , D , and U_e , are forcing frequency, nozzle exit diameter, and jet exit velocity respectively), ranging from 0.09 to 3.0. The azimuthal modes (m) investigated are $m = 0 - 3, \pm 1, \pm 2$, and ± 4 - this comprises all modes available with eight actuators. The performance of LAFPA does also strongly depend on the stagnation temperature of the jet and M_J . The effects of stagnation temperature are investigated for 1.0, 1.4, and 2.0 times the ambient temperature in M_J 0.9 jet for very limited azimuthal modes and St_{DF} . In an M_J 1.65 perfectly-expanded jet, the control authority of LAFPA is investigated for only $m = \pm 1$ and $St_{DF} \sim 0.3$.

The jet spreading increases with decreasing duty cycle until the limit of incomplete breakdown is reached. Thus, the optimum duty cycle is the lowest value, at a given forcing frequency, which ensures complete breakdown. Extensive experiments in M_J 0.9 and 1.3 perfectly-expanded jets show that the jet spreading is greatest at about $St_{DF} = 0.3$ for most azimuthal modes. The most and least effective azimuthal modes for mixing enhancement are $m = \pm 1$ and ± 4 , respectively. The results also show that the effect of forcing is very similar in M_J 0.9 subsonic and 1.3 perfectly-expanded supersonic jets. The results in the heated M_J 0.9 jet show that the effects of forcing increase with increasing stagnation temperature. In addition, the jet spreading in $m = 0$ is comparable to that in $m = 1$ at an elevated stagnation temperature while it was one of the less effective modes in an unheated jet. The turbulent kinetic energy along the jet centerline also increases significantly near $St_{DF} = 0.3$ for most azimuthal modes.

In off-design conditions of $M_J = 1.2$ and 1.4, the forcing is less effective compared to the perfectly-expanded case of $M_J = 1.3$. Flow structure visualization, using Galilean streamlines, shows that there are naturally-amplified flow structures (generated by a natural feedback mechanism in the over- and under-expanded jets) in addition to the structures generated by forcing. The competition of these structures seems to be responsible for the reduced effectiveness of forcing. The performance of LAFPA in a high M_J supersonic jet ($M_J = 1.65$) shows reduced forcing effectiveness. It has not yet been conclusively determined if the reduction in effectiveness is due to the lack of LAFPA control authority or increased flow compressibility.

1. INTRODUCTION

Many researchers have worked on jet flow control to enhance mixing and/or reduce noise. Most of the earlier jet flow control was done in low-speed and low Reynolds number flows. In such flows, acoustic drivers were successfully used since the flow momentum and associated flow characteristic frequency are low. However, the acoustic driver does not have sufficient bandwidth and amplitude in high-speed and high Reynolds number flows, since characteristic flow frequency and flow momentum increase as the jet speed and Reynolds number rise.

1.1 Jet instabilities

The most successful manipulation of the jet flow is related to controlling the jet characteristic instabilities. There are two major instability modes in a jet: the initial shear layer instability and the jet column instability. These modes are based on two length scales in a free jet: the initial boundary layer momentum thickness (θ) at the nozzle exit and the nozzle exit diameter (D) for a circular nozzle or the nozzle exit height (h) for a rectangular nozzle. The initial shear layer instability frequency is scaled with the momentum thickness (θ) at the nozzle exit. The jet column instability or the jet preferred mode is the instability around the end and downstream of the potential core, and its frequency is scaled with the nozzle exit diameter (D) or height (h). The corresponding Strouhal numbers are $St_\theta (= f\theta/U_j)$ and $St_D (= fD/U_j)$ for initial shear layer instability and jet column mode, respectively. The f and U_j are instability wave frequency and the jet exit velocity, respectively.

The shear layer of an unforced jet in the vicinity of the nozzle exit is very thin so that its behavior is very similar to that in a planar shear layer, since curvature effects are negligible. The mixing layer near the exit of the jet is referred as initial shear layer. In the initial shear layer, the maximum amplification of disturbances seems to occur around the Strouhal number ($St_\theta = f\theta/U_j$) of 0.012 in unforced jets [Zaman and Hussain 1981], while the maximum amplification rate of disturbances occur around $St_\theta = 0.017$ [Freymuth 1966, Michalke 1965] in forced jets. The input excitation amplitude required to control this instability in low-speed flows is very small and linear instability analysis has been used extensively to explore various aspects of this instability [Michalke 1965]. When the initial shear layer is forced, the increased amplification rate leads to earlier saturation of amplification and breakdown of amplified instability waves/vortices into smaller scales so that the amplification of instability is smaller than that in unperturbed jets [Zaman and Hussain 1981]. Thus, turbulence intensity in the downstream region can be reduced when the initial shear layer is forced at $St_\theta = 0.017$. However, the growth of instability at $St_\theta = 0.012$ leads to the large scale structures in the shear layer of the jet, which are responsible for the entrainment of ambient air into the jet and gross mixing with the jet fluid.

The maximum amplification of the jet column instability occurs over a wide range of St_D from 0.2 to 0.6 [Crow and Champagne 1971; Gutmark and Ho 1983; Ho and Huerre 1984; Cho et al. 1998], depending heavily upon the experimental facility as well as on what is measured and where it is measured. This is presumably due to the variations in the naturally occurring disturbances in the facilities. The jet column mode can be excited directly by forcing the mode with high enough amplitude [Cho et al. 1998].

The initial shear layer instability and the jet column mode can be coupled when the boundary layer at the nozzle exit is laminar [Ho and Hsiao 1983]. The coupling occurs through an integer number (usually 3 or 4) of pairings of relatively small structures in the initial shear layer. Kibens [1980] also

observed a coupling of these two modes in a forced jet with an acoustic driver. However, the Strouhal number along the lip-line of the jet was not stepwise, but smoothly changed. This suggests that the pairing did not occur in an orderly manner so that the coupling of the two modes perhaps did not happen [Ginevsky, et al. 1974]. Based on earlier results in Mach 0.9 subsonic [Kim et al. 2009a] and Mach 1.3 supersonic [Samimy et al. 2007b] jets, it seems that the jet column mode is directly forced by the LAFPA's.

In addition to the two instability modes discussed above, there is azimuthal mode instability in a circular jet. The jet column instability is unstable to azimuthal or helical modes [Cohen & Wygnanski 1987]. The major factor deciding the growth rate and amplitude of various azimuthal modes seems to be the ratio of the jet nozzle exit diameter to the boundary layer momentum thickness at the nozzle exit (D/θ_0). Linear stability analysis of Michalke [1977] and Plaschko [1979] and experimental work of Cohen and Wygnanski [1987], Corke, Shakib, and Nagib [1991], and Corke and Kusek [1993] showed that for large D/θ_0 ($D/\theta_0 \gg 1$), both axisymmetric ($m=0$) and the first spinning or helical modes ($m=+1$ or -1) are unstable in the initial jet shear layer. Linear stability analysis of Cohen and Wygnanski [1987] also showed that for a very thin boundary layer (or very large D/θ_0), many azimuthal modes are unstable in the initial shear layer region. Linear stability analysis of Michalke [1977] also showed that further downstream in the jet, where the velocity profile is bell-shaped, the jet can only support helical modes. It has also been reported that the growth region of helical modes move further upstream towards the nozzle as the jet velocity increases [Ho and Huerre, 1984]. A more detailed discussion on the instability related to a circular jet is found in Samimy et al. [2007b].

1.2 Heated jet

Previous work on control of heated jets has focused on characterizing the changes in the flow affected by varying the temperature of the jet. It has been observed that jet total temperature is an independent parameter governing the changes in turbulent boundary layer integral characteristics (e.g. displacement thickness, etc.) in addition to jet exit Reynolds number over the range examined in those experiments (280,000 - 1,400,000) [Lepicovsky 1990]. When the boundary layer of a low Reynolds number ($\sim 10,000$) heated jet transitions from turbulent to laminar, the mixing characteristics change dramatically [Strykowski and S. Russ 1992]. Lepicovsky [1986] experimented with acoustically excited heated jets concluding that: jet sensitivity to upstream acoustic excitation varies strongly with the jet operating conditions, excitation threshold level increases with increasing jet temperature, and jet preferred mode Strouhal number does not change significantly under varying conditions. In a comparison of Mach 0.3 and Mach 0.8 jets, it was concluded that the higher Mach number jet achieved natural excitation due to heating and suggested that larger external forcing amplitudes would be required to observe any excitation effects [Ahuja et al. 1986]. This study also noted that the trend observed in their experiments is contradictory to theory [Ahuja et al. 1982] which states that excitation effectiveness should increase with temperature. Turbulent boundary layers are less selective (compared to laminar) about optimum excitation frequency [Lepicovsky 1989]. Based on these previous works LAFPA's may have an advantage over previous actuators that ideally positions LAFPA's to investigate excitation in heated jets. One disadvantage is that, at least at the present time, there is no mechanism for directly controlling the forcing amplitude of LAFPA's so an increase in excitation threshold would only be noticed if the threshold exceeded the forcing amplitude required to control the jet.

When the jet is heated while maintaining a constant stagnation pressure (constant Mach number), the Reynolds number ($Re = \rho U_j D / \mu$) decreases. The equations used to calculate the Reynolds number are: the ideal gas law, isentropic compressible flow relations, and Sutherland's formula for viscosity. Thus, for the relevant values of $D = 2.54$ cm and $M_j = 0.9$ for these experiments, Reynolds number has the following relationship:

$$Re(T_o) = 1.515 \times 10^{10} \times T_o^{-2} + 1.302 \times 10^8 \times T_o^{-1} \quad (1)$$

where T_o is the stagnation temperature in Kelvin. For example: $Re(290) \approx 630,000$ and $Re(580) \approx 270,000$ correspond to a temperature ratio of about 1.0 and 2.0, respectively. Consequently, as the stagnation temperature rises, the Reynolds number could become sufficiently small for the boundary layer at the nozzle exit to potentially become transitional or laminar.

Another way in which heated jets may differ from unheated jets is the effect of density gradients. The density ratio between the core and the ambient air could affect the nature of jet instabilities. Studies of density gradient phenomena to this point have focused on much lower Reynolds numbers (typically a few thousand) and lower speeds than those in this paper, but the concepts may still be applicable. In a jet with sufficiently large density ratio, there could be a region of absolute instability leading to jet global instability. This instability exists in addition to the initial shear layer and jet column instabilities discussed previously. If a sufficiently large region becomes absolutely unstable, the jet may become globally unstable displaying oscillatory behaviors [Huerre and Monkewitz 1990]. Large, axially symmetric oscillations in the potential core region of jets with density ratio ($S = \rho_j / \rho_{amb}$) less than 0.72 (temperature ratio above 1.39) with a characteristic Strouhal number of ~ 0.3 have been observed [Huerre and Monkewitz 1990, Monkewitz et al. 1990]. Jendoubi and Strykowski [1994] used simulations to explore how these instabilities change with Mach number, co- and counter-flow, and shear layer thickness. It was concluded that increasing Mach number decreases the level of instability. This increase in stability is supported by the observation that the region of absolute instability shrinks from $S < 0.7$ for incompressible to $S < 0.2$ at Mach 0.6. Soteriou and Ghoniem [1995] reported on numerical simulations of density ratios in shear layers on the range 0.33 – 4.0, which showed that as the density ratio decreases: convective velocity slows, entrainment increases, and growth rate increases. In short, the flow becomes biased towards the denser fluid. A fairly exhaustive list of additional studies can be found in the work of Lesshafft et al [2007].

1.3 Objectives of the research

The objectives of the present research are multifaceted and related to these questions:

- 1) Does the plasma actuator, to be described later, have control authority in high-speed and high-Reynolds number jets?
- 2) What are the major parameters which significantly affect the jet flow?
- 3) Do the actuators have the same control authority in off-design conditions?
- 4) Are the actuators more or less effective in heated jets?
- 5) What is the range of jet Mach numbers where the actuator has control authority?

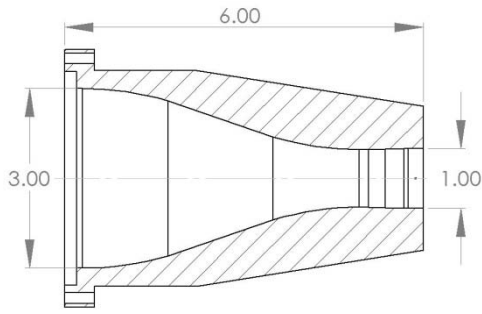
Extensive experiments are carried out to find answers for 1) and 2) in M_j (fully expanded jet Mach number) 0.9 subsonic and M_j 1.3 perfectly-expanded supersonic jets over a wide range of forcing frequencies and all available azimuthal modes. To find answers for 3), experiments are conducted in off-

design conditions of M_j 1.2 (overexpanded) and 1.4 (underexpanded). Based on the results and conclusions of M_j 0.9 and 1.3 jets, very limited experiments are carried out to answer questions 4) and 5) in heated M_j 0.9 and unheated M_j 1.65 jets, respectively.

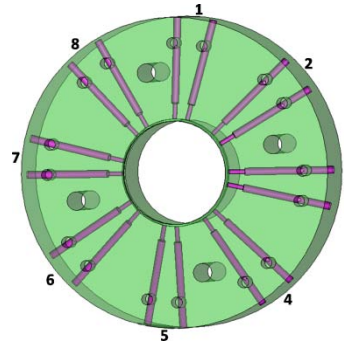
2. EXPERIMENTAL FACILITY AND TECHNIQUES

2.1 Nozzle and Air Supply System

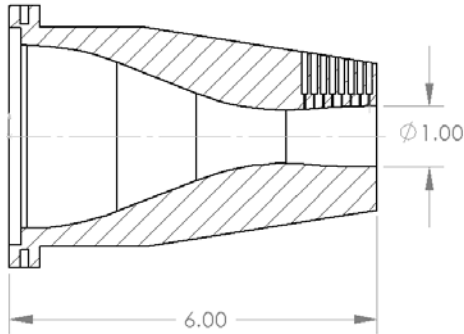
All the experiments are conducted at the Gas Dynamics and Turbulence Laboratory at the Ohio State University. The compressed air, which is filtered and dried, is stored in two cylindrical tanks with a capacity of 43 m³ up to 16 MPa. The compressed air by three five-stage compressors is supplied to the storage tank and then to the stagnation chamber of the jet. The air is then discharged through a nozzle with 1.0" (2.54 cm) exit diameter. Three nozzles are used to cover M_j 's from 0.9 to 1.65. A convergent nozzle is used for Mach 0.9 jets, and a design Mach (M_d) 1.3 converging-diverging nozzle is used for supersonic jets in perfectly expanded ($M_j = 1.3$) and imperfectly expanded conditions ($M_j = 1.2$ and 1.4). Shown in Fig. 2.1a is the streamwise cross-section of M_d 1.3 nozzle, which has very a smooth converging section designed by the method of characteristics to obtain shock-free uniform exit velocity. Mach 0.9 nozzle has a relatively rapid converging section compared to the Mach 1.3 nozzle (drawing is not shown). For the $M_j = 1.65$ jets, either contoured or conical (military application) nozzle is used as shown in Fig. 2.1.



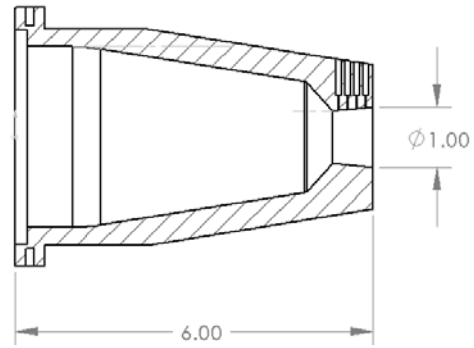
(a) M_d 1.3 contoured nozzle



(b) Boron nitride nozzle extension



(c) M_d 1.65 contoured nozzle



(d) M_d 1.65 conical nozzle

Fig. 2.1 Schematic of M_d 1.3 and 1.65 nozzles and nozzle extension (units are in inch).

At the end of the nozzle, a boron nitride nozzle extension is attached to house eight plasma actuators, uniformly distributed in azimuthal direction (Fig. 2.1b). Each actuator is composed of two tungsten pin electrodes with a diameter of 1 mm. The center-to-center distance of two electrodes is about 4 mm at the tip. All electrodes are placed 1 mm upstream of the extension exit within a ring groove, measuring 1 mm wide and 0.5 mm deep, to prevent the plasma from being blown off. As shown in Fig.

2.1, the electrodes are installed radially and the tip of each electrode is flush-mounded to the inner surface of the nozzle extension.

Table 1 shows the fully expanded jet Mach number (M_J , Mach number based on the ratio of the stagnation pressure to ambient pressure) and corresponding nozzle pressure ratios relative to the ambient pressure. For the M_d 1.3 nozzle, the jet is either perfectly-expanded ($M_J=1.3$), over- ($M_J=1.2$), or under- ($M_J=1.4$) expanded. The M_d 1.65 nozzles are operated only at the design Mach number. However, the flow at the nozzle exit for the conical nozzle is not perfectly expanded due to its conical diverging section. The effects of the stagnation temperature of the jet are investigated only at $M_J = 0.9$ with stagnation temperature ratios (T_o/T_a , T_o = stagnation temperature, T_a = ambient temperature) of 1.0, 1.4 and 2.0. The Reynolds number at the nozzle exit is also shown in Table 1. The Reynolds number ($Re_D = \rho U_e D / \mu$) is based on the nozzle exit diameter (D) and velocity (U_e), and also on density (ρ) and dynamic viscosity (μ) at the nozzle exit.

Table 1 Fully expanded jet Mach numbers and corresponding nozzle pressure ratios.

Nozzle	Fully expanded jet Mach number (M_J)	Nozzle Pressure Ratio (stagnation pressure / ambient pressure)	Stagnation temperature ratio (T_o/T_a)	Reynolds number (Re_D)
Convergent nozzle	0.9	1.69	1.0	0.63×10^6
			1.4	0.41×10^6
			2.0	0.27×10^6
Design Mach 1.3 Converging-diverging nozzle	1.2	2.42 (Over-expanded)	1.0	1.1×10^6
	1.3	2.77 (Perfectly expanded)	1.0	1.2×10^6
	1.4	3.18 (Under-expanded)	1.0	1.4×10^6
Design Mach number 1.65	1.65	4.58 (perfectly expanded)	1.0	16.8×10^6

The heating system is composed of a Watlow 15 kW electric heater and a vertical heat storage tank. The heat storage tank is a 3.5 m (138 in.) tall by 0.3 m (12 in.) diameter cylinder packed with four sets of vertically aligned rows of stainless steel plates. An electric fan takes room air, passes it through the electric heat chamber, through the heat storage tank, and discharges it outdoors. The electric heater has a maximum output temperature of 866 K (1100 °F) which produces a maximum jet stagnation temperature of ~775 K due to heat loss in the storage system. During experiments, pressurized air is forced through the heat storage tank to be heated before entering the jet stagnation chamber. The Mach 0.9 jet experiments can be run continuously for approximately 40 minutes with minimal temperature variation ~0.2 K/min. This system is limited, not by a maximum flow rate, but by how long the storage tank can maintain a stable temperature.

2.2 Boundary Layer Conditions near the Nozzle Exit

As discussed earlier, the condition of boundary layer near the nozzle exit plays a significant role in the jet development and jet instabilities. Due to the small diameter of the nozzle and very thin boundary layer at the nozzle exit, even the simplest questions about the boundary layer are nearly impossible to answer with PIV measurements. In order to address this issue, a slightly larger converging nozzle with 3.81 cm (1.5 in.) diameter was used to examine the boundary layer characteristics of this experimental setup. Apart from the change in diameter, the nozzle used in this experiment is essentially identical to the

nozzle used for the PIV results. A slightly larger nozzle diameter was chosen to maximize the number of measurement points obtained in the boundary layer while remaining sufficiently similar to the primary nozzle. Additionally, a slightly larger diameter allows access to Reynolds numbers (based on nozzle exit diameter) typical of the operating conditions in the unheated jet case while avoiding the compressibility complications at higher velocities. Since hot-wire measurements are very difficult to obtain in a hot jet, the decision was made to assume that any significant changes in the boundary layer characteristics should be, at least primarily, dependent on Reynolds number. The free shear profile just downstream of the nozzle was measured in an unheated jet over a range of Reynolds numbers from 200,000 to 600,000 created by varying the Mach number of the jet.

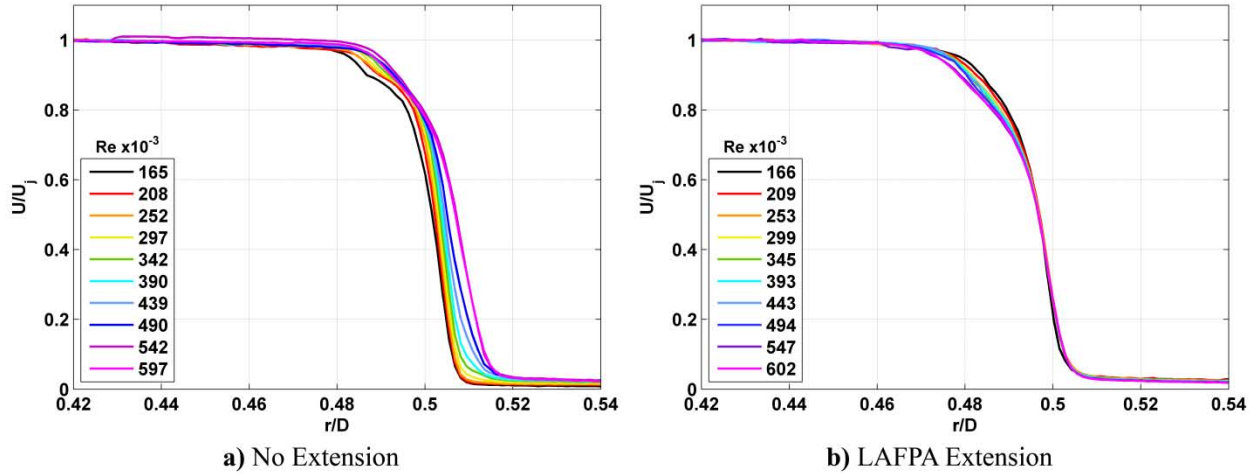


Fig. 2.2 Normalized free shear layer velocity profiles for a range of Reynolds numbers.

The normalized velocity profiles for the two most informative cases are shown in Fig. 2.2. The abscissa is the radial jet coordinate normalized by the jet diameter. Before proceeding any further, the effects of the thick lipped nozzle should be noted. The comparatively large outer diameter of the nozzle lip (~3 in.) creates a recirculation region which acts to widen the diameter of the jet as determined by the hot-wire data. Additionally, the wake profile typical of thin lipped nozzles is completely absent. Without a nozzle extension (Fig. 2.2a), the normalized velocity profiles do not collapse – indicating transitional behavior in the boundary layer. As Reynolds number increases, the profile pushes outward and the sloped decreases.

However, when a nozzle extension is attached (Fig. 2.2b), the profiles collapse very well. The only appreciable change with increasing Reynolds number is a slight decrease in the curvature of the high velocity shoulder. The consistency of the profile is evidence of a consistently turbulent boundary layer. Additionally, the extension slightly decreases the effective jet diameter. Through experimentation with different nozzle extensions (not shown), it was established that the collapse is caused by either the slight trip created by the mating surfaces between the nozzle and the nozzle extension or the additional distance provided by extension. In reality, both features probably contribute.

Since these profiles are of shear layers, not traditional boundary layers, it was decided to estimate the momentum thickness by fitting the profiles to a hyperbolic tangent as performed by Bechert and Stahl [1988]. The slope of the fitted profile is used as the slope of a line. The horizontal distance (Δ) between

where that line crosses one and zero is related to the momentum thickness (θ) as $\Delta = 4\theta$. The momentum thickness of the LAFPA extension case was determined to be ~ 0.09 mm with a variation of ~ 0.01 mm over the range of Reynolds numbers. The case without an extension had momentum thicknesses ranging from ~ 0.05 to ~ 0.09 mm. Previous work by Lepicovsky [1999] reports similar values for the momentum thickness of turbulent boundary layers over this range of Reynolds numbers in a 5.08 cm (2 in.) jet. From the profiles shown in Fig. 2.2b, the best estimate for the boundary layer thickness, ~ 1.2 mm, was calculated as the distance from the nozzle lip ($r/D = 0.5$) to 98% of the free-stream velocity.

2.3 Plasma Actuator

The plasma generating system, shown in Fig. 2.3, has two high voltage Glassman DC power supplies, with output of 10 kV and 1 Ampere. Each power supply can drive four actuators simultaneously, and thus up to eight actuators can be operated at the same time. Each actuator is controlled independently by a Behlke high voltage transistor switch. A National Instruments (NI) analog board attached to a PC is used to generate eight independent, continuous pulse trains to control the transistor switches. Details of the plasma system are provided in Utkin et al. [2007] and in Samimy et al. [2007b].

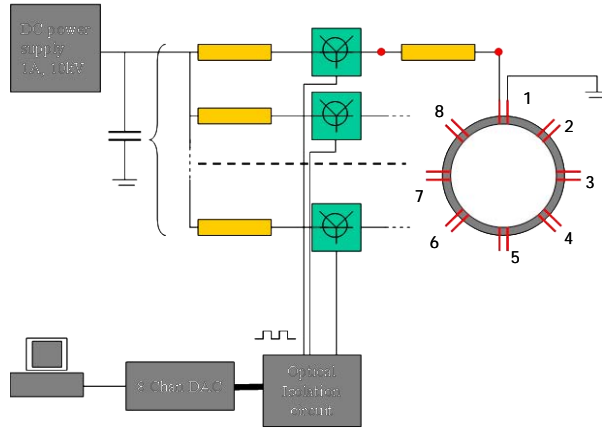


Fig. 2.3 Schematic of the in-house fabricated 8-channel plasma generator.

The forcing frequency, duty cycle, and azimuthal mode are controlled through LabView, NI software. The available azimuthal modes with eight actuators are $m = 0-3, \pm 1, \pm 2$, and ± 4 , where m indicates azimuthal mode. A detailed description of the azimuthal modes is in Kim et al. [2009a]. Although experiments are conducted for all these modes, more extensive results for $m = 0, 1$, and ± 1 will be presented since these modes were representative in $M_j = 0.9$ jets [Kim et al. 2009a]. The forcing Strouhal number ($St_{DF} = f_F D / U_e$, f_F is forcing frequency) ranges from 0.07 to 3.0, covering the jet column mode instability and the lower end range of the initial shear layer instability. The jet exit velocity is used in calculating the forcing Strouhal numbers for all jet Mach numbers, and its value varies due to variation of the stagnation temperature.

2.4 Flow Field Measurements

The jet velocity field is measured by a LaVision PIV system using either one or two cameras with 2048x2048 pixel resolution. A Spectra Physics Model SP-400 dual-head Nd:YAG laser is used for the light source. The cameras and laser are synchronized by a timing unit housed in a dual-processor PC. The

setup for the PIV and the flow visualization is the same and is depicted in Fig. 2.4. The spatial resolution of the velocity vectors depends on the field of view, and the number of pixels used. For the most of streamwise velocity field measurements, the spatial resolution is about 2.2 - 2.5 mm.

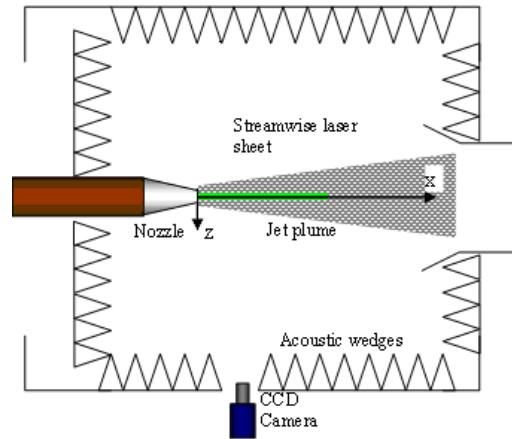


Fig. 2.4 Schematic of the jet and the optical diagnostics set up at GDTL. Y-coordinate is normal to the plane.

The cold jet plume is seeded with Di-Ethyl-Hexyl-Sebacat (DEHS) liquid droplets atomized by a four jet LaVision atomizer. However, it is not possible to seed the heated jet plume with liquid droplets as the high temperatures of the jet evaporate the droplets, and so it is necessary to use an alternative seeding technique. The seeding used in heated jets is aluminum oxide particulates suspended in ethanol, a technique developed and used by Wernet & Wernet [1994]. The particles have a mean diameter of $0.6\ \mu\text{m}$ in a 0.02% concentration by weight. A stable suspension is possible because the aluminum oxide and the ethanol have significantly different pH values. The ethanol, or some substituted liquid, sometimes has to be pH adjusted in order to obtain the proper relationship to the particles. This pH imbalance creates a slight electric repulsion between individual particles. The particles, which on their own tend to agglomerate, are placed, in high concentration, into ethanol and the mixture is sonicated. The ultrasonic waves break apart the agglomerated particles creating the suspension. The concentrated suspension may then be diluted down to the desired level by adding more ethanol. When done properly, this suspension is stable almost indefinitely. In the experiments conducted for this paper, suspensions were sometimes left to sit for months and were still usable.

A 38.1 cm (15") duct is placed upstream of the jet exit to generate a co-flow. The co-flow is generated by channeling part of the entrained air into the jet through the duct without using any fans or blowers. The co-flow is seeded by a fogger to avoid spurious velocity vectors in the entrained air region. The average droplet size is about 0.25 and $0.7\ \mu\text{m}$ for the jet flow and co-flow, respectively. The turbulence statistics were converged using 600 to 650 image pairs [Kim et al. 2009a&b]. Thus, about 700 image pairs are used for all the statistics reported in this paper. The uncertainty in the PIV measurements is related to many parameters such as the particle size and density, and turbulence scales of interest. Within 5% deviation from the actual turbulence intensity, the seeded particles trace the flow up to 20 and 70 kHz of turbulence fluctuations frequency for 0.7 and $0.25\ \mu\text{m}$ particles respectively [Melling 1997]. Based on this calculation, the uncertainty of turbulence intensity is about 5% up to a Strouhal number of

1.33. However, the uncertainty level for the mean and turbulence statistics was within $\pm 3\%$ and $\pm 15\%$, respectively, based on the repeatability measurements for the baseline jet. In the shock-containing imperfectly expanded jets, the particles lag behind the actual flow speed in regions near the shocks. Melling [1997] showed that a $0.25\text{ }\mu\text{m}$ particle passing through an oblique shock wave (upstream and downstream Mach numbers are 1.5 and 1.15, respectively) needed about 0.5 mm before it was within 5% of the downstream velocity. In the present research, the shock is not quite as strong as Melling's example so an estimated distance required for the particle to reach the downstream velocity is about 0.2 mm. Thus, the uncertainty of the present PIV measurements is not affected by particle lag for most of the flow field measured.

3. RESULTS

The three major control parameters are duty cycle, forcing frequency (or Strouhal number), and azimuthal mode. The effects of these parameters will be investigated in cold $M_J = 0.9, 1.2, 1.3$, and 1.4 jets. The Mach 0.9 jet was used to further develop both control and measurements tools before moving on to supersonic jets. The measures for the jet spreading used in the research are centerline Mach number and the jet width at half maximum (the jet width based on the half velocity of the local centerline velocity). Large-scale structures generated by forcing are visualized and their role in jet mixing enhancement are also discussed. Four main results to be discussed are:

- a) $M_J = 0.9$ unheated subsonic jet (extensive forcing frequencies and azimuthal modes, Sec. 3.1)
- b) $M_J = 1.2, 1.3$, and 1.4 unheated supersonic jet (limited azimuthal modes, Sec. 3.2)
- c) $M_J = 0.9$ heated subsonic jet (limited azimuthal modes at single forcing frequency, Sec. 3.3)
- d) $M_J = 1.65$ unheated subsonic jet (only for one mode and several forcing frequency, Sec. 3.4)

As discussed in Sec. 1.3, each section has unique objectives as follows:

- 3.1) To clarify the effects of duty cycle, forcing frequency, and azimuthal modes in $M_J = 0.9$ unheated jets and to find the optimum duty cycle for each forcing frequency.
- 3.2) To determine the control authority of plasma actuators in unheated supersonic jets of $M_J = 1.2, 1.3$, and 1.4 for limited azimuthal modes based the results in the $M_J 0.9$ jet.
- 3.3) To find the effects of the stagnation temperature on the effectiveness of plasma actuators in $M_J = 0.9$ heated jets for very limited azimuthal mode and fixed forcing Strouhal number of 0.3.
- 3.4) To determine the control authority in a high Mach number jet of $M_J = 1.65$ perfectly-expanded unheated jet only for $m = \pm 1$ and several St_{DF} 's.

The extensive results in $M_J = 0.9$ and 1.3 jets serve as a reference for generating a test matrix for other experiments.

3.1 Mach 0.9 Cold Subsonic Jet

Detailed two-component particle image velocimetry measurements on a streamwise plane passing through the jet centerline are used to explore the effects of forcing Strouhal number and azimuthal mode on the Mach 0.9 jet. The overall performance of the plasma actuators at each Strouhal number and mode are discussed by using the average velocity images and turbulence statistics. Then, conditionally-averaged velocity components superimposed on conditionally-averaged streamlines are be used to investigate the dynamics of vortices or large-scale structures and their roles in the jet development.

3.1.1 Effects of Duty Cycle of Input Signal

The effect of duty cycle, percentage of arc duration to pulsation period, was investigated at various St_{DF} 's for $m = \pm 1$. However, only results for $St_{DF} = 0.32$, near the jet column instability, are shown in Fig. 3.1.1. The figure shows the Mach number decay along the jet centerline up to $x/D = 11$ at duty cycles ranging from 3% to 50%. The centerline Mach number is an indirect indicator of jet spreading and the decay of Mach number is faster for increased jet spreading in general. As the duty cycle decreases,

the centerline Mach number decays faster, implying faster jet spreading. When the duty cycle is further decreased, there is occasional misfire in plasma actuators. Thus, the optimal duty cycle at a forcing frequency is determined at smallest duty cycle which does not cause misfire in actuators. The following equation shows the relation between duty cycle (τ is not in percentage but in fraction, so $\tau = 0 - 1$) and forcing frequency (f_F),

$$\tau = \begin{cases} [0.6(f_F / 1000) + 2] / 100 & \text{for } f_F < 30 \text{ kHz} \\ [0.26(f_F / 1000) + 11.42] / 100 & \text{for } f_F \geq 30 \text{ kHz} \end{cases} \quad (1)$$

In all following experiments, the duty cycle is determined by Eq. 1. Then the pulse train $g(t)$ for each actuator is given as:

$$g(t) = \begin{cases} 0 & \text{if } 0 < t < \frac{m\phi_a}{2\pi f_F} \\ 1 & \text{if } \frac{m\phi_a}{2\pi f_F} < t < \frac{m\phi_a}{2\pi f_F} + \frac{\tau}{f_F} \\ 0 & \text{if } \frac{m\phi_a}{2\pi f_F} + \frac{\tau}{f_F} < t < 1 \end{cases} \quad (2)$$

where $\phi_a = \pi(i-1)/4$ is the channel phase corresponding to the azimuthal location of the actuator in the nozzle extension (see Fig. 2.1 or 2.3), $i=1, 2, \dots, N$ is the channel number, N is the number of channels ($N=8$ in the present work), and m is the phase shift parameter (azimuthal mode number). For $m=0$, all plasma actuators operate in phase, producing axisymmetric forcing mode; $m=1$ produces sequential operation in the first helical mode; and $m=\pm 1$ generates two counter-rotating helical modes, superposition of which produces a “flapping” mode. A more detailed description of the input pulse train is given in Samimy et al. [2007a] and Kim et al. [2009a].

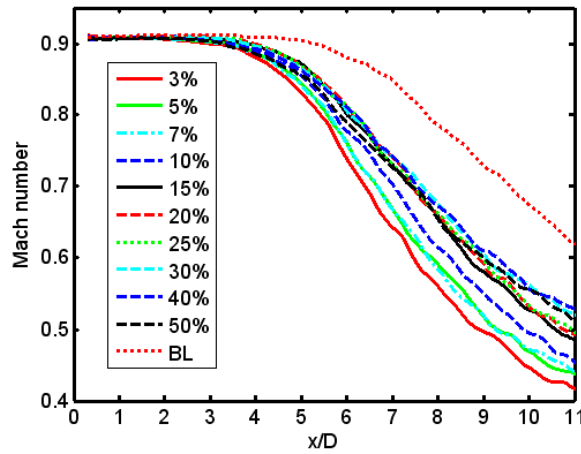


Fig. 3.1.1 Centerline Mach number at $St_{DF} = 0.32$ (3.5 kHz) and at $m = \pm 1$.

3.1.2 Effects of Forcing Strouhal Number on Overall Jet Spreading

The jet was forced at forcing Strouhal numbers (St_{DF}) ranging from 0.09 to 3.08 for all available azimuthal modes. However, only results for $m = 0, 1, 3$ and ± 1 are shown in this section. The centerline velocity decay has been widely used as a measure of the jet spreading or mixing with the ambient air, as often it is the only available results. The centerline velocity decay increases as the jet spread increases in most cases. In the present research, growth of the full width at half maximum (FWHM) of the jet centerline velocity is also used as a measure for the jet spreading or mixing.

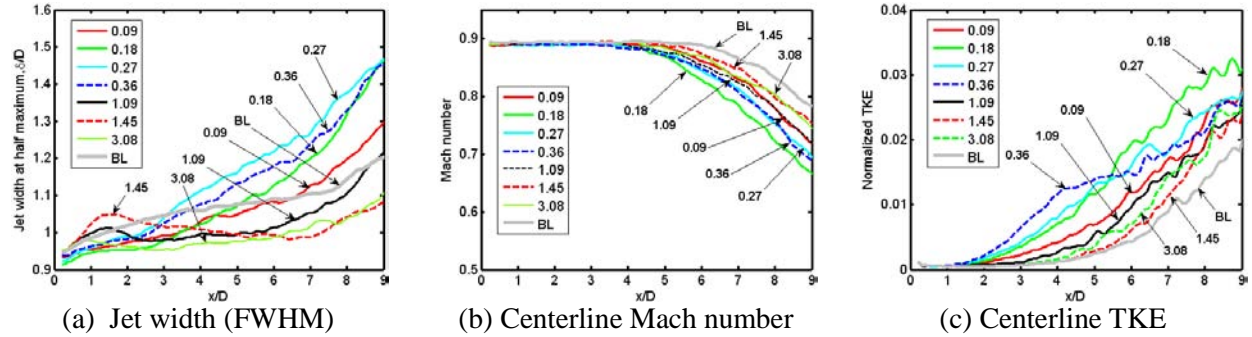


Fig. 3.1.2 Jet width development with downstream locations (a), centerline Mach number decay (b), and centerline TKE (c) at $m = 0$.

For $m = 0$ mode, the jet width (calculated by using FWHM and referred as the jet width henceforth), is shown in Fig. 3.1.2 along with the jet centerline Mach number and the measured 2-component turbulence kinetic energy (from here on TKE) profiles. The trend of jet width with the St_{DF} does not match the centerline Mach number decay trend at this mode. However, the trend of the centerline Mach number decay is quite similar to that of the centerline TKE development. As will be shown later, the mismatch of these trends is observed only at the axisymmetric mode ($m = 0$). At this point, it is not clear why they are so different at this mode.

The jet width shows the effects of forcing on the jet spreading for the entire streamwise measurement extent, whereas the centerline Mach number decay provides the overall mixing/spreading effect only beyond the potential core. When the jet is forced at a Strouhal number near or below 0.36, the jet width grows almost linearly in downstream direction for the entire measured x/D . The best spreading/mixing is observed at $St_{DF} = 0.27$, where the jet width is increased by about 20% at $x/D = 9$. The jet width grew faster and saturated closer to the nozzle exit when the jet was forced at higher Strouhal numbers resulting in significant mixing reduction by $x/D = 9$.

As the forcing Strouhal number is increased, the saturation occurred earlier since the generated structures are smaller and thus their life span is shorter. At a St_{DF} equal or greater than 1.0, the jet width is reduced upstream of $x/D = 2$ and remained unchanged up to $x/D = 6$ (which is approximately the end of the potential core). The jet spreading is reduced by forcing at a higher St_D most likely by suppressing the formation and/or development of large-scale structures, which play an important role in entrainment and jet spreading/mixing.

Figure 3.1.3 shows the development of jet width and the centerline Mach number at $m = 1$ mode. For this mode, unlike for the $m = 0$ mode, the trend of the centerline Mach number is similar to that of the jet width development downstream of x/D of about 5. Although not shown, the trend of the centerline

TKE matches with these two trends as well. As mentioned earlier, the three trends are very similar for all the azimuthal modes tested except for $m = 0$.

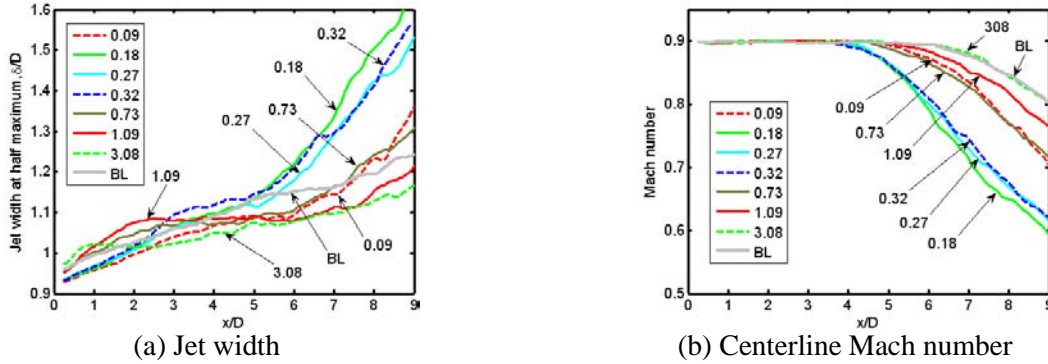


Fig. 3.1.3 Growth of the jet width with downstream locations (a) and centerline Mach number decay (b) at $m = 1$.

For $m=1$, the growth of the jet width is maximum when forcing at $St_{DF} = 0.18$, and only a slightly lower growth is observed at $St_{DF} = 0.27$ and 0.32 . For these three forcing cases, as well as others with relatively strong jet spreading, the initial linear growth of the jet width stops near the end of potential core before starting another linear growth region, but with much larger slope. At a St_{DF} of 0.36 (not shown here) and higher, there was a region of almost zero growth rate as clearly observed at a St_{DF} of 1.09 . The significantly reduced growth near the end of the jet potential core is due to the cross-centerline interaction of large scale structures in this region. This will be further discussed later.

At St_{DF} 's greater than 1.0 , the initial growth rate of the jet width is increased over that of the baseline (Fig. 3.1.3a), but decreased for St_{DF} 's less than 0.7 . The saturation in the jet width growth occurs earlier and the saturated jet width also decreases as the St_{DF} increases, which is similar to what was found at $m = 0$ mode. In the near field, the growth and saturation of the jet width with the St_{DF} is consistent with the pressure perturbation level measurements along the nozzle lip line using a single actuator [Samimy et al. 2007]. The jet width remains about the same after it saturated, and the jet growth is suppressed at high St_{DF} 's as was true for the $m = 0$ mode. As will be discussed in a later section, the quick jet width saturation with increasing St_{DF} is due to the smaller structures and their shorter life span when forcing the jet at higher frequencies.

For the first combined mode ($m = \pm 1$), often referred to as the flapping mode, the jet width growth on the flapping plane is shown in Fig. 3.1.4a. The trend of the jet width growth is consistent with the centerline Mach number decay as shown in Fig. 3.1.4b. Note that the ordinate scale in Fig. 3.1.4a is over twice that for the other modes presented earlier. In the upstream region, the trend of the jet width growth with St_{DF} is similar to that for the $m = 1$ mode. Similar to the results for the other modes presented, the growth in jet width is suppressed when the jet is forced at higher St_{DF} 's, as can be seen at 3.08 . The jet width is increased significantly near $St_{DF} = 0.3$, and the maximum growth is at $St_{DF} = 0.27$, *approximately 3 times that of the baseline at $x/D = 9$* . At low St_{DF} 's, the jet width grows monotonically up to $x/D = 4$, which is near the end of the potential core. When St_{DF} is increased or decreased from 0.27 , the jet spreading is decreased very rapidly. At St_{DF} of 0.09 and 0.73 , the jet width increases monotonically (almost linearly) with downstream location. The growth in jet width near $St_{DF} = 0.3$ starts to increase exponentially at $x/D = 4$, where the potential core ends as seen in Fig. 3.1.4b. As with the other azimuthal

modes, the enhanced growth resulted in a reduction in the jet potential core. The potential core length was reduced to $x/D = 4$ for the best mixing case from $x/D = 6$ for the baseline case (Fig. 3.1.4b).

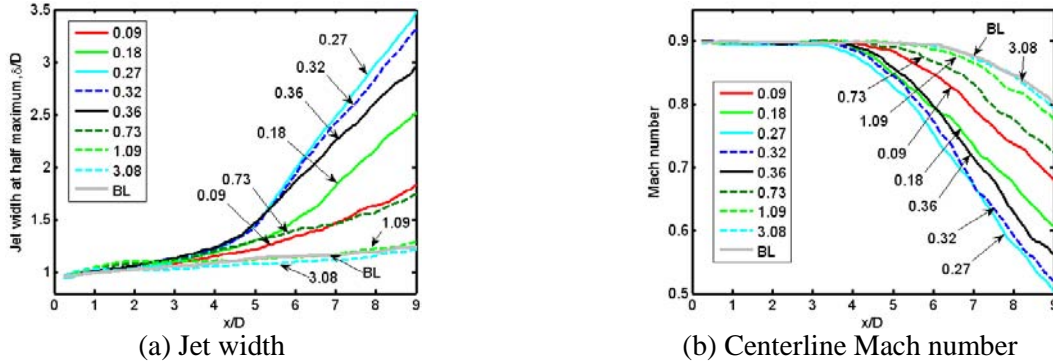


Fig. 3.1.4 Development of jet width and centerline Mach number for $m = \pm 1$ mode on the flapping plane. Note that the ordinate scale in (a) is over twice the others in Figs. 3.1.2 & 3.1.3.

As was presented and will be further discussed below, the most effective forcing was at $m = \pm 1$ mode as far as the jet spreading is concerned. For this mode, the average streamwise velocity contours, on the flapping plane of the jet, are shown in Fig. 3.1.5 at $St_{DF} = 0.18, 0.27, 0.72, 1.08$, and 3.08 . The jet exit velocity is about 280 m/s and varies slightly depending on the jet stagnation temperature. In the figure, the low-speed background is for the co-flow where the velocity is less than 3 m/s (about 1% of the jet exit velocity) and is not expected to affect the jet development significantly.

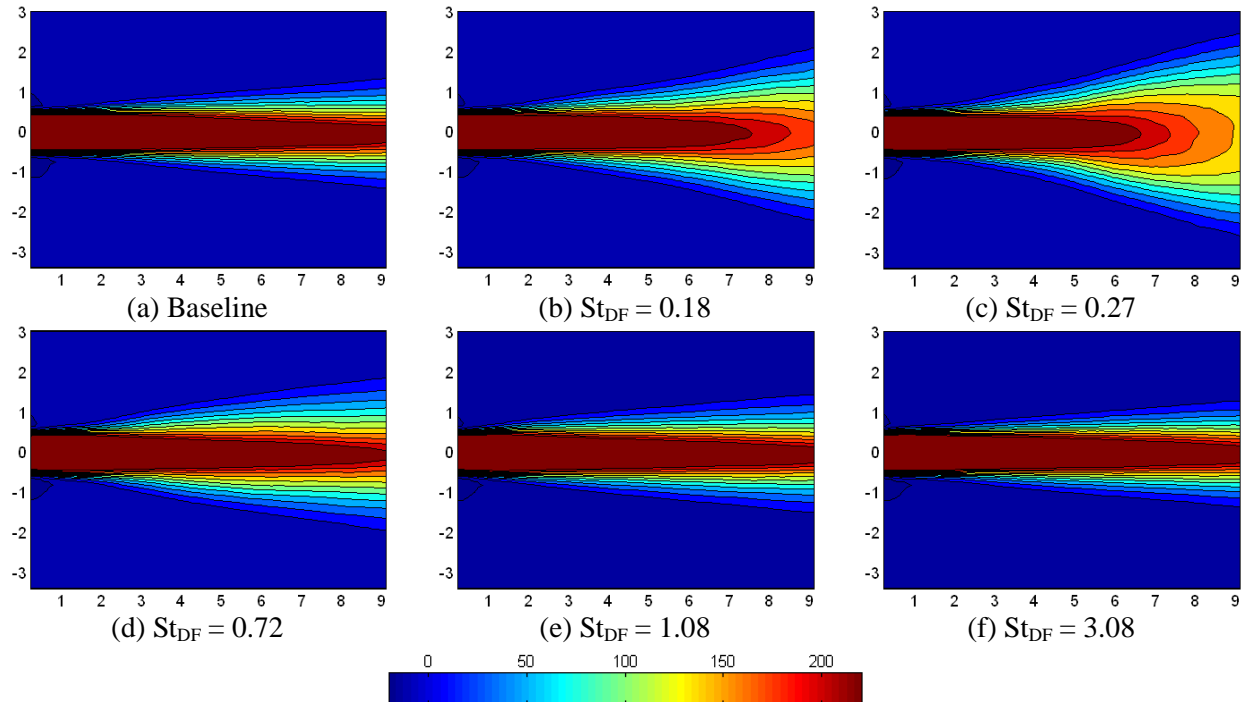


Fig. 3.1.5 Average streamwise velocity field for various forcing Strouhal numbers at $m = \pm 1$. The velocity scale is in m/s and the exit jet velocity is about 280 m/s.

As St_{DF} increases, the jet spreading angle increases until it reaches a maximum around $St_{DF} = 0.3$, beyond which it decreases slowly. The jet spreading is almost the same as that of the baseline jet when forcing at St_{DF} 's greater than about 1.0. The results suggest that forcing around a St_D of 0.3 is the most effective in spreading the jet, which is the jet preferred St_D at this mode. At this St_{DF} (0.3), the jet potential core length is significantly shortened as shown in Fig. 3.1.5(c). This can be more readily seen in Fig. 3.1.4b, which shows the centerline Mach number distributions with various forcing Strouhal numbers. The centerline Mach number decays the fastest at $St_{DF} = 0.27$. This is consistent with the highest jet spreading, shown in Fig. 3.1.5(c). As the St_{DF} increases beyond about 0.3, the potential core increases, and becomes almost the same as that of the baseline jet for St_{DF} 's greater than about 1.0.

The jet response to the forcing with plasma actuators is dependent on the forcing frequency, duty cycle, and azimuthal mode. The effects of duty cycle were shown in Sec. 3.1.1, and the duty cycle was predetermined by Eq. 1 for each forcing frequency. The optimum forcing Strouhal number, where the jet spreading is maximum, depends on the forcing azimuthal mode as can be inferred from the results presented so far. Table 2 shows the optimal forcing Strouhal number for each mode based on the jet width downstream of the jet potential core. The optimum St_{DF} is about 0.3 except for azimuthal modes 1 and 3. However, the Strouhal number for the second best is 0.27 for $m = 1$ mode and the jet width growth at this value is very close to the optimum value. The only exception is $m = 3$ mode, which has a maximum jet width growth at $St_{DF} = 0.09$ (1/3 of other cases). The jet preferred Strouhal number, reported in the literature for the past 10-20 years varies from 0.2 to 0.6. Thus, the optimum St_{DF} for each mode is within the range in the literature except for $m = 3$.

Table 2 Optimum forcing Strouhal number for each mode based on the jet width downstream of jet potential core region.

Mode	0	1	2	3	± 1	± 2	± 4
St_{DF}	0.27	0.18	0.36	0.09	0.27	0.32	0.32

3.1.3 Effects of Azimuthal Mode

As was presented earlier, the jet preferred Strouhal number, where the jet spreading/mixing is maximized, varied for different azimuthal modes, but remained close to 0.3 for most modes except for $m = 3$, which was 0.09. The average streamwise velocity contours are shown in Fig. 3.1.6 for $m = 0-3, \pm 1, \pm 2$, and ± 4 modes at St_{DF} corresponding to those in Table 2. For all modes, the jet spreading is significantly enhanced compared to that of the baseline jet (Fig. 3.1.6e), with the largest enhancement at $m = \pm 1$ mode (Fig. 3.1.6f). A shorter visual potential core length is observed for greater jet spreading. This is more readily observed in the centerline Mach number profiles shown in Fig. 3.1.7a. The length of the potential core for $m = 1$ and ± 2 modes is reduced by a similar amount. The least spreading is observed when exciting $m = \pm 4$. As was discussed earlier, the mean velocity contours and the centerline Mach number only show the effects of forcing on the potential core length and the overall spreading downstream of the potential core.

The jet width and equivalent width development are shown in Figs. 3.1.7b and 3.1.7, which show the effects of forcing over the entire region of the jet flow from the nozzle exit to $x/D = 9$. Figure 3.1.7b shows the jet width calculated from Fig. 3.1.6, and thus only shows the jet width on the PIV plane in this figure. Since the jet cross-section at a far downstream location is nearly axisymmetric, Fig. 3.1.7b is

appropriate for evaluating the overall spreading except for $m = \pm 1$ mode. For $m = \pm 1$ mode, the jet spreads significantly more in the flapping plane compared to the non-flapping plane. The cross-section is assumed to be approximately elliptic and thus the equivalent jet width for $m = \pm 1$ is calculated from the square root of the multiplication of jet widths on the flapping and non-flapping planes, to take into account the highly non-axisymmetric spreading. The results for all the modes are shown in Fig. 3.1.7c. The trend of equivalent jet width is consistent with centerline Mach number except for $m = 0$ mode. This is due to the relatively slow decay of the centerline Mach number for $m = 0$ mode as will be discussed later.

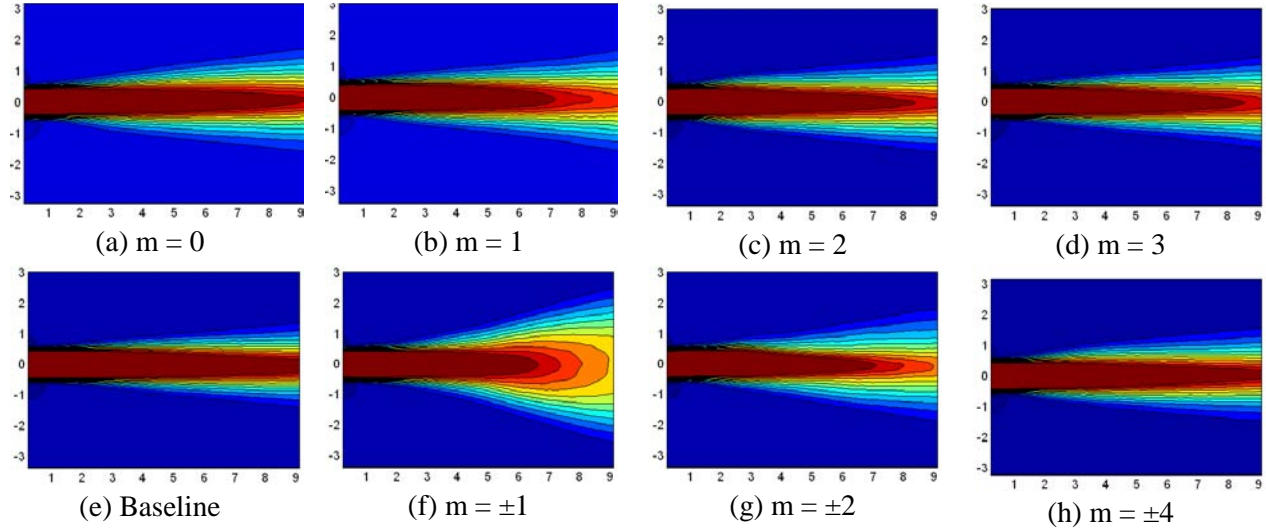


Fig. 3.1.6 Average streamwise velocity contours for various azimuthal modes at the St_{DF} 's shown in Table 2.

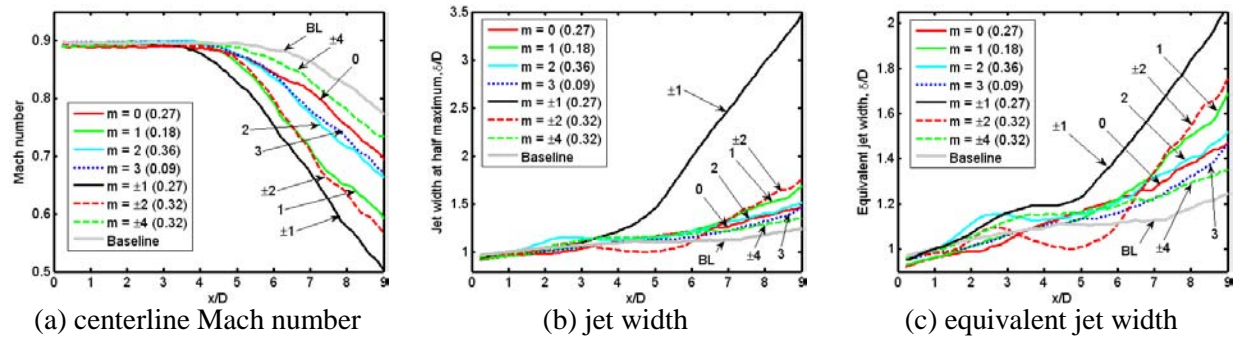


Fig. 3.1.7 Development of centerline Mach number and jet width and equivalent width at various azimuthal modes at St_{DF} 's shown in Table 2.

The equivalent jet width also shows that the maximum and minimum jet spreading occurs at $m = \pm 1$ and $m = \pm 4$ modes, respectively. For $m = 2$, ± 1 , and ± 4 modes, the jet width grows significantly over the other modes in the initial region or near field. However, the growth rate of the jet width for $m = 2$ and ± 4 decreases near the end of the potential core and thus this lead to a limited increase in jet widths by $x/D = 9$ (Fig. 3.1.7c). For $m = \pm 2$ mode, the jet width remains saturated from $x/D = 2.5$ until $x/D = 5$

(approximate end of the potential core), and then experiences rapid growth further downstream. At higher azimuthal modes of $m = 3$ and ± 4 , the jet centerline Mach number decay is slower and the increase in the jet width at a far downstream location is less than those of other modes. For $m = \pm 2$, the centerline Mach number decay is comparable to that of $m = \pm 1$ although the streamwise velocity contour is not comparable. In addition to the jet spreading, it seems that the vortex-vortex interaction across the jet column is another factor related to the centerline Mach number decay. This will be further discussed later by using large-scale structures and their dynamic interaction.

3.1.4 Effects Forcing on Turbulence Statistics

As presented in the previous section, changes in the mean flow characteristics depend significantly on the St_{DF} and forcing azimuthal mode. In this section, the effects of forcing on the turbulence statistics are explored along the jet centerline. The normalized two-dimensional turbulent kinetic energy and anisotropy ratio (σ_v/σ_u , σ_u and σ_v are RMS of x- and y-component velocity fluctuations, respectively) along the jet centerline are shown in Fig. 3.1.8 for $m = 0, 1$, and 3 modes.

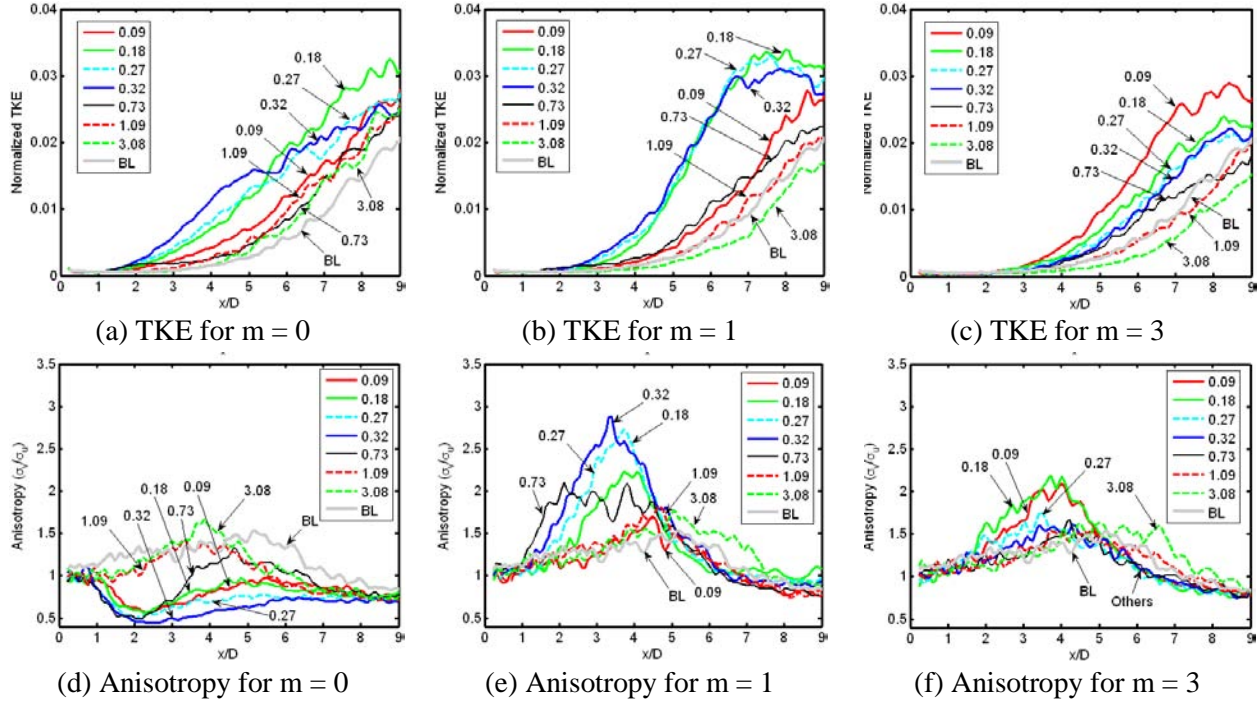


Fig. 3.1.8 Normalized TKE and anisotropy for $m = 0, 1$, and 3 modes along the jet centerline.

For $m = 0$ mode, the TKE is increased for all St_{DF} 's with the maximum amplification occurring at $St_{DF} = 0.18$, which corresponds to the case where the centerline Mach number decayed the fastest (Fig. 3.1.2b). The TKE is more amplified at $St_{DF} = 0.32$ and 0.36 (not shown here) up to around the end of the potential core ($x/D \approx 5$). Up to $x/D = 1$ to 1.5 , the anisotropic ratio is 1, as expected, as the fluctuations are due to random noise and measurement errors. However, further downstream, the ratio is substantially less than one at $St_{DF} \leq 0.73$, and substantially larger than one for the baseline jet and at $St_{DF} \geq 1.09$ for $m=0$ case (Fig. 3.1.8d). At lower St_{DF} 's, the streamwise (or x-component) turbulence intensity was amplified

more than the cross-stream (y-component) turbulence intensity. At higher St_{DF} 's, the scales of the generated structures are so small that their influence on the centerline is expected to be very limited, and thus the forcing effects are expected to be negligible. On the other hand, the scales of the induced structures are much larger at lower St_{DF} 's, increasing interactions across the jet centerline and thus significantly altering the anisotropy ratio. The anisotropy ratio was reduced for all cases downstream of the potential core.

For $m = 1$, a significant amplification in TKE was observed over a wide range of St_{DF} 's from 0.18 to 0.36 (not shown here). The TKE is saturated around $x/D = 7$ for these forcing Strouhal numbers. Contrary to the $m = 0$ case, the anisotropy in Fig. 3.1.8e implies that the cross-stream velocity fluctuations are dominant over the streamwise velocity fluctuations for St_{DF} 's = 0.18-0.36 (0.36 case is not shown) in the potential core region. As will be discussed later, the difference is associated with the symmetric or asymmetric nature of the large-scale structures across the jet diameter. The turbulence field becomes more isotropic downstream of the potential core. Figure 3.1.8e shows that the anisotropy is saturated near the end of potential core. As the St_{DF} is increased, the amplification level decreases and the anisotropy is about the same level as the baseline jet case for St_{DF} 's equal or greater than 1.8 (not shown here).

For $m = 3$, the amplification in TKE is moderate except for $St_{DF} = 0.09$ and 0.18, where the jet spreading was maximum. At a low St_{DF} , the anisotropy increased near the end of the potential core similar to that for $m = 1$, but the increase is moderate. Interestingly, the TKE level was reduced when the jet was forced at a St_{DF} greater than 1.0. The reduction in TKE at high St_{DF} 's is related to the broadband noise suppression seen for this mode [Samimy et al. 2007a, Bridges and Wernet 2002].

The development of TKE and anisotropy along the jet centerline for $m = \pm 1$ are shown in Fig. 3.1.9. A dramatic increase in TKE was observed at low St_{DF} 's. The anisotropy also increased significantly at low St_{DF} 's, but the trend showed some disparity from that of TKE. The increase in anisotropy means that the velocity fluctuations in the cross-stream direction are dominant over those in the streamwise direction, as was also seen for $m = 1$. Since the flapping plane is in the y-direction, the domination of the cross-stream velocity fluctuations is expected. As the St_{DF} is increased, the development of TKE and isotropy approach the levels of the baseline jet.

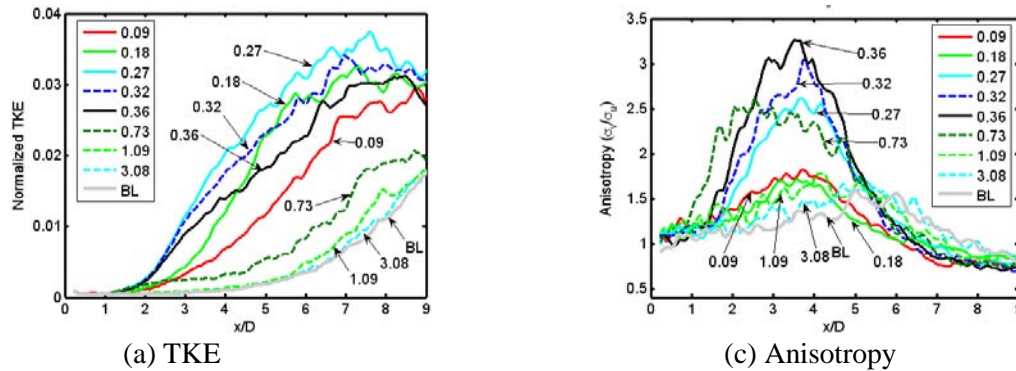


Fig. 3.1.9 Normalized TKE and anisotropy for $m = \pm 1$ mode along the jet centerline.

Figure 3.1.10 shows the development of TKE and anisotropy at the modes and St_{DF} 's, where the jet width was maximized as shown in Table 2. The interaction between the generated structures across the jet centerline is expected to be noticeable when the scale of structures is large and comparable to the jet

diameter. The onset of where the TKE starts to increase over the background level appears to be approximately the same for all azimuthal modes, but the amplification rates are significantly different for each mode. For $m = 0$, the TKE developed monotonically with downstream location, and did not show any saturation in the measured range. Vortex rings were generated by the plasma actuators as will be shown later, and the scale/size of the rings grew monotonically with downstream location, and thus the TKE was also expected to grow in such a fashion. For $m = \pm 1$, the TKE started to grow significantly as early as $x/D = 2$ and saturated around $x/D = 7$. The least amplification in TKE is observed for $m = \pm 4$ mode, where its growth rate is about the same as the baseline jet. For most cases, the growth in TKE is saturated around $x/D = 7-8$.

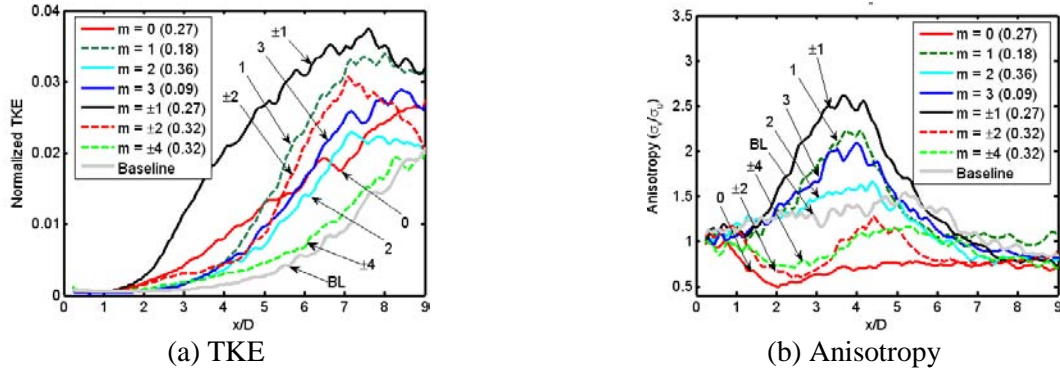


Fig. 3.1.10 Development of TKE and anisotropy at the St_{DF} 's in Table 2.

The development of anisotropy in Fig. 3.1.10b is very interesting. For even numbered modes, anisotropy is decreased, implying the streamwise velocity fluctuations are dominant in TKE. The case for $m = 2$ seemed different, but the development at a lower St_{DF} is similar to other even numbered modes. When the jet was forced at odd numbered modes, the anisotropy is increased and saturated around $x/D = 3.5$. The anisotropy reached a minimum for the even numbered modes around x/D of 2-2.5. These differences can be explained through vortex dynamics of the generated structures, as will be presented and discussed in the following section.

3.1.5 Vortex Dynamics and Its Role in the Jet Development

The overall effects of St_{DF} and forcing azimuthal mode were investigated and discussed in the earlier sections by using the average velocity contours, the jet width, TKE, and anisotropy. The average velocity and turbulence statistics are useful in evaluating the overall effects of St_{DF} and forcing azimuthal mode. However, they do not reveal details of flow structures and their role in the jet development. Thus, large-scale structures are extracted from PIV data and their dynamics are discussed in this section.

The Galilean decomposition is applied to the measured velocity fields to extract large-scale structures. The convection velocity of large-scale structures must be known to obtain the Galilean-decomposed velocity field. Once the convection velocity of large-scale structures is known, the Galilean-decomposed velocity field is obtained by subtracting the convection velocity from the measured velocity field [Konstantinidis et al. 2005]. Thus in the Galilean decomposition, the reference frame moves at the convection velocity. A large-scale structure does exist and is visualized in the Galilean-decomposed

velocity field if the streamlines make a closed loop or have a spiral pattern [Kline and Robinson 1990, Robinson et al. 1989].

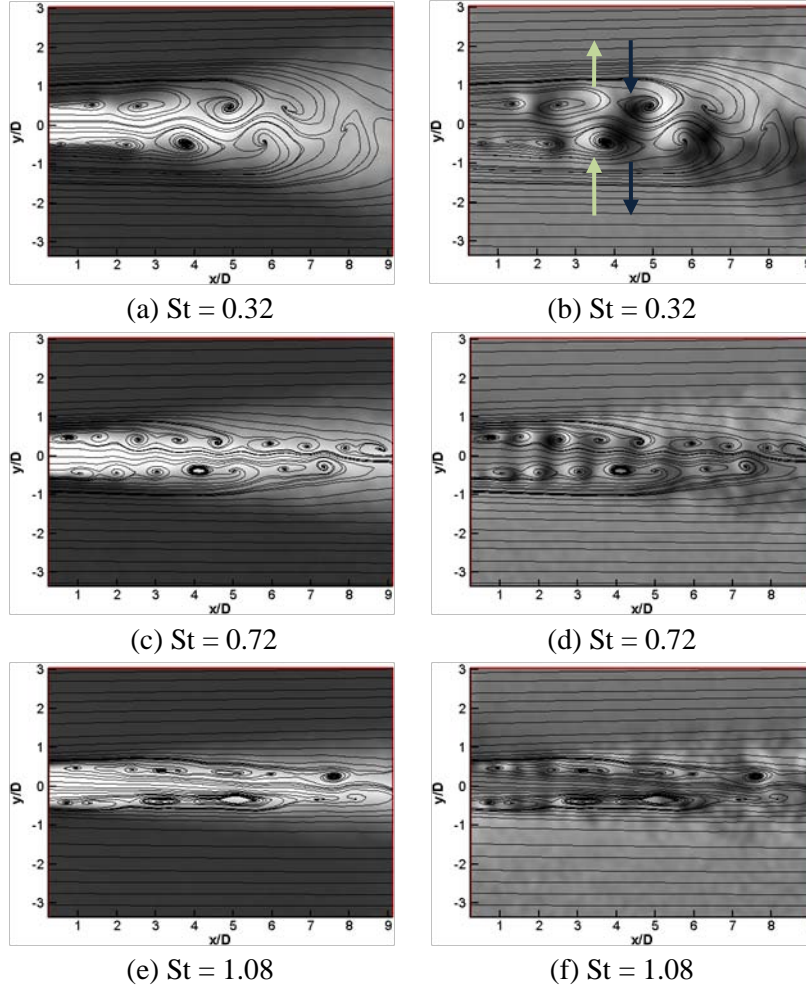


Fig. 3.1.11 Conditionally-averaged Galilean decomposed velocity fields and streamlines of streamwise (left column) and cross-streamwise (right column) velocities at $m = \pm 1$.

In the present research, a conditionally-averaged velocity field was obtained and used for large-scale structures visualization. To get a conditionally-averaged field from 700 instantaneous velocity fields, two-dimensional cross-correlation was used to extract large-scale structures. A correlation window was taken in a given instantaneous velocity field. The velocity pattern within the window was correlated to the available 700 instantaneous velocity fields. All instantaneous images with a correlation level greater than a threshold value were ensemble averaged to form a conditionally-averaged image of the 2-D velocity field. One could also use proper orthogonal decomposition for this purpose as in Kastner et al. [2008]. The next step is to calculate convection velocity of large-scale structures. Two-dimensional spatial-correlations were used to calculate the spacing or wavelength of large-scale structures for the forced cases. The convection velocity is obtained by multiplying the large-scale structure spacing by the forcing frequency as was done by Troutt and McLaughlin [1982]. The last step to obtain a conditionally-averaged Galilean-decomposed velocity field is to subtract the convection velocity from the conditionally-averaged

velocity field. Then, the large-scale structures are visualized when the Galilean streamlines are added, as was detailed in Kline and Robinson [1990] and in Robinson et al. [1989], and is shown in Fig. 3.1.11 for $m=\pm 1$ at St_{DF} 's of 0.32, 0.72, and 1.08.

In the figure, the conditionally-averaged Galilean streamlines and streamwise velocity magnitude (Fig. 3.1.11a) and cross-stream velocity magnitude (Fig. 3.1.11b) are superimposed. For the streamwise velocity, the dark and bright regions represent the slower and faster velocities, respectively. The maximum and minimum velocities are about 280 (in the potential core) and 3 m/s (in the ambient region). For the cross-stream velocity, the medium tone background represents near zero velocity, and the brighter and darker tones indicate positive and negative velocities, respectively. In Figs. 3.1.11-13, the background velocity contours are added for the ease of visualization. The figure shows the size and spacing of vortices, and the interaction between not only the vortices but also the vortices and the jet column. The large-scale structures generated by the forcing are robust and seem to be two-dimensional on the visualization plane, rotating either clockwise or counter-clockwise, for those in the bottom shear layer and top shear layer, respectively.

At lower St_{DF} 's, the generated large-scale structures are very well organized and their scale by the end of the potential core is comparable to the nozzle exit diameter. The vortices in the top and bottom shear layer are out of phase since the jet was forced with the 1st flapping mode ($m = \pm 1$). Downward velocity is induced in the downstream side of a vortex in the bottom shear layer and the upstream side of a vortex in the top shear layer, while upward velocity is induced in the upstream side of a vortex in the bottom shear layer and the downstream side of a vortex in the top shear layer, as indicated by arrows in Fig. 3.1.11b. The cross-stream velocity, induced by the vortices, appears strong enough to cause undulations in the jet column, which can be inferred from wavy streamlines along the jet centerline. When the vortices in the top and bottom shear layers are out-of-phase, as expected for $m=\pm 1$ case, the upward and downward induced velocities are in the same cross-stream direction at the same streamwise location, as shown in Fig. 3.1.11b. As a result, the jet appears to be flapping by the induced velocity. In addition to the undulating motion of the jet column, the entrainment of the ambient air and the ejection of jet fluid into the ambient by the induced cross-stream velocity increase the lateral spread of the jet.

When the St_{DF} is increased to 0.72, the spacing of the adjacent vortices and the scale of the generated structures are significantly reduced (about halved) as shown in Fig. 3.1.11c. At this Strouhal number, the interaction between the vortices in the top and bottom shear layers is weaker due to reduced scale of the generated vortices. The jet column did not significantly undulate because of the smaller vortices and weaker interactions between the vortices and the jet column at this Strouhal number. As shown in Figs. 3.1.4 and 3.1.5, the jet potential core was not significantly changed by the generated structures due to the limited interaction between top and bottom shear layers. As shown in Fig. 3.1.11d, the induced cross-stream velocity is confined to the thin top and bottom shear layers. Since the induced cross-stream velocity is reduced, it is expected that the entrainment and ejection of fluid would also be limited at this Strouhal number. As a result, the jet spreading was less enhanced than at $St_{DF} = 0.32$.

At higher St_{DF} of 1.08, the generated vortices are barely identifiable and are not organized, resembling those in the unforced jet. This is the reason for the mean flow (Figs. 3.1.4 and 3.1.5) and turbulence statistics (Fig. 3.1.9) for this forced case to be similar to those for the baseline jet. For all other

modes, the effects of St_{DF} on the spacing and size of the generated structures are very similar, and therefore, the results are not presented here.

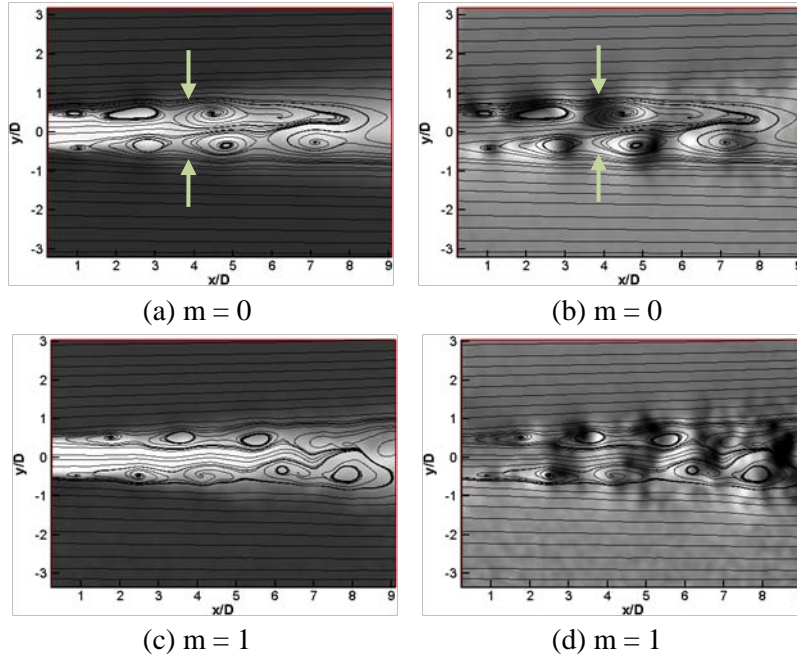


Fig. 3.1.12 Conditionally-averaged Galilean streamlines and velocity magnitude contours for streamwise (left column) and cross-streamwise (right column) velocities for $m = 0$ and 1 modes at $St_{DF} = 0.32$.

Figure 3.1.12 shows conditionally-averaged streamwise and cross-stream velocity contours with superimposed Galilean streamlines for two additional modes $m = 0$ and 1 at a St_{DF} of 0.32. As discussed earlier, the forcing at even- and odd-numbered azimuthal modes showed distinctly different turbulence characteristics as shown in Fig. 3.1.10b – hence the selection of these two representative modes. For the axisymmetric mode ($m = 0$), the streamwise dimensions of the generated vortices are approximately the same as those for the flapping mode ($m = \pm 1$), but the cross-stream scales are smaller. Although the vortices at this mode appear to be as strong as those in the $m = \pm 1$ mode, the jet spreading is not as significant as seen in the $m = \pm 1$ case. The symmetry of the vortices seems to be responsible for the slower jet spreading. Since the generated structures for $m = 0$ are donut-shaped vortex rings, their development in the cross-stream direction is limited by this symmetry. When one part of the vortex ring attempts to grow toward the jet centerline, the opposite part also takes the same action, and thus the growth of the ring toward the jet centerline is limited due to the axisymmetric nature of the ring vortex. For the flapping mode ($m = \pm 1$), the vortex could grow toward the jet centerline easily by pushing the jet column to the other side as shown in Fig. 3.1.11a. This limited growth of the vortex is partially responsible for the slower jet spreading as seen in Figs. 3.1.6 and 3.1.7.

In addition to the slower spreading for the $m=0$ case, the jet centerline Mach number also decays relatively slowly as seen in Fig. 3.1.7. It is conjectured that the jet centerline Mach number decay is closely related to the interaction between vortices and the jet column, which affects the entrainment of slow-moving fluid into the jet plume. The vortices at this mode do not cross the jet centerline because of

their symmetry as discussed earlier. As a result, the interaction is not as destructive as in the asymmetric cases (odd numbered modes). The entrained fluid, from the much slower moving surrounding air near the trailing region of a ring as indicated by arrows in Fig. 3.1.12, goes through acceleration at the center of the ring due to self-induction. The self induction seems to make the flow near the centerline accelerated, which counters the slowing action of the entrained fluid. Thus, the acceleration due to self-induction at the jet centerline and the symmetry of the vortex ring may be partially responsible for the slower centerline decay when compared to the other modes, as shown in Fig. 3.1.7.

Another interesting finding at $m = 0$ is that the jet centerline velocity seems to undulate periodically with the downstream location. The jet fluid at the center of a vortex ring is accelerated by self-induction of the vortex ring. In the trailing region of a vortex ring, the velocity is expected to decrease due to the entrainment of the slower moving ambient air as indicated by the arrows in Fig. 3.1.12a. The entrainment by the induced velocity can be deduced from the cross-stream velocity contours, which show vertically induced velocity with opposite sign as shown in Fig. 3.1.12b. Thus, two opposite actions of deceleration and acceleration take place around a vortex ring. These combined effects are most likely responsible for the periodic changing of the centerline velocity.

As discussed earlier, the development of TKE along the jet centerline for the $m = 0$ case was monotonic (Fig. 3.1.10a). The amplification of the centerline TKE is governed by the interaction between the vortices and the jet column. For odd-numbered modes, the flapping action of the jet plume across the jet centerline would increase the turbulence level. For $m = 0$ case, the vortex rings grew monotonically and their identities were preserved for long downstream distances. These seems to be the cause for the monotonic development of TKE for $m = 0$.

For $m = 1$ case, the vortical structures are smaller and weaker than those for $m = 0$ or $m = \pm 1$. The vortex generated at this mode is helical and thus the coherence level in the cross-stream direction is smaller than $m = 0$ or $m = \pm 1$, where the generated vortices are vortical rings or spanwise structures, respectively. The jet column undulation and the induced velocity around a vortex are similar to those for the $m = \pm 1$ mode, as can be seen in Figs. 3.1.11 - 12. Thus, it is expected that the vortex dynamics at this mode to be similar to those at $m = \pm 1$ since the vortex patterns are very similar. However, the interaction between vortices across the jet column and cross-stream velocity induced by self-induction are expected to be slightly weaker than those at $m = \pm 1$. This reduced interaction and induced velocity may be responsible for the reduced jet spreading as shown in Fig. 3.1.7c.

The development of anisotropy was discussed earlier (Fig. 3.1.10b) and showed the streamwise velocity fluctuations to be largest for the axisymmetric modes (even numbered modes). As can be inferred from Fig. 3.1.12, the cross-stream velocity fluctuations are suppressed because of the symmetric nature of the vortices across the jet centerline as shown in Fig. 3.1.12b. The induced velocity on the upstream side of a pair of vortices on the top and bottom shear layers is downward and upward, respectively, as indicated by arrows in Fig. 3.1.12b. Also the streamwise velocity fluctuation is more likely amplified due to self- or mutual-induction. This explains why the anisotropy is decreased for the even numbered modes. On the other hand, the induced cross-stream velocity fluctuations are in the same direction at a given x/D for the odd numbered modes as observed in Fig. 3.1.12d. This leads to more amplification in the cross-stream velocity fluctuations, and is responsible for the increased anisotropy for the odd numbered modes. The level of interaction across the jet centerline can be higher earlier for the even numbered modes than

for the odd numbered ones as can be observed in Figs. 3.1.12a and d. This is associated with the earlier or later saturation of anisotropy for the even or odd numbered modes, respectively.

As discussed in Sec. 3.1.3, the centerline Mach number distribution for $m = \pm 2$ is comparable to that of $m = \pm 1$ although the jet spreading is not. The vortex dynamics can offer some clues for this difference. Galilean streamlines superimposed on streamwise and cross-streamwise velocity components are shown in Fig. 3.1.13 for two phases. The bottom images are 180° out of phase relative to the top ones. The arrows in Fig. 3.1.13a indicate the center of two adjacent vortices. However, the arrows at the same x/D location in Fig. 3.1.13c point to a location between two consecutive vortices because the two images are out of phase. Although the vortex pattern is similar to that of the $m = 0$ mode, the vortices at this mode are expected to be quasi-two-dimensional since the actuators on the vertical and horizontal planes are operated out of phase. This will be further discussed later using cross-stream velocity fields.

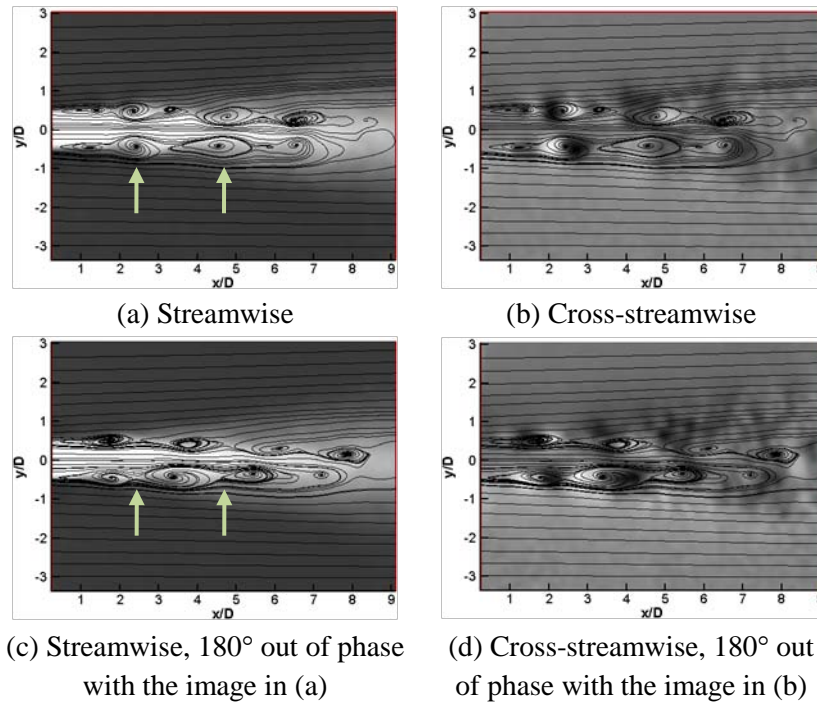
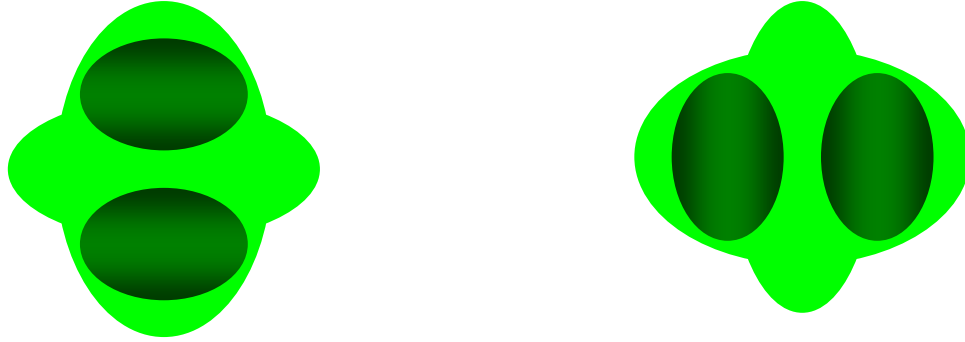


Fig. 3.1.13 Conditionally-averaged Galilean-decomposed velocity components with superimposed streamlines for $m = \pm 2$.

The following discussion is based on the assumption that the generated vortices are spanwise or at least quasi-spanwise. This is confirmed by taking images in the visualized cross-section (not shown) of an ideally expanded Mach 1.3 jet at $x/D = 4$. The high-speed jet column is squeezed in the vertical direction between a pair of horizontally aligned vortices at the location indicated by the two arrows in Fig. 3.1.13a. The corresponding jet cross-section is shown schematically in Fig. 3.1.14a. In a half cycle of the forcing period, a vertically oriented pair of vortices pass through the same downstream location (indicated by the arrows in Fig. 3.1.13c) and causes the high-speed plume to be squeezed vertically as shown schematically in Fig. 3.1.14b). This alternating squeezing action by vertically and horizontally aligned pairs of vortices is probably responsible for the relatively fast decay of the jet centerline Mach number.

On the other hand, it is expected that the mixing/spreading performance of pairs of vortices at this mode would not be large, as the vortices are symmetric across the jet centerline as explained for the $m = 0$ case.



(a) At an x/D location indicated by an arrow in Fig. 3.1.13a (b) At an x/D location indicated by an arrow in Fig. 3.1.13c

Fig. 3.1.14 Schematic of the jet cross-section for $m = \pm 2$. The light gray tone represents the jet cross-section and the darker ellipses indicate large-scale structures.

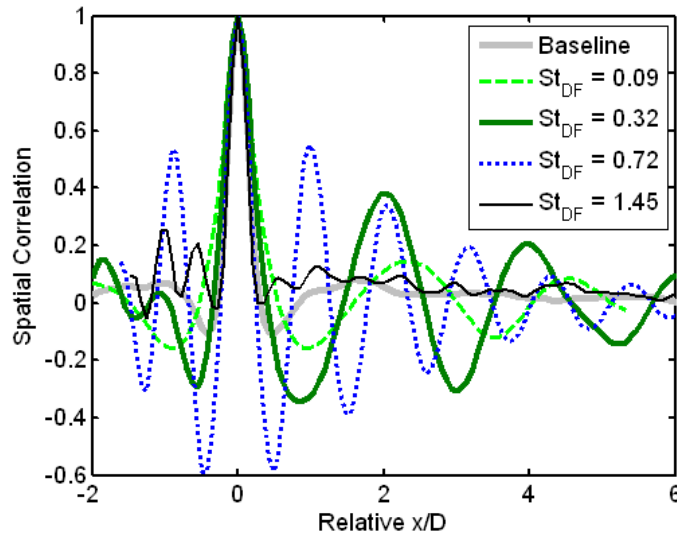


Fig. 3.1.15 Spatial correlation along the lip-line of the jet for several Strouhal numbers at $m = \pm 1$ mode.

3.1.6 Convection Velocity of Large-Scale Structures

The convection velocity of the generated structures due to forcing was calculated by the method discussed in the earlier section. A correlation window in an instantaneous velocity field was selected, covering approximately 75 – 125 % of the streamwise spacing of two adjacent large-scale structures and the entire width of the shear layer. As in Samimy et al. [2007], one can get the spatial-correlation profiles along any streamwise line, e.g. the jet lip-line, from such two dimensional spatial-correlations. The spatial-correlation profiles for several Strouhal numbers are shown in Fig. 3.1.15 for $m = \pm 1$. When there are periodic structures in the shear layer, the spatial correlation is similar to an amplitude-modulated sinusoidal wave. For the baseline jet, there is no periodic motion. When the jet was forced, large-scale periodic structures are generated as indicated by the multiple local peaks of the amplitude-modulated

sinusoidal wave. As discussed earlier, the peak-to-peak distance is the wavelength (spacing) of the generated structures. The convection velocity is obtained by multiplying the calculated wavelength by the forcing frequency. The calculated convection velocity for three forcing modes of $m = 0, 1$, and ± 1 are shown in Fig. 3.1.15.

As the St_{DF} is increased, the normalized convection velocity is increased for all three modes as shown in Fig. 3.1.16. At the lowest forcing Strouhal number, the convection velocity is close to the theoretically predicted value of 0.52. It seems that the normalized convection velocity converges to about 0.77 at a St_{DF} 's greater than about 0.72. The present normalized convection velocity, calculated from instantaneous velocity fields, is slightly larger than that obtained from qualitative flow visualization results in a Mach 1.3 jet for St_{DF} 's of 0.3-0.65 [Samimy et al. 2007]. Their results showed a constant value of 0.67 over this Strouhal number range. The convection velocity measured in a supersonic round jet at Mach numbers from 1.6 to 1.86 was from 0.7 to 0.78 [Petitjean et al. 2006], which agrees well with the present results at higher Strouhal number forcing cases. They used a two-point space-time correlation based technique to calculate convection velocity in the cold jet. Bridges [2006] also measured convection velocity in cold and heated circular jets by using a dual-PIV system. The normalized convection velocity in his case is 0.75 at an acoustic Mach number 0.9 in a cold jet. His results also compare well with the present results at higher St_{DF} 's. In a forced jet by glow discharge, the normalized convection velocity measured by Troutt and McLaughlin [1982] is about 0.8 for a St_{DF} of 0.3 -0.8 in a Mach 2.1 jet. Although their results compare well with the present values at higher Strouhal numbers, they did not see an increase in convection velocity as the St_{DF} was increased from 0.3 to 0.8, which potentially could indicate the lack of actuator authority to force the jet column instability.

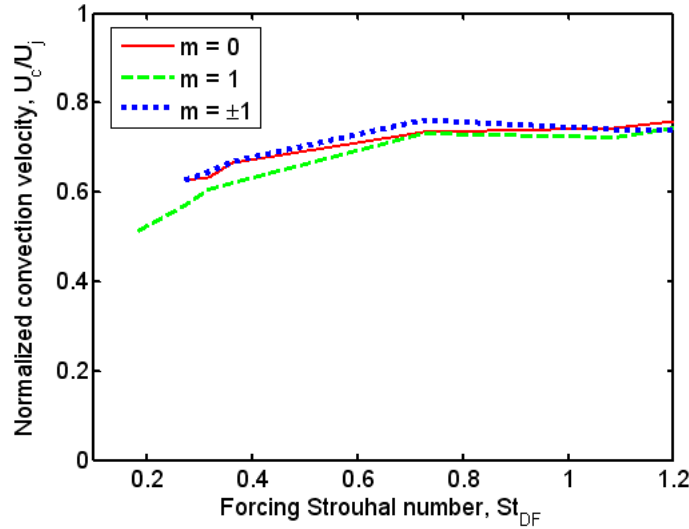


Fig. 3.1.16 Convection velocity for three modes.

3.2 Mach 1.3 Cold Supersonic Jet

As in the results in the Mach 0.9 cold jet, the performance of the plasma actuators is evaluated by PIV measurements. The centerline Mach number decay and the jet width (δ), defined by the full width at half maximum (FWHM) of the streamwise velocity, is used for overall performance evaluation. The spacing and convection velocity of generated large-scale structures is obtained from spatial cross-

correlation and these are used for conditional sampling of PIV images. The large-scale structures are visualized by using conditionally-sampled Galilean velocity fields (the coordinate systems are moving with the convective velocity of large-scale structures). From this information about large-scale structure, the role of the generated structures in the jet development is discussed extensively. The jet flow fields are measured at $M_J = 1.2$ (overexpanded), 1.3 (perfectly expanded), and 1.4 (underexpanded). The results for the perfectly expanded jet ($M_J = 1.3$) are very similar to those in Mach 0.9 cold subsonic jet as will be detailed later.

3.2.1 Effects of Forcing Strouhal Number on Overall Jet Mixing

The results for Mach 0.9 subsonic [Kim et al. 2007, 2009] and perfectly-expanded Mach 1.3 supersonic [Samimy et al. 2007] jets showed that the forcing is most effective at $m = \pm 1$. Thus, the results at $m = \pm 1$ are used for the evaluation of the effects of St_{DF} numbers on the jet spreading for all M_J 's. Average streamwise velocity contours for $m = \pm 1$ are shown in Fig. 3.2.1 for three fully-expanded jet Mach numbers of 1.2 (over-expanded), 1.3 (perfectly-expanded), and 1.4 (under-expanded). The streamwise velocity is scaled from -40 m/s to the maximum for each Mach number. The maximum jet velocity is about 360, 380, and 420 m/s for $M_J = 1.2, 1.3$, and 1.4, respectively. Thus, no information can be gained from a one-to-one comparison of the colors in plots of differing Mach number.

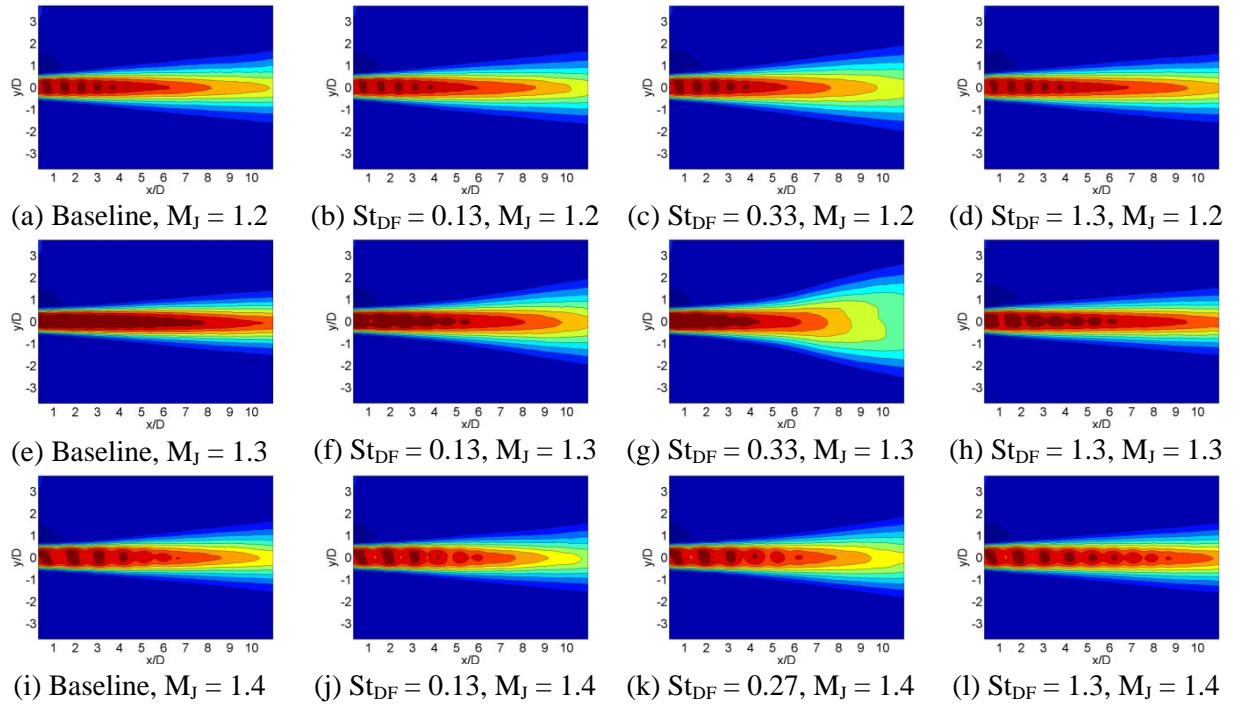


Figure 3.2.1 Average streamwise velocity contours for various St_{DF} numbers at three jet Mach numbers. The maximum velocity of the jet is about 360, 380, and 420 m/s for Mach = 1.2, 1.3, and 1.4 jets, respectively.

The baseline/unforced jets show that the jet spreading is increased at the off-design jets of $M_J = 1.2$ and 1.4. The enhanced spreading is due to the feedback mechanism sustained by upstream-traveling acoustic waves and downstream traveling large-scale structures/hydrodynamic waves in the jet shear layers that interact with the shock waves generating the acoustic waves. A strong tone is also generated by the feedback mechanism in all three cases, as shown in Figure 3.2.2. For the imperfectly-expanded jets,

the broadband shock associated noise (broad humps in the spectra) is significantly increased. However, the shock associated broad noise is not significant in the perfectly expanded jet (Fig. 3.2.2b). The shock cell patterns are clearly seen in the average streamwise velocity contours for the imperfectly-expanded jet (Figures 3.2.1a & i). Thus, the shock strength is less in the perfectly-expanded jet than in the imperfectly-expanded jet. This can be more clearly observed in the centerline Mach number to be presented later.

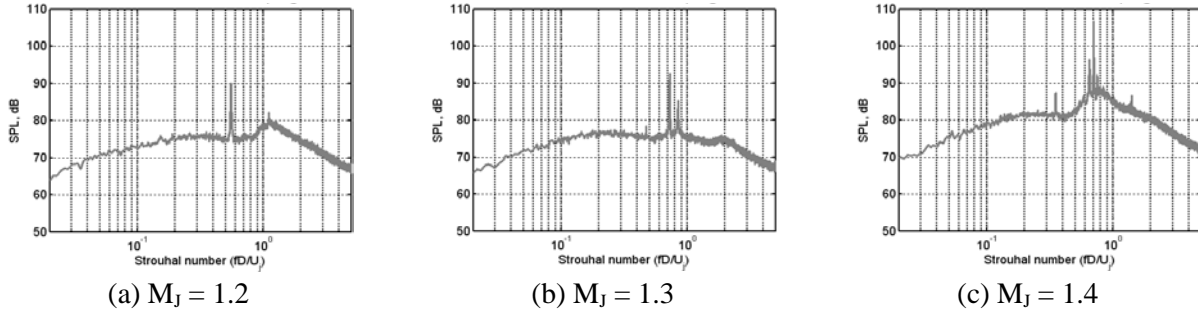


Fig. 3.2.2 Average spectra at $M_J = 1.2, 1.3$ and 1.4 , measured at 90° relative to the jet centerline.

For the over-expanded jet ($M_J = 1.2$), the effect of forcing is not apparent at a low St_{DF} of 0.13. The maximum spreading occurs at a St_{DF} of 0.33 (Fig. 3.2.1c), but the enhancement of jet spreading is moderate. At a higher St_{DF} of 1.3 (Figure 3.2.1d), it appears that the jet spreading is even suppressed. The contours for the under-expanded jet (Figures 3.2.1 i-l) show that the trend of jet spreading with St_{DF} is roughly similar to that for the over-expanded jet. For this flow regime, the maximum spreading is at a slightly low St_{DF} of 0.27 (Figure 3.2.1k). As will be further discussed, the forcing is less effective in the imperfectly-expanded jets when compared to the perfectly-expanded Mach 1.3 jet.

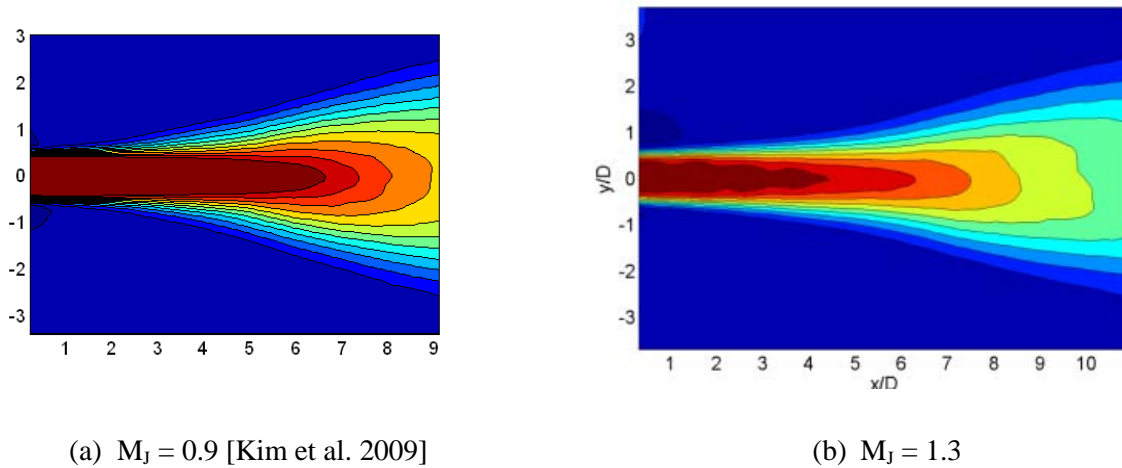


Figure 3.2.3 Average velocity contours in the flapping plane at $m = \pm 1$ and $St_{DF} \approx 0.3$. The scale is about the same, but the spans in streamwise and cross-streamwise directions are different.

For the perfectly expanded jet ($M_J = 1.3$), the jet responds to the forcing in a wide range of St_{DF} 's. At a low St_{DF} of 0.13, the jet spreading is significantly enhanced, contrary to the imperfectly-expanded cases. The maximum spreading is observed at a St_{DF} of 0.33 (Figure 3.2.1g) and the enhancement in the jet spreading is dramatic. At a high St_{DF} of 1.3, the velocity contour is very similar to that of the baseline,

implying that forcing is not effective at high St_{DF} 's. The trend observed at the perfectly-expanded Mach 1.3 supersonic jet is very similar to what was observed in a subsonic M_j 0.9 jet [Kim et al. 2009a & b].

Figure 3.2.3 shows the streamwise velocity contours measured by the PIV system for Mach 0.9 and 1.3 jets, respectively, at a St_{DF} of about 0.3 and at $m = \pm 1$. Note that the color map is not the same – the same color does not represent the same velocity. The jet exit velocity is about 280 and 380 m/s for $M_j = 0.9$ and 1.3, respectively. In both jets, the actuators have control authority and the enhancement of mixing/spreading (spreading from here on) is about the same. As will be further discussed in a later section, the nature and role of generated structures in the jet development are also about the same.

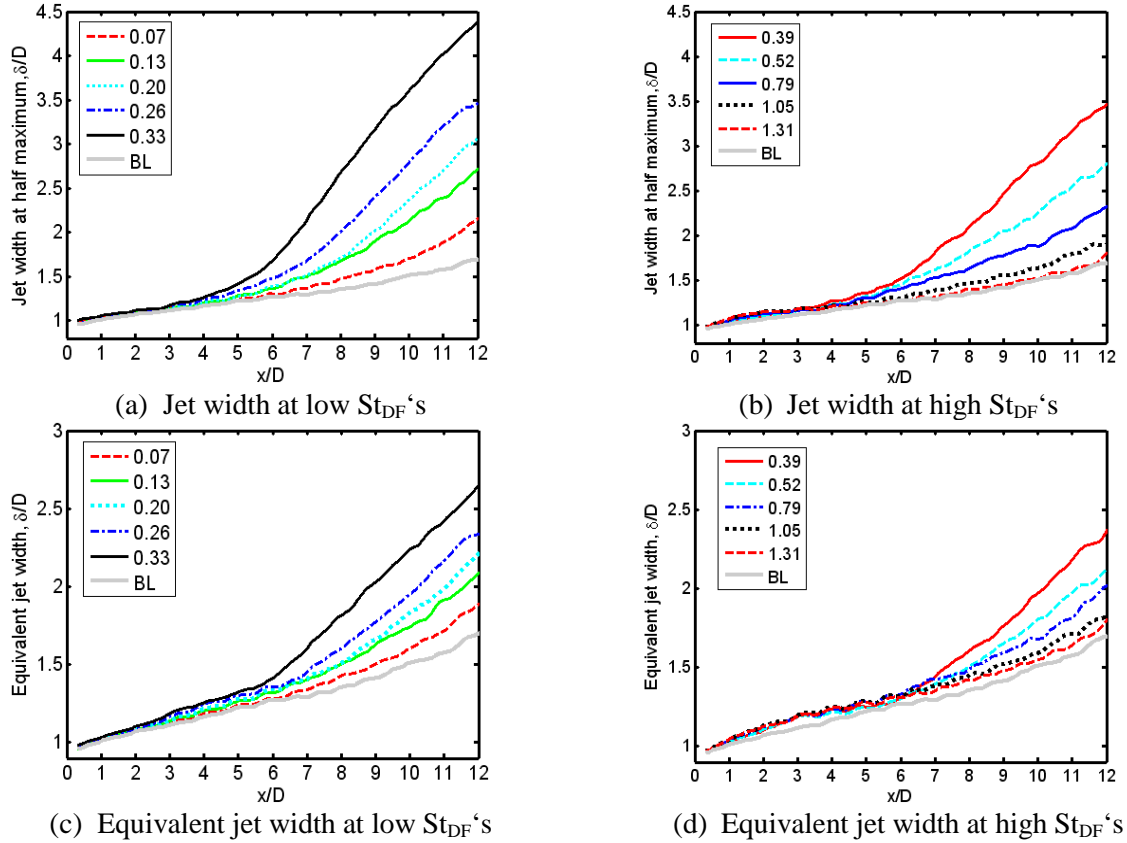


Fig. 3.2.4 Jet width development at $m = \pm 1$ for various St_{DF} numbers.

The effects of forcing Strouhal number will be more extensively presented by examining jet width and jet centerline Mach numbers. For $M_j = 1.3$, the jet width development at $m = \pm 1$ is shown in Fig. 3.2.4 at various St_{DF} 's. The jet width in Figs. 3.2.4a&b is on the flapping plane, which shows the effects of forcing Strouhal number. The jet width on the non-flapping plane (not shown here) does not show any significant spreading. Thus, the cross-section of the jet plume is elliptic at this forcing mode. An equivalent jet width, defined as the geometric average of the jet width in the flapping and non-flapping planes (square root of the multiplication of two jet widths), is shown in Figs. 3.2.4c&d. One could then compare this jet width with those of other modes, which are axisymmetric in the average sense. As in the $M_j = 0.9$ subsonic jet [Kim et al. 2009], the jet plume spreading was significantly enhanced by forcing. As the St_{DF} number is increased, the spreading also increases up to $St_{DF} \approx 0.3$ as shown in Figs. 3.2.4a & c. When the St_{DF} number is further increased, the jet spreading is decreased as shown in Figs.

3.2.4b & d and more visually in Fig. 3.2.1h. Thus, the enhancement of the jet width is greatest at $St_{DF} \approx 0.3$. At high St_{DF} 's greater than 1.31, the jet width development is about the same as that of the baseline as can be seen also in Figs. 3.2.1e&h. The trend of jet spreading with St_{DF} 's is more readily seen in Fig. 3.2.5, showing the jet widths at $x/D = 10$ for $m = \pm 1$. In the figure, the jet width for the forced cases is normalized by that for the baseline. The normalized jet width increases rapidly at St_{DF} 's approaching 0.33. For St_{DF} 's greater than 0.33, the normalized width decreased with increasing St_{DF} 's as was seen in Figs. 3.2.1 and 3.2.4. The jet width at $M_J = 0.9$ for $m = \pm 1$ (Fig. 3.1.4) is very similar to that at $M_J = 1.3$ shown in Fig. 3.2.4. These results show that the performance of the actuators is about the same in both Mach 0.9 subsonic and perfectly-expanded Mach 1.3 jets.

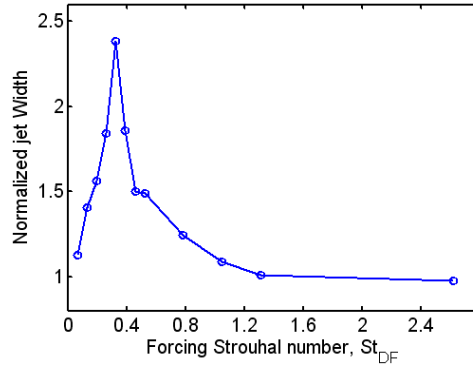


Fig. 3.2.5 Normalized jet widths on the flapping plane at $x/D = 10$ for $m = \pm 1$. The jet width at each St_{DF} number was normalized by that for the baseline.

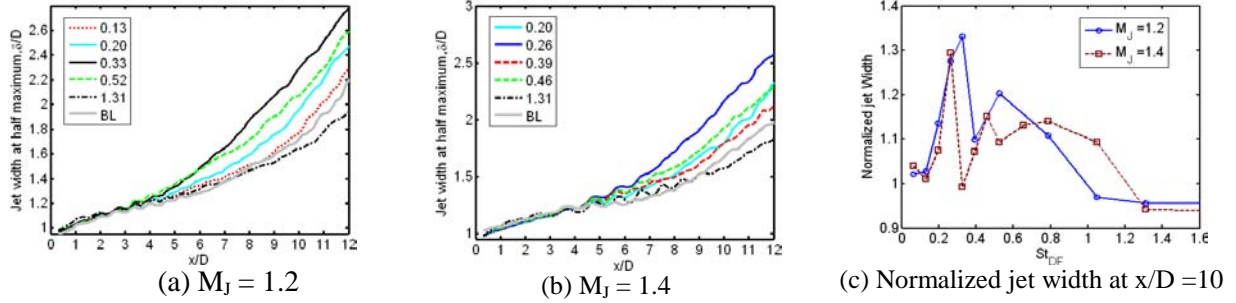


Fig. 3.2.6 Jet width development on the flapping plane at $m = \pm 1$ for the imperfectly-expanded jets.

For the imperfectly-expanded Mach 1.2 & 1.4 jets, the jet width development with downstream location at $m = \pm 1$ is shown in Figure 3.2.6. In both jets, the jet width increases at low St_{DF} 's less than about 0.3. The enhancement of jet spreading is maximum at St_{DF} numbers 0.33 and 0.26 for $M_J = 1.2$ and 1.4, respectively. The jet width shows a dip and secondary peak at high St_{DF} numbers when the St_{DF} number is increased further from the maximum (Fig. 3.2.6c), which was not seen in the perfectly-expanded jet (Fig. 3.2.5). For some other azimuthal modes (not shown here), the normalized jet width is undulating with St_{DF} numbers. This difference in jet width trend is possibly due to the interaction of the forced and naturally amplified (by the feedback loop) structures as will be further discussed later. At St_{DF} 's greater than 1.0, the jet width is reduced by forcing as was also observed in the velocity contours in

Fig. 3.2.1. The overall enhancement of jet spreading is not as significant as in the perfectly-expanded jets. It seems that the reduction in jet spreading at high St_{DF} numbers and overall spreading is also associated with the interaction of the forced and naturally occurring structures.

Table 3. Optimal St_{DF} numbers, showing maximum jet spreading at each azimuthal mode.

Azimuthal mode	$M_J = 1.2$	$M_J = 1.3$	$M_J = 1.4$
$m = 0$	0.52	0.52	0.33
$m = 1$	0.26	0.39	0.26
$m = 2$	0.26	0.33	0.06
$m = 3$	0.20	0.13	0.26
$m = \pm 1$	0.33	0.33	0.26
$m = \pm 2$	0.52	0.33	0.46

For other azimuthal modes, the optimal St_{DF} numbers are selected from the normalized jet width at $x/D = 10$ and are shown in Table 3. For the most cases, the optimal St_{DF} number is about 0.3. Exceptionally low numbers are seen at 0.13 for $M_J = 1.3$ & $m = 3$ and 0.06 for $M_J = 1.4$ & $m = 2$. In the $M_J = 0.9$ subsonic jet, the optimal St_{DF} number was lower than any other modes as in the $M_J = 1.3$ perfectly-expanded supersonic jet. For other cases, the numbers are within 0.2-0.6 range, found in the literature.

3.2.2 Effects of azimuthal modes

3.2.2.1 Perfectly-expanded jet

The results presented in the earlier section showed the effects of St_{DF} numbers at $m = \pm 1$. In this section, the effects of azimuthal modes will be discussed by using optimal cases; those that show the most jet spreading. For the perfectly-expanded jet, the average streamwise velocity contours at the optimal St_{DF} numbers, listed on Table 2, are shown in Fig. 3.2.7. Also, the profiles of the centerline Mach number and jet width are shown in Figure 3.2.8 for the optimal St_{DF} 's. Note that an equivalent jet width is used only for $m = \pm 1$ since the jet cross-section is elliptic for this mode. The streamwise velocity contours and centerline Mach number show that the jet potential core length is shortened significantly for $m = 1$ and ± 1 , and moderately for the other modes. The potential core length is reduced from 7 nozzle diameters in the baseline jet to 4 (for $m = 1$ & ± 1) and 5.5 (for the rest of modes). Although both the potential core length and centerline Mach number are indirect measures for the jet growth/spreading, the trend observed in Figs. 3.2.7 and 3.2.8a is very similar to what is seen in the jet width, a direct measure for the spreading. There is a moderate undulation in the centerline Mach number due to weak shock cells. Although the diverging section of the nozzle was designed by the method of characteristics, the occurrence of weak shocks is unavoidable with a thick lipped nozzle. For all azimuthal modes, the centerline Mach number decay is enhanced by forcing. The results in Figs. 3.2.7-8 show that the most effective forcing is at $m = \pm 1$ as in the $M_J = 0.9$ subsonic jet (Sec. 3.1). At this mode, a dramatic enhancement in jet spreading is manifested in accelerated centerline Mach number decay and enhanced jet width. Additionally, the spreading at $m = 1$ is substantially improved. For the rest of the azimuthal modes, the enhancement in jet spreading is moderate.

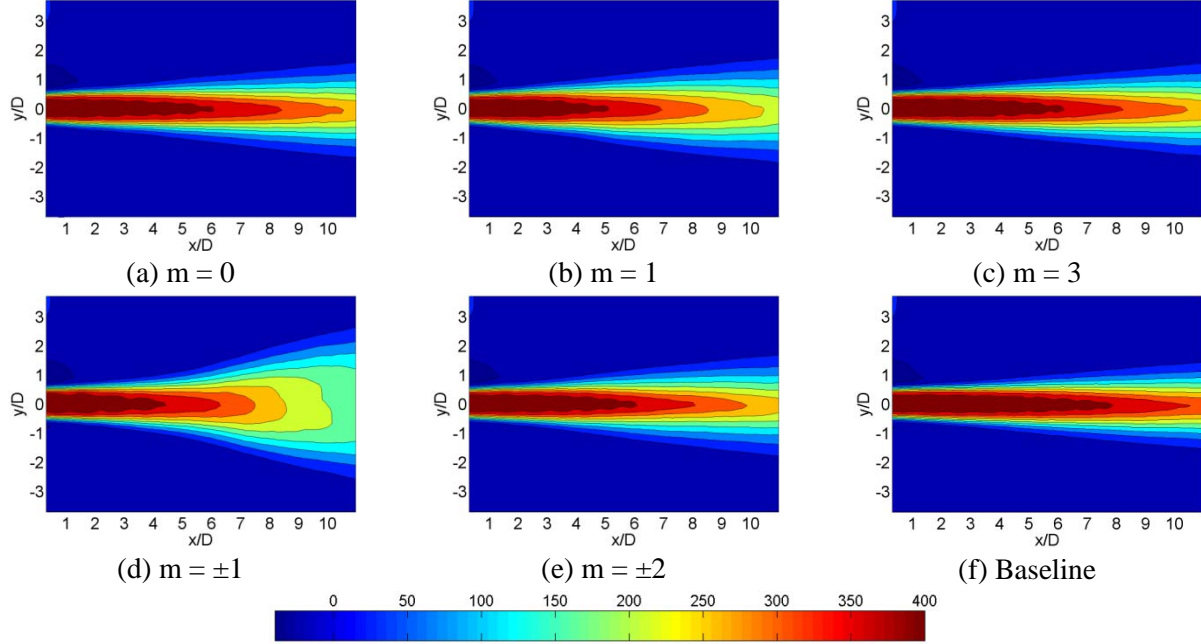


Fig. 3.2.7 Average streamwise velocity contours at the optimal St_{DF} 's, listed in Table 2, for each azimuthal mode.

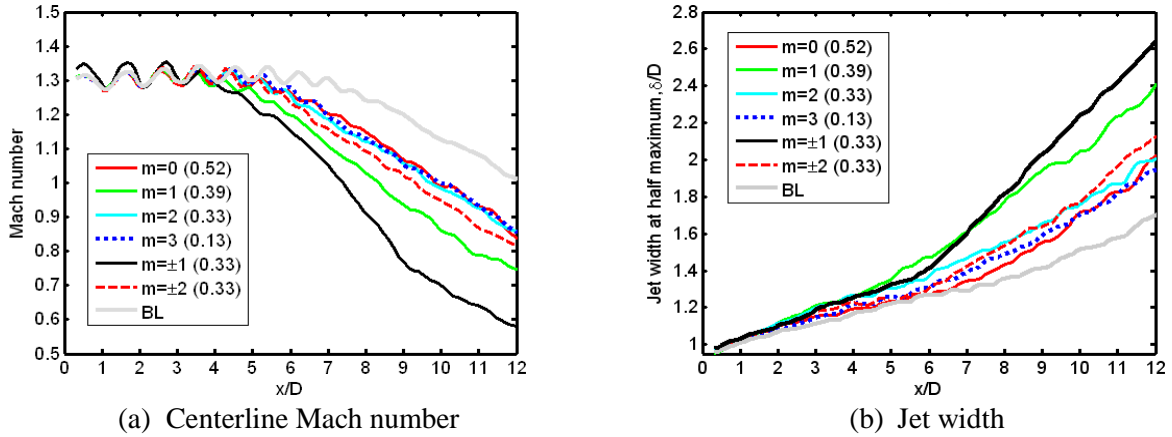


Fig. 3.2.8 Comparison of the centerline Mach number and jet width at $M_J = 1.3$. For $m = \pm 1$, the jet width is the equivalent width. The forcing Strouhal number is shown in the legend of each figure.

The results in the perfectly-expanded M_J 1.3 jet are largely similar to those in M_J 0.9 subsonic jets [Kim et al. 2009]. However, the jet growth at $m = \pm 2$ is significantly reduced compared to those in Mach 0.9 jets. In the M_J 0.9 jet, the increase in centerline Mach number decay was similar for both $m = \pm 2$ and $m = \pm 1$ cases. In the perfectly-expanded Mach 1.3 jet, the jet growth at $m = \pm 2$ is about the same as the moderately effective group of modes ($m = 0$, & 2-3). At this point, it is not clear why the performance at $m = \pm 2$ was reduced in M_J 1.3 jets. Another difference is the growth in the initial shear layer. In the M_J 0.9 subsonic jet, a significant enhancement in jet width in the initial shear layer was seen for many azimuthal modes at a relatively high St_{DF} of about 1.0 (see Fig. 3.1.7) [Kim et al. 2007, 2009]. For the perfectly-expanded M_J 1.3 jet, the enhancement in jet width in the initial shear layer is only seen at $m = 3$

(shown in Fig. 3.2.9) and is not as significant as in the subsonic counterpart. The increased jet width upstream of the end of potential core is thought to be due to growths of the structures generated by forcing.

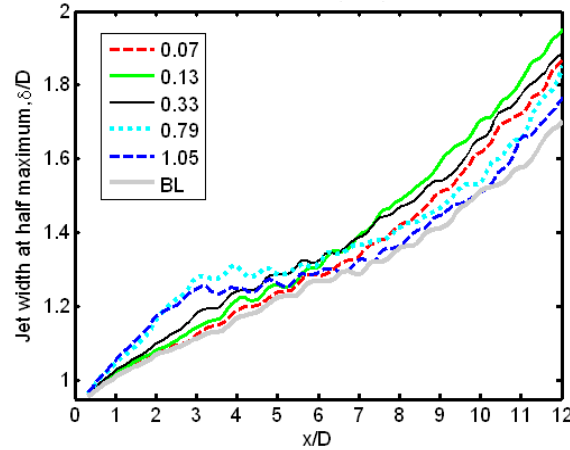


Fig. 3.2.9 Jet width development along the streamwise direction at $m = 3$.

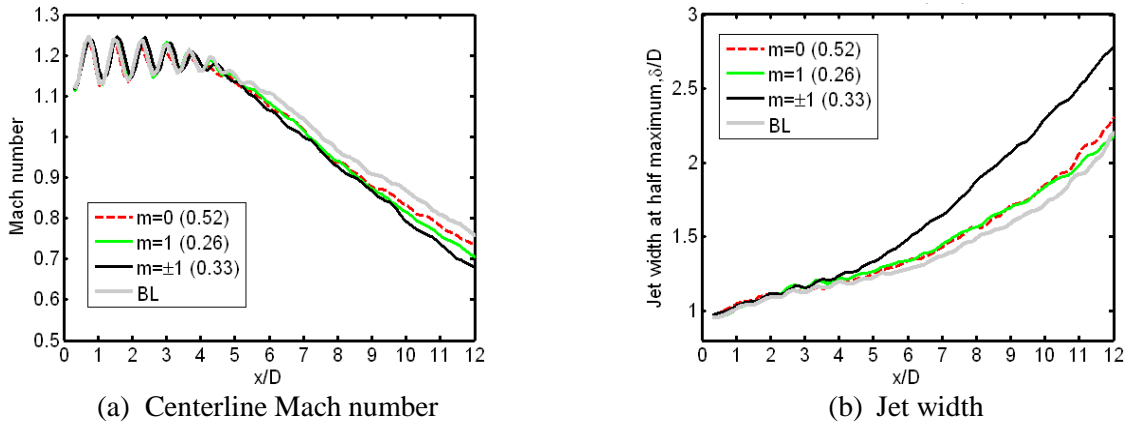


Fig. 3.2.10 Comparison of the centerline Mach number and jet width at $M_j = 1.2$. The jet width for $m = \pm 1$ is on the flapping mode. The forcing Strouhal number is 0.52, 0.26, and 0.33 for $m = 0, 1$, and ± 1 , respectively.

3.2.2.2 Imperfectly-expanded jets

The centerline Mach number and jet width development for two modes of $m = 0$ and 1 are compared to show the effects of azimuthal mode in the over-expanded jets (Fig. 3.2.10). In this figure, the St_{DF} number for each azimuthal mode is selected for the maximum jet spreading as listed in Table 3. In the over-expanded $M_j = 1.2$ jet, the centerline Mach number is a better measure for the overall jet spreading since no measurement is done on the non-flapping plane for the $m = \pm 1$ case. Neither the potential core length, obtained from Fig. 3.2.10a, nor the centerline Mach number decay rate beyond the

end of potential core is significantly altered by forcing. The ineffectiveness of forcing in the over-expanded jet is also manifested in the average streamwise velocity contours shown in Fig. 3.2.11. The shock cell patterns in the potential core region and jet growth are barely changed by forcing. However, the jet width on the flapping plane at $m = \pm 1$ shows a notable increase, suggesting that large-scale structures are generated. However, it seems that the generated large-scale structures lack the strength to significantly excite the shock containing jet and so do not increase mixing. This will be discussed further later. For the other modes not presented here, the spreading is about the same as that for $m = 0$ or 1. These results show that the forcing in the over-expanded jet is not as effective as in the perfectly-expanded jet.

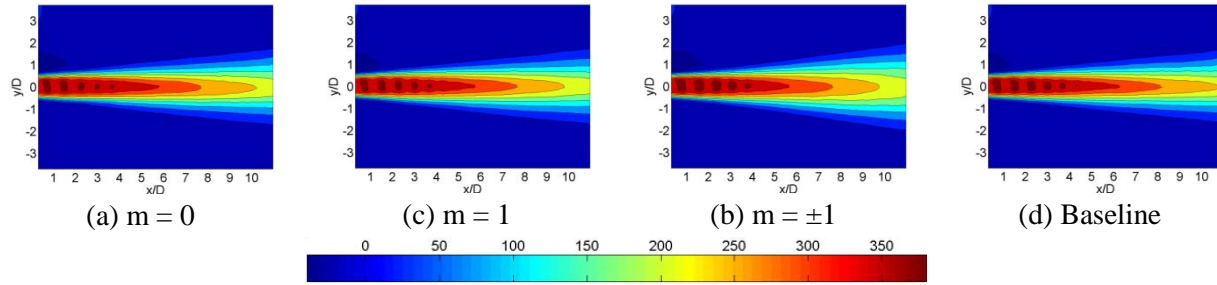


Fig. 3.2.11 Average streamwise velocity contours in the over-expanded jet ($M_j = 1.2$).

For the under-expanded $M_j = 1.4$ jet, the centerline Mach number and jet width are shown in Fig. 3.2.12 for $m = 0, 1$, and ± 1 . For the other modes not shown here, the centerline Mach number and jet width are very similar to that for $m = 1$ and $m = 0$, respectively. Again, in this figure, the forcing Strouhal number for each azimuthal mode is selected for the maximum jet spreading as listed in Table 3. The centerline Mach number undulates between 1.3 and 1.5 due to periodic shock cell structures in the jet. The jet potential core length and centerline Mach number decay are not significantly changed by forcing, as in the over-expanded jet. The jet width is increased slightly by forcing, but the increase is not as significant as in $M_j = 0.9$ subsonic (Sec. 3.1) or ideally expanded $M_j = 1.3$ jets. The jet width enhancement at $m = \pm 1$ seems significant, but note that the non-flapping plane width, which would be very close to that for the baseline, is not taken into account. The equivalent jet width is expected to be very close to that for the $m = 0$. This explains why the centerline Mach number decays for $m = 1$ and ± 1 are very close to each other as seen in Fig. 3.2.12a. The reduced jet spreading over the baseline jet is partially due to enhanced mixing in the baseline/unforced jet as discussed earlier (Figs. 3.2.1a,e,&i).

In $M_j = 1.4$ jets, the centerline Mach number decay is slightly suppressed for all azimuthal modes except for $m = \pm 1$, as shown in Fig. 3.2.12a. For $m = 0$, the centerline Mach number decay is significantly reduced and the jet width development is almost the same as the baseline. In the $M_j 0.9$ subsonic jet (Sec. 3.1), it was shown that vortex rings were generated at $m = 0$, and that the centerline velocity decay and jet spreading were reduced due to self induction and axisymmetric nature of the vortex ring [Kim et al. 2007 & 2009].

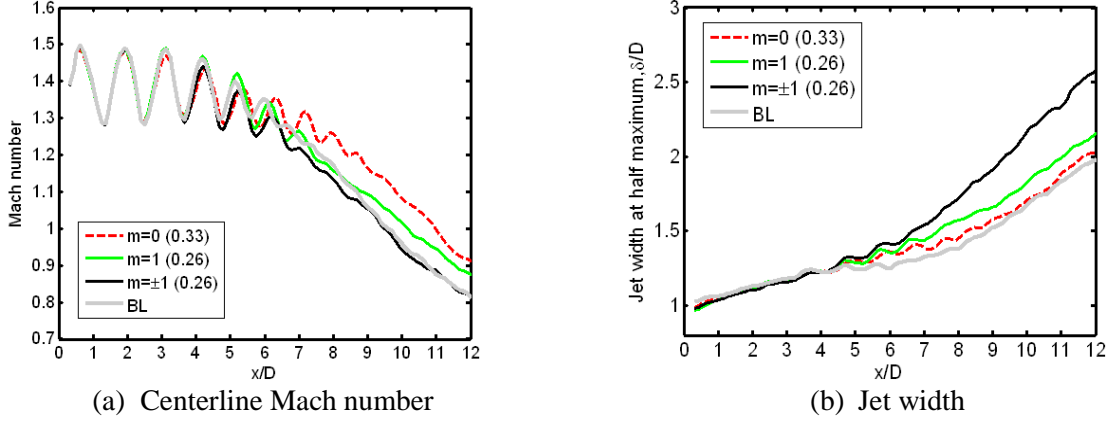


Fig. 3.2.12 Comparison of centerline Mach number and jet width at $M_J = 1.4$. The jet width for $m = \pm 1$ is on the flapping mode. The number in the parentheses indicates the forcing Strouhal number for each azimuthal mode.

3.2.3 Effects of Forcing on Turbulence

This section examines the development of jet centerline two-dimensional turbulent kinetic energy (TKE henceforth), as only a two-component PIV system was utilized. The effects of forcing Strouhal number on TKE is shown in Fig. 3.2.13 in the perfectly-expanded jet. The TKE level is significantly increased at a St_{DF} number near of 0.3, but its level is close to that for the baseline at low (not shown here) and high St_{DF} numbers (1.31, for an example). For the St_{DF} of 0.33 which showed maximum jet growth, the TKE level saturates at $x/D = 8$ and then slowly decays. At other St_{DF} 's, the TKE level increases almost monotonically without showing any saturation in the entire streamwise measurement span. This trend was not observed in the MJ 0.9 subsonic jet, where TKE saturated at $x/D = 7$ at low St_{DF} 's (Fig. 3.1.10).

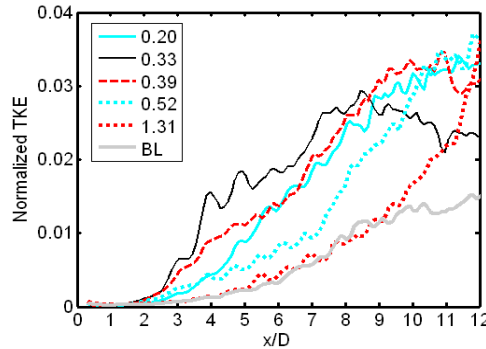


Fig. 3.2.13 Turbulent kinetic energy development at $m = \pm 1$ in the perfectly-expanded jet.

Figure 3.2.14 shows the effects of azimuthal modes for three flow regimes of $M_J = 1.2$, 1.3, and 1.4. The cases shown in the figure are for forcing Strouhal numbers that achieved maximum spreading for each mode, listed in Table 3. The forcing Strouhal numbers for each mode correspond to those shown Figs. 3.2.8, 3.2.10, and 3.2.12, respectively. For $M_J = 1.3$, TKE is significantly increased for all forcing modes as in the M_J 0.9 subsonic jet. The increase in TKE level in the M_J 1.3 supersonic jet is a little bit less than that in the M_J 0.9 subsonic jet (compare Figs. 3.1.10a and 3.2.14a). The TKE saturates at $x/D =$

8.5 and 10.5 for $m = \pm 1$ and 1, respectively. This suggests that the earlier saturation of TKE indicates increased jet growth/spreading. As in a $M_J = 0.9$ subsonic jet, the TKE is still on the rise for $m = 0$. This is due to self-induction by vortex rings and the symmetric nature of the generated structures in this mode [Kim et al. 2007 & 2009], as discussed in Sec. 3.1.

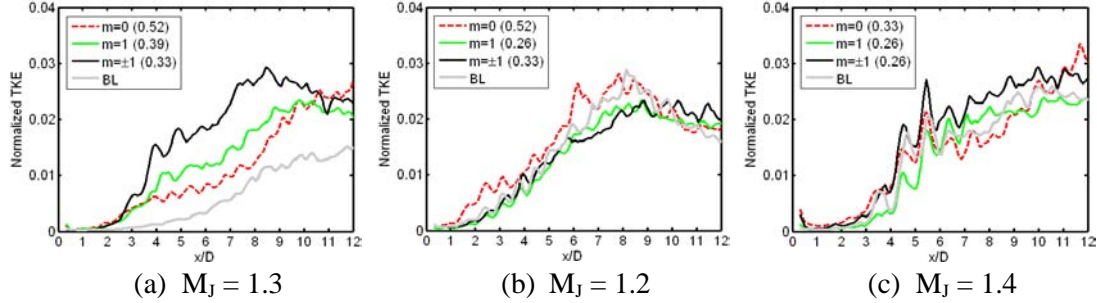


Fig. 3.2.14 Two-dimensional turbulent kinetic energy development for three azimuthal modes $m = 0, 1$, and ± 1 .

For imperfectly-expanded jets of $M_J = 1.2$ and 1.4 , it appears that centerline TKE is not significantly altered by forcing as seen in Fig. 3.2.14b & c. This is partially due to increased TKE level in the unforced baseline jets due to the presence of relatively strong shock/expansion train. As was discussed earlier, when the jet operates in imperfectly-expanded regime, a screech tone is generated by a feedback mechanism between the hydrodynamic and acoustic waves (Fig. 3.2.2), and large-scale structures are amplified due to this feedback mechanism resulting in the increase in TKE. If the large-scale structures are suppressed, TKE would be reduced by forcing. This was observed when the jet was forced at high St_{DF} 's (not shown here).

3.2.4 Large-Scale Structures and their role in the Jet Development

Large-scale structures are visualized by using conditionally sampled Galilean velocity field. In the Galilean velocity field, the reference frame moves with the convection velocity of large-scale structures in the flow. Thus, the large-scale structures are stationary in this frame, and they are identified if the streamlines show closed or spiral shapes [Kline and Robinson 1990, Robinson et al. 1989]. The procedure was discussed in more detail earlier.

3.2.4.1 Perfectly-Expanded Jet ($M_J = 1.3$)

Large-scale structures for excitation with $m = \pm 1$ at various Strouhal numbers in the $M_J = 1.3$ jet are shown Fig. 3.2.15. The relative magnitude of the streamwise velocity is represented by color: red and blue indicate fast and slow speeds, respectively. There is no common color map, valid for all images, since the reference frame moves at a different speed for each case. The structures identified by Galilean streamlines are similar to those visualized by laser scattering [Samimy et al. 2007b]. Large periodic structures are generated by forcing at a wide range of St_{DF} 's from 0.2 to 1.05 as in the $M_J 0.9$ subsonic jet (Sec. 3.1). At St_{DF} 's outside of this range, there are no visible periodic structures in the shear layer as shown in Fig. 3.2.15e, as an example. When this figure is compared to the case for $M_J 0.9$ jet (Fig. 3.1.11), the jet spreading and structure formation by forcing are very similar in qualitative sense.

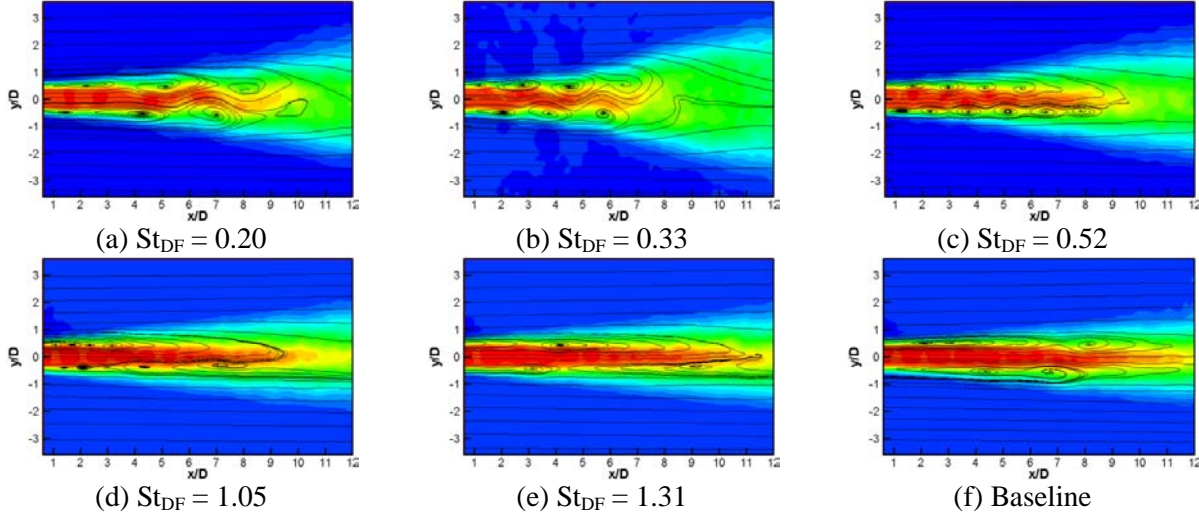


Fig. 3.2.15 Galilean streamlines superimposed on the streamwise velocity fields at $m = \pm 1$ in the $M_J = 1.3$ jet. The velocity fields were conditionally-averaged and the number of images used for the averaging was 30.

At $St_{DF} = 0.33$, the generated structures are very robust and well organized. The generated structures are nearly circular in shape, penetrating into the jet centerline, and causing significant undulation in the jet plume. The potential core length is about four nozzle exit diameters as shown in Fig. 3.2.8a. The potential core is significantly shortened by the entrainment of ambient air and penetration of energetic structures into the jet as seen in Fig. 3.2.15b. Also, the jet spreading is significantly enhanced by the robust structures as shown in Fig. 3.2.8b. The generated structures either decay completely and/or become very disorganized by $x/D = 7$ – no identifiable large structures are seen downstream of this location. As shown in Fig. 3.2.13, the TKE development is saturated at this location and this saturation location is related to the sudden decay of large-scale structures.

At a low St_{DF} number of 0.2, the generated large periodic structures appear to be nearly elliptical with a high aspect ratio aligned in the streamwise direction. This may be due to a limited growth of the structures in the spanwise direction when compared to that at $St_{DF} = 0.33$. Also, the interaction between the generated structures and the jet plume appears to be limited. The monotonic increase in TKE (Fig. 3.2.13) up to x/D of 12 indicates that the interaction between structures is significantly less for this case. This can be inferred from a longer spatial lifetime of the generated structures at $St_{DF} = 0.2$ than at $St_{DF} = 0.33$. Some large structures are seen up to $x/D = 10$ at $St_{DF} = 0.2$ while all structures had decayed by $x/D = 7$ for $St_{DF} = 0.33$. As in $St_{DF} = 0.33$ case, the jet plume is undulating in the lateral direction due to the flapping action caused by the generated structures. However, the undulating motion is not as significant as in $St_{DF} = 0.33$ case due to the less energetic structures. As a result, the mixing enhancement is relatively less significant at this forcing Strouhal number.

At a moderate St_{DF} of 0.52, periodic large structures, with a reduced spacing, are generated. The interaction between generated structures seems minimal, which is inferred from the well-preserved periodic structures and their almost constant dimension up to $x/D = 8$. It seems that the jet plume undulates less since the generated structures are smaller than those at low St_{DF} 's. The reduced undulation of the jet plume suggests that the interaction between the generated structures and the jet plume is not

significant when compared to that at low St_{DF} 's. The reduced TKE at this St_{DF} number, shown in Fig. 3.2.13, also confirms that the interaction was decreased or limited at this moderate St_{DF} .

Interestingly, some periodic structures are observed even at a high St_{DF} number of 1.05 (Fig. 3.2.15d). The generated structures are very small and closely spaced. It appears that these small structures decay faster than those at low St_{DF} numbers, but they are occasionally visible up to $x/D = 8$. At a higher St_{DF} number of 1.3 (Fig. 3.2.15e), no periodic structures are seen and the flow fields are very similar to that of the baseline (Fig. 3.2.15f). In the baseline jet, there are some randomly spaced structures, but they are not energetic so that their effect on the jet plume is minimal. The structures observed in this $M_J = 1.3$ jet are very similar to what were seen in the $M_J = 0.9$ subsonic jet with a Reynolds number of about 0.7×10^6 (Sec. 3.1).

Figure 3.2.16 shows the effects of St_{DF} number on the spacing (and also dimension) of the generated structures. The structure spacing is calculated from two-dimensional spatial correlation of 700 instantaneous velocity fields as detailed in Kim et al. [2009a&b]. The spacing (λ) is inversely proportional to St_{DF} number as shown in Fig. 3.2.16, and the streamwise dimension of the structures also shows the same trend as the structure spacing, as seen in Fig. 3.2.15. The profiles for various azimuthal modes in Fig. 3.2.16 are collapsed into a single curve using the following equation

$$\frac{\lambda}{D} = \frac{a}{St_{DF}} + c \quad (3)$$

where a and c are constants. The figure shows that the structure spacing is strongly dependant on the St_{DF} number, and that effects of azimuthal modes are minimal. Also shown in the figure is that the perfectly-expanded jet responds to the forcing over a range of St_{DF} numbers from 0.2 to 1.3. This strong relation further confirms that the structures seen in Fig. 3.2.15 were generated by the excitation/forcing rather than by any other means.

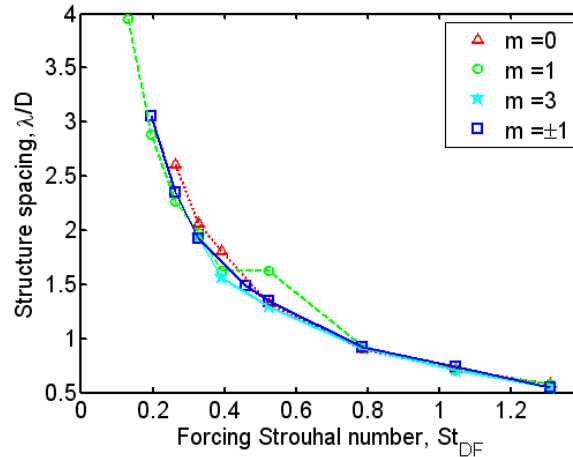


Fig. 3.2.16 Spacing of the generated structures in $M_J = 1.3$ jets.

Figure 3.2.17 shows visualized large-scale structures for $m = 0$ and 1 at St_{DF} numbers showing the maximum spreading for each mode (Fig. 3.2.8 and Table 3). For $m = 0$, the visualized structures are

symmetric across the jet plume since they are vortex rings. The centerline streamwise velocity between a pair of vortical structures (actually inside a vortex ring) is faster due to self induction, but the flow between two neighboring vortex rings is slower due to the entrainment of slow moving ambient air [Kim et al. 2009a&b]. Thus, the streamwise velocity along the jet centerline undulates, similar to what was observed in $M_j = 0.9$ subsonic jet [Kim et al. 2009a]. As in the Mach 0.9 jet, the structures do not penetrate into the jet centerline due to the symmetric nature of the generated structures. Consequently, the interaction of large-scale structures and the jet plume is less destructive. As a result, the centerline Mach number decay is less than in that of any other mode as shown in Fig. 3.2.8a. For $m = 1$, the pattern of the generated structures and jet plume undulation is very similar to that of $m = \pm 1$, but the structures seem less energetic. As a result, the enhancement in the jet width at this mode is less than that of $m = \pm 1$ (Fig. 3.2.8b).

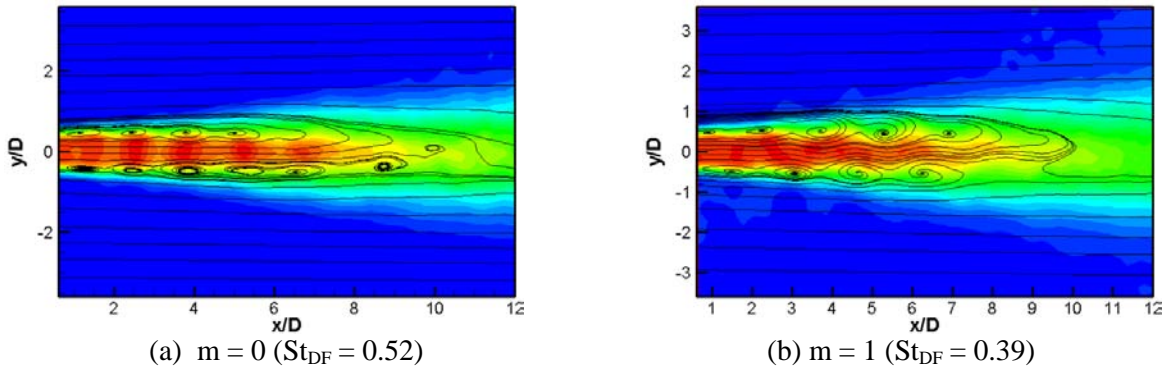


Fig. 3.2.17 Galilean streamlines superimposed on the conditionally-averaged streamwise velocity fields for the cases shown in Fig. 3.2.8 or Table 3.

For other modes not shown here, the generated vortex pattern is very similar to that for $m = 0$ and 1 for even- and odd-numbered modes, respectively. For example, the vortex pattern of $m = 2$ is similar to that at $m = 0$, shown in Fig. 3.2.17a. In Mach 0.9 subsonic jet, the streamwise component of turbulence was more amplified at even-numbered modes, while the cross-streamwise component was more amplified at odd-numbered modes. As discussed in Sec. 3.1, this is due to symmetric or asymmetric nature of the generated structures for even- or odd-numbered modes, respectively [Kim et al. 2009a&b]. All these results show that the effects of forcing on the flow structures and jet development are very similar to what was observed in $M_j = 0.9$ subsonic jet [Kim et al. 2009a]. Thus the discussion of the role of generated structures on the jet development presented in the subsonic case is still valid in this perfectly-expanded $M_j = 1.3$ supersonic jet.

3.2.4.2 Imperfectly-Expanded Jets ($M_j = 1.2$ and 1.4)

Flow visualizations were conducted at $M_j = 1.2$ and 1.4 to investigate whether the plasma actuators are effective in forcing flows containing a shock/expansion train. Some preliminary results presented in Samimy et al. [2007b, 2008] and the results discussed in earlier sections showed that the forcing is less effective in imperfectly-expanded jets (Figs. 3.2.8, 3.2.10, & 3.2.12). The flow visualizations based on the condensed water particle showed that the jet responded to the forcing in a similar fashion as in perfectly-expanded $M_j = 1.3$ jet [Samimy et al. 2008]. However, it seemed that the jet did not respond to the actuation in the over-expanded $M_j = 1.2$ jet. The generated structures are

visualized based using the Galilean velocity field to find an answer for the reduced effectiveness at the imperfectly-expanded jets.

Visualized large-scale structures are shown in Fig. 3.2.18 for $m = \pm 1$ in the over-expanded $M_J = 1.2$ jet. These structures were also seen in flow visualizations in the earlier research [Samimy et al. 2008]. The generated structures seem as robust and energetic as in the perfectly-expanded jet (Fig. 3.2.15). However, the enhancement in jet growth is not as significant as that in $M_J = 1.3$ jets as seen in Fig. 3.2.10b. The spacing of the structures, the distance between two consecutive spiral shapes, are inversely proportional to St_{DF} numbers ranging from 0.2 to 1.1 as also shown in Fig. 3.2.19. For $m = 0$ and 1, the jet responds in a narrower range of St_{DF} numbers from 0.3 to 0.8 when compared to the perfectly-expanded jet case shown in Fig. 3.2.16. In the baseline jet, some periodic structures are observed, but they appear to be not well organized. However, an image acquired from the proper orthogonal decomposition (not shown here) showed that there are periodic structures in the baseline jet. The periodic structures in the proper orthogonal decomposition images do not necessarily indicate that there are such structures in the flow in steady fashion. This suggests that the spatially periodic structures are generated by a feedback mechanism in the baseline, but that they are not steady in time.

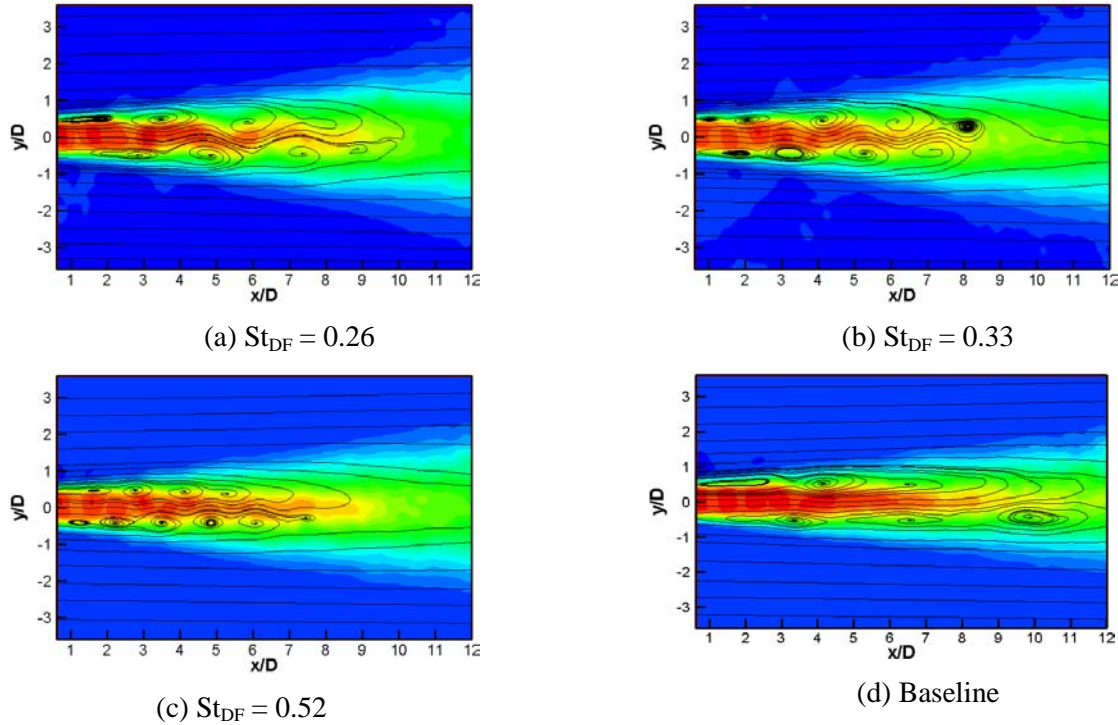


Fig. 3.2.18 Galilean streamlines superimposed on the conditionally-averaged streamwise velocity fields at $m = \pm 1$ in the over-expanded $M_J = 1.2$ jet.

There was a sign of competition for energy between generated structures due to forcing and naturally amplified structures at a St_{DF} about 0.3. The indicator of this competition is the behavior of structure spacing especially for $m = 0$. There is dual spacing of structures around a St_{DF} of 0.3 which suggests competition. The presence of dual spacing at a St_{DF} about 0.3 is observed in Fig. 3.2.18b. In the upstream region, the spacing is very close to that for the baseline. However, the spacing in the downstream region collapses on the relation in Eq. 3, implying that the structures are generated by forcing.

At high St_{DF} 's near 0.8-1.0, the forced structures are small and less energetic so that the naturally amplified structures seem to prevail – inferred from the structure spacing. Unlike in the perfectly-expanded jet, the forced structures need to compete with the naturally amplified structures to survive. As a result of this competition or interaction, it is thought that the vortices are weaker than in the perfectly-expanded jet although it is not readily seen in the visualized structures in Fig. 3.2.18. A careful comparison of Figs. 3.2.15 and 3.2.18 suggests that the generated structures at this St_{DF} are perhaps well organized, but the spanwise dimension is smaller than that observed in the perfectly-expanded $M_J = 1.3$ jet. These findings suggest that the generated structure in the over-expanded jet is less energetic than those in the perfectly-expanded jet. This reduced strength and growth of the structures may be responsible for the decreased effectiveness in mixing enhancement in the over-expanded jet (Fig. 3.2.10).

For the under-expanded $M_J=1.4$ jet, visualized structures at $m = \pm 1$ are shown in Fig. 3.2.20. As was observed in other flow regimes, the spacing and dimension of structures decreased with increasing St_{DF} number. In the baseline jet, there are periodic structures generated by a feedback mechanism as in the over-expanded jet. The pattern of vortical structures in forced cases is very similar to what was seen in the other two flow regimes of $M_J = 1.2$ and 1.3 (Figs. 3.2.15 & 3.2.18). At low St_{DF} 's of 0.13 and 0.26, the spacing in the vicinity of the nozzle exit is smaller than that at far-downstream locations. The spacing in the upstream region is actually very close to that for the baseline. As in the over-expanded jet, this dual spacing in the shear layer suggests that the forced structures need to compete with the naturally amplified structures which can be observed in Fig. 3.2.20f. At moderate St_{DF} numbers of 0.39 and 0.52, only single spacing is seen over the entire streamwise span. A dual spacing is also observed at high St_{DF} numbers about 1.0, but it is not readily observed in Fig. 3.2.20e.

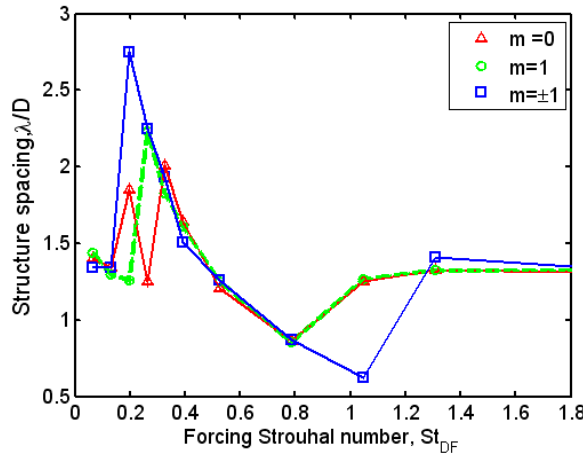


Fig. 3.2.19 Spacing of the structures in $M_J = 1.2$ jets.

Although the generated structures appear to be as energetic as those in the perfectly-expanded case, it is expected that the strength of the generated structures will be less in the under-expanded jets due to competition. As in the over-expanded case, the reduced strength may be partially responsible for the reduced jet growth as shown in Fig. 3.2.12b. At $St_{DF} = 0.26$, the jet responded to the forcing and the generated structures seem to be more energetic compared to other cases shown in the figure. These energetic structures are responsible for better mixing enhancement as shown in Fig. 3.2.12b. At $St_{DF} = 0.39$ and 0.52, the spacing of the generated structures is very close to that of the shock cells. The generated structures are well organized, but it seems that they are not sufficiently energetic to be able to

undulate the jet column significantly, as inferred from the relatively straight jet plume. When the jet is forced at high St_{DF} 's as in Fig. 3.2.20e, the structure spacing is the same as the baseline, but the formation of structures is suppressed by forcing as inferred from the dimension and irregular spacing of the structures. The suppression of naturally amplified structures is most likely responsible for the reduced jet growth and the increased potential core length at high St_{DF} 's (Fig. 3.2.12b).

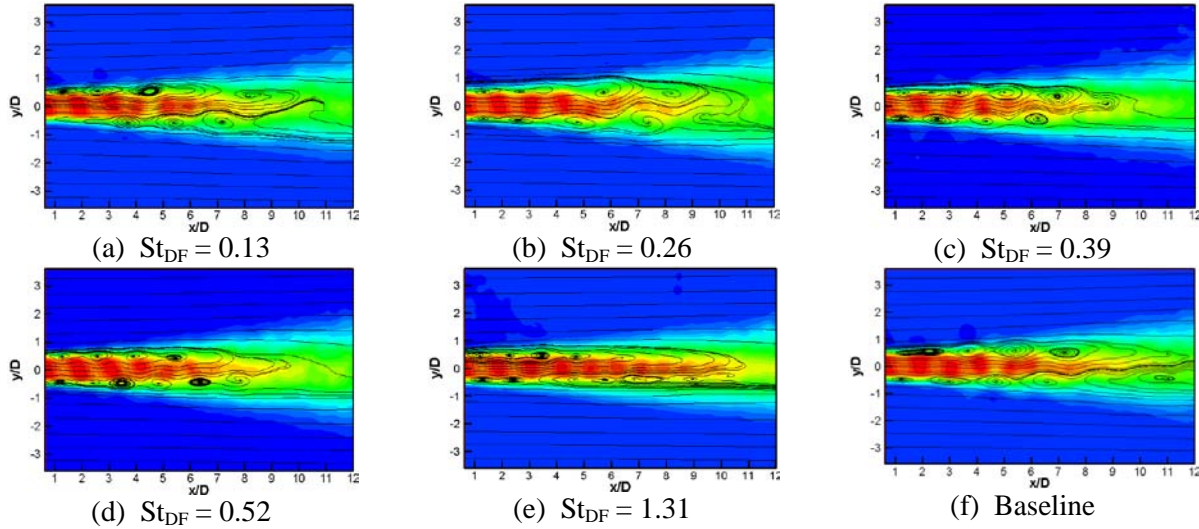


Fig. 3.2.20 Galilean streamlines superimposed on the conditionally-averaged streamwise velocity fields at $m = \pm 1$ in the under-expanded $M_J = 1.4$ jet.

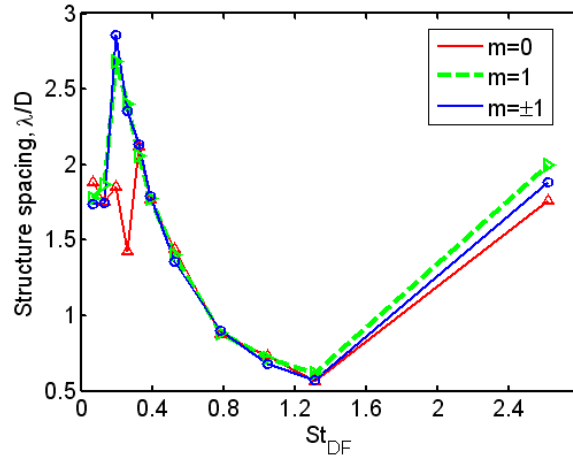


Fig. 3.2.21 Spacing of structures in $M_J = 1.4$ under-expanded jets.

Figure 3.2.21 shows the spacing of periodic structures either forced or naturally amplified. The spacing of generated structures is inversely proportional to St_{DF} numbers ranging roughly from 0.3 to 1.3. For low and high St_{DF} numbers, the structure spacing is the same as that in the baseline jet as was observed in Fig. 3.2.20. In the $M_J = 1.4$ baseline jet, the Strouhal number at the measured fundamental screech frequency (f_s) is about 0.37 ($= f_s D / U_J$) as shown in Fig. 3.2.2. This screech and the periodic structures seen in Fig. 3.2.20f were generated by the feedback mechanism. As in the over-expanded jet,

the initial shear layer at $M_j = 1.4$ is exposed to two sources of perturbation: one is seeded by the plasma actuators and the other is amplified by the flow-acoustic feedback mechanism. Thus, Figures 3.2.20b and 3.2.21 suggest that there is a strong competition for energy between these two sets of structures, especially at St_{DF} numbers near 0.3 and 1.0. When the forced structures are not energetic either due to lack of organization (at low St_{DF} numbers) or small in dimension (at high St_{DF} numbers), the naturally amplified structures prevail over forced structures. It seems that the jet responds either to the forcing by the actuators or to the natural perturbation by the flow-acoustic feedback mechanism. The structure spacing is different from that of the baseline if the jet responds to the perturbation seeded by the actuators.

The jet width for the three baseline/unforced jets is compared as shown in Fig. 3.2.22. The jet width is increased by the naturally amplified structures in the over- or under-expanded baseline jets. Thus, for imperfectly expanded jets, the reduced mixing enhancement over each corresponding baseline jet is partially related to the already enhanced mixing caused by the feedback mechanism (shown in Figs. 3.2.8, 3.2.10, and 3.2.12). At high St_{DF} 's, the jet growth is reduced by forcing at some azimuthal modes (not shown). As discussed earlier, the reduction in jet growth is due to suppression of naturally amplified structures for the imperfectly-expanded jets.

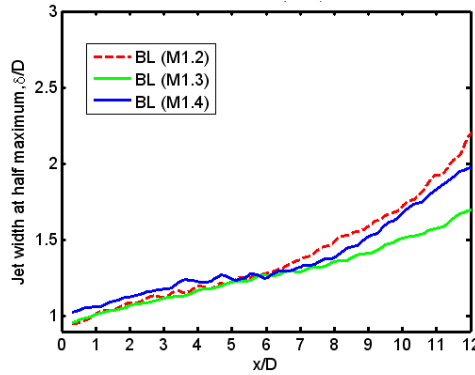


Fig. 3.2.22 Jet width for the three baseline jets.

3.3 Mach 0.9 Heated Subsonic Jet

The performance of plasma actuators in an M_j 0.9 subsonic jet was investigated for stagnation temperature ratio (T_o/T_a) of 1.0, 1.4, and 2.0 at a fixed forcing Strouhal number ($St_{DF} = 0.3$), which is close to the jet preferred instability. The focus in this section is determining whether the performance of the plasma actuators in the heated jet is comparable to the corresponding cold jet for limited azimuthal modes of $m = 0$, 1, and ± 1 . In this section, FWHM indicates the jet width while δ was used in earlier sections.

3.3.1 Mean Flow Results

The mean flow results use centerline Mach number and turbulent kinetic energy as well as jet width as the metrics for mixing enhancement. It should be noted that the plotting markers, created by severely down sampling the data, are for visual identification.

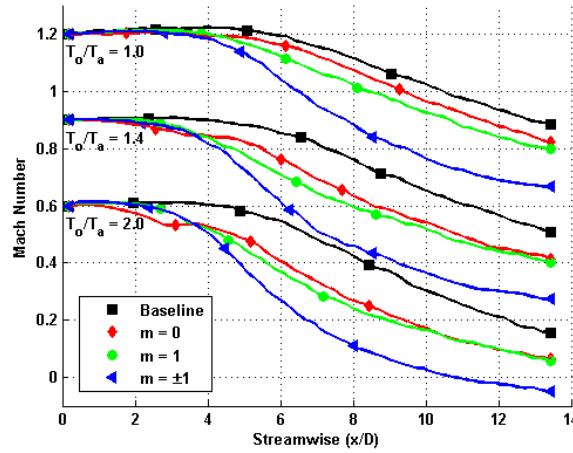


Fig. 3.3.1 Centerline Mach number for jet with various temperatures and forcing azimuthal modes.

Figure 3.3.1 shows the centerline Mach number for all the cases experimented. Mach number for the three temperature ratios is offset in increments of 0.3 to facilitate visual examination. These results show that the jet potential core ends (the centerline Mach number starts dropping) at smaller x/D across all cases as temperature is increased. In all forcing cases, the jet potential core is shortened by forcing, especially for $m = 0$ at higher temperatures, with mode ± 1 consistently producing the greatest centerline Mach number decay rate. It should be noted that the forcing effectiveness, indicated in this figure by the rate of centerline decay, appears to be improving as the temperature is raised. There exists a small, rapid, decay region upstream of $x/D = 4$ for $m = 0$ which becomes stronger as the temperature increases. It is barely observable at $T_o/T_a = 1.4$, but is readily apparent at 2.0. This feature most likely is due to two events. First, Suzuki and Colonius [2006] have shown in a recent work that $m = 0$ mode growth in an unforced jet is significantly more enhanced by heating of the jet than that of modes 1 and 2. Second, the nature of the generated vortex pattern and interaction of coherent vortices in the axisymmetric $m = 0$ case creates self-induction which generates regions of additionally accelerated flow as can be clearly seen in $T_o/T_a = 2.0$ on a streamwise range of 3 to 4 x/D [Kim et al. 2009a]. Additionally, the effectiveness of mode 0 excitation and, to a lesser extent, mode 1 increase significantly in the elevated temperature cases and their downstream centerline Mach number profiles ($x/D > 8$) become similar. These results indicate that mixing enhancement due to forcing is achieved at all temperatures and that mixing enhancement

improves as temperature increases. Additionally, the results indicate a significant change in jet characteristics as a function of temperature supported by the significant changes in $m = 0$ mode response.

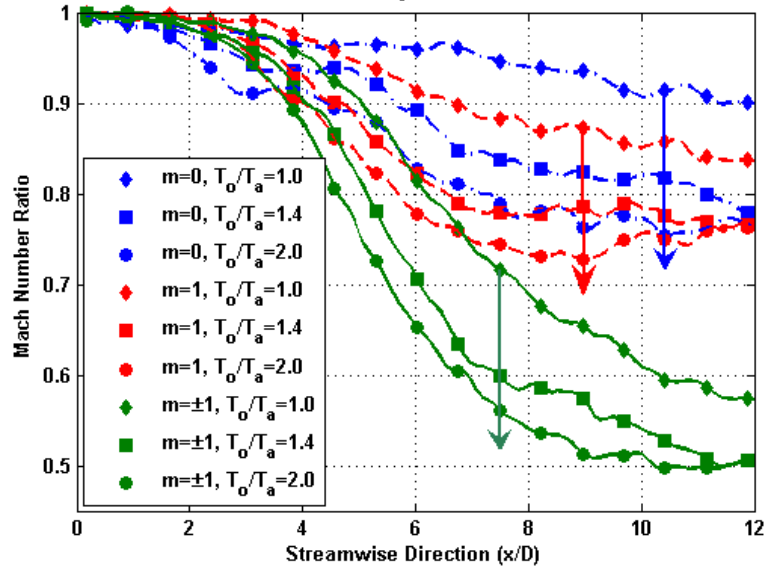


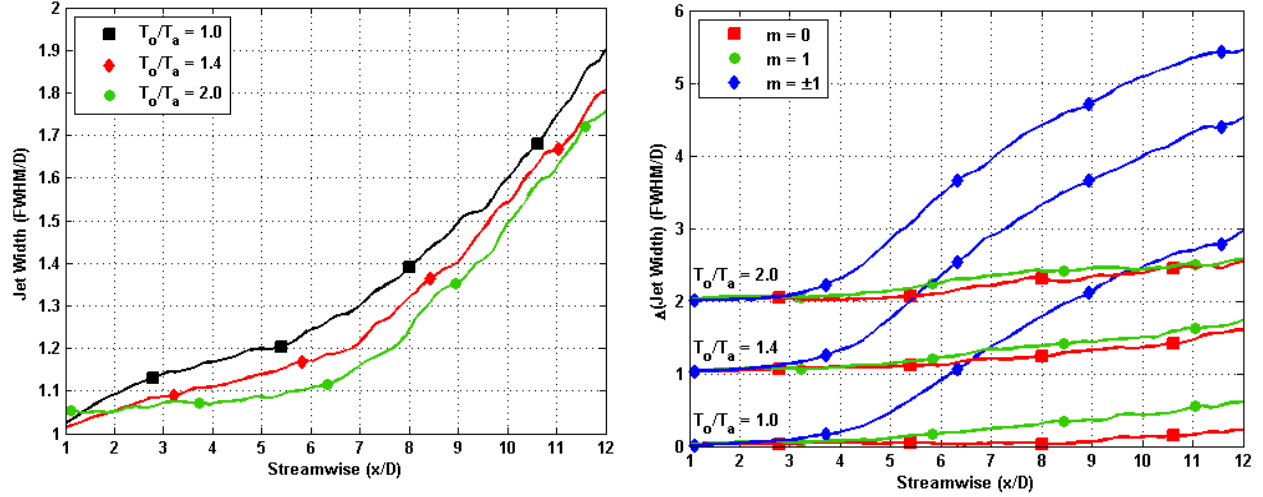
Fig. 3.3.2 Ratio of centerline Mach number for forced jet to the baseline centerline Mach number.

In Fig. 3.3.2, the centerline Mach number for each mode and temperature ratio has been divided by the baseline centerline Mach number at that temperature. This provides a clear view of the profile changes due to excitation (a value of less than one indicates an increase in centerline Mach number decay). In all three forcing cases, a consistent increase in centerline decay is observed. The convergence by $x/D = 12$ of the two elevated temperatures indicates the end of heating effects, due to enhanced mixing and significant entrainment of the ambient air into the jet. This figure eliminates the ambiguity in the previous figure showing definite improvement in control effectiveness across all modes as temperature is increased. It also clearly shows that the $m = \pm 1$ mode is producing the greatest increase in centerline decay rate.

The jet width characteristics are shown in Fig. 3.3.3. From Fig. 3.3.3a, there are a few noticeable changes in the unforced spreading of the jet with temperature. As the temperature is raised, the spreading rate, which is the slope of the curves shown, slows down significantly in early jet development, but becomes similar beyond $x/D \approx 8$. On average, the jet with temperature ratio of 2.0 is about 9% narrower than the unheated jet. At a temperature ratio of 2.0, the jet has no significant spreading until about $x/D = 5$. In all three temperatures, there are two distinct spreading rates. The transition between the two spreading rates occurs between $x/D = 5$ and 7. While the initial spreading rates vary substantially ($\sim 0.03FWHM/x$ with variation of 45%), the second spreading rate ($\sim 0.12FWHM/x$ with variation of 3.5%) is about the same for all three temperatures.

It may be confusing to some readers how the jet potential core can become shorter while the jet is also narrowing. There are several factors which contribute to this result. The shortening of the potential core due to heating has also been reported in Lepicovsky's work [1999]. In this paper, Lepicovsky points out that as temperature increases, kinematic viscosity and jet exit velocity increase. The change in

viscosity affects the growth of the shear layer. The increasing disparity between the core and ambient velocities increases the instability of the shear layer which gives rise to vortices. Secondly, it is well known, but often overlooked, that shear layers do not spread symmetrically about the plane of their origin. The exact nature of the spreading dynamics is beyond the scope of this paper, but the work of Elliott and Samimy [1990] is a representative example of the understanding in this area. Given this asymmetric behavior, it is reasonable to accept that the potential core can shorten while the jet narrows.



a) Jet width in an unforced jet for various temperatures.

b) $\Delta(\text{Jet spreading})$ for various forced cases.

Fig. 3.3.3 Jet full width at half maximum for various conditions.

In Fig. 3.3.3b the appropriate baseline jet width is subtracted from the forced case – the results for temperature ratios of 1.4 and 2.0 are artificially shifted up for visual clarity. It should be noted that, because the $m = \pm 1$ mode is elliptical and the measurement plane is on the major axis of the elliptic jet cross-section, the data collected for this mode exaggerates the increase in spreading compared to the total area of the jet [Kim et al. 2009a or Sec. 3.1]. In the previous work, it is noted that the jet width on the non-flapping axis can be approximated by the unforced width. Consequently the width data for the $m = \pm 1$ mode is corrected to reflect the area of an axisymmetric jet. This correction, known as the equivalent jet width (δ_{eq}), is calculated as $\delta_{eq} = \sqrt{\delta_{Base} \delta_{\pm 1}}$ where “Base” and “ ± 1 ” are the measured unforced and forced widths respectively. The other modes are axisymmetric so this consideration is not necessary. In the unheated jet, modes 0 and 1 have distinct spreading rates, but in the elevated temperature cases, their spreading patterns are very similar. For modes 0 and 1, additional spreading due to forcing is not observed until about $x/D = 5$ or 6 indicating that forcing at these conditions does not have an impact until the jet undergoes the spreading transition observed in the unforced cases. Furthermore, the additional spreading generated by forcing with modes 0 and 1 is fairly minimal. On the other hand, mode ± 1 creates substantial additional spreading with onset occurring at a much lower x/D (~ 3).

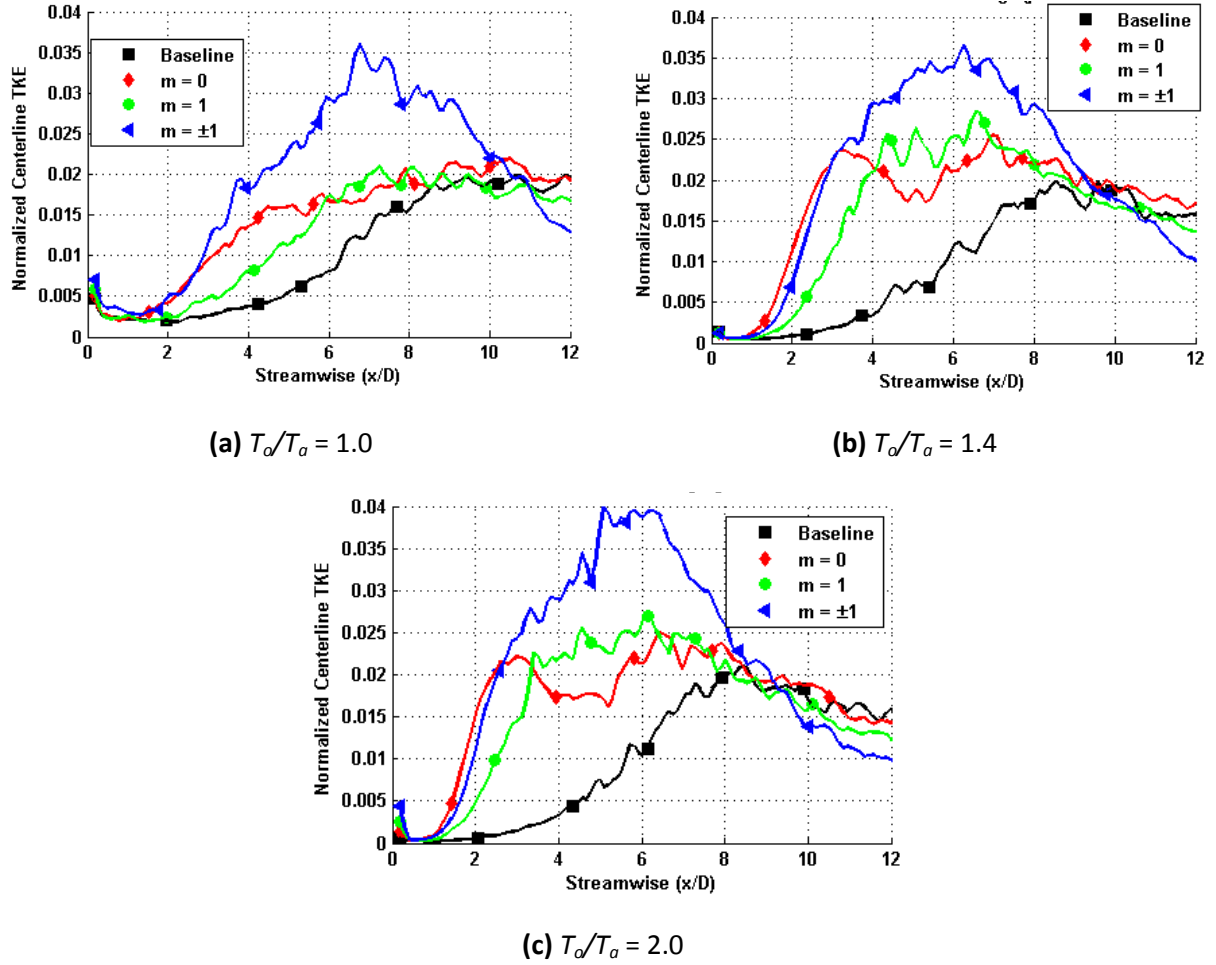


Fig. 3.3.4 Jet centerline turbulent kinetic energy for various temperature ratios and forcing modes.

The normalized TKE results shown in Fig. 3.3.4 reinforce the results observed above. It should be noted that TKE is a two component kinetic energy as only streamwise and normal to streamwise velocity components were measured. All forcing cases show significantly higher TKE growth and they saturate before the baseline case does, with $m = \pm 1$ consistently showing the greatest peak. The $T_o/T_a = 1.0$ case is consistent with results obtained previously at GDTL [Samimy et al. 2007b]. As the temperature is raised, the baseline remains relatively unchanged while the forcing cases grow and saturate more rapidly. There is little change in the $m = 0$ and $m = 1$ modes between 1.4 and 2.0, but $m = \pm 1$ case has a noticeable peak increase. The TKE growth onset becomes more rapid in all forcing cases as temperature increases. The $m = 0$ mode shows two saturation events at elevated temperatures supporting the assertion of the presence of strong, rapidly developing, structures. While the baseline onset does also become more rapid, it is not nearly as dramatic as the forcing cases. These results further support the conclusion that significant mixing enhancement occurs at all temperatures with increased mixing enhancement at higher temperatures.

3.3.2 Conditionally-Averaged Results

Now that the mean flow characteristics have been examined, the structures present in the flow will be discussed in an effort to better understand the effects of forcing on the flow structure in a heated jet and explain the underlying behavior.

Conditional-averaging is conducted using a correlation map to reveal dominant feature of the flow. The conditional-averaging in this section is different from that in earlier sections, but largely very similar. Each image is correlated with all other images. If the structures in the flow are relatively coherent, there will be significant correlation among a subset of the images collected. Once the conditionally-averaged velocity field is generated, various flow analysis methodologies can be applied to examine the structures.

In the data presented in this paper, the fluctuating v -component tended to bring out the most readily identifiable structures so it is used for the correlations. The region of interest is the mixing layer surrounding the jet potential core – thus correlation is performed on a region of typical size -1 to $+1$ y/D by 0 to 4 x/D . A requirement of 10% usage of the data set (typically about 70 fields) for conditional-averaging ensures that the results are converged and the structures analyzed are statistically significant. It should be noted that conditional-averaging of the Baseline (no forcing) velocity fields is considerably less reliable than the forced cases, as the structures in the flow are not sufficiently coherent. While the forced cases tend to satisfy the 10% requirement with a correlation coefficient of ~ 0.55 , the Baseline cases typically only meet the requirement at a value of about 0.22. This is expected since the forcing generates large repeatable structures whereas the Baseline jet possesses large scale but not quite coherent structures.

Figures 3.3.5 and 3.3.6 show the conditionally-averaged streamwise component of velocity. These figures are presented to give a visual sense for the flow before discussing the structures. In the Baseline, small, transverse oscillations in the potential core are just barely observable. The small magnitude of these oscillations indicates a lack of coherence in large-scale structures. The results for each forced case show significant alteration of the jet potential core. In the $m = 1$ mode, there are pronounced, transverse oscillations and the potential core is shortened by about 2 x/D compared to the baseline. The $m = \pm 1$ mode exhibits qualitatively similar results to mode 1, but the oscillation amplitude is greater and the potential core is shortened by 3 x/D . In the $m = \pm 1$ mode, the oscillations are so large that (as seen in Fig. 3.3.5d at $x/D = 3$) the potential core is perturbed entirely to one side of the jet centerline. As was discussed in the mean flow results, the baseline, $m = 1$, and $m = \pm 1$ modes vary only quantitatively as the temperature is raised – the potential core becomes shorter.

The behavior of the $m = 0$ mode is more complex than the others as can be seen in Figs. 3.3.5b and 3.3.6. In the unheated case, there are weak longitudinal variations in the potential core which are accompanied by axisymmetric variation (waists) which is out of phase relative to the longitudinal variations. Referring to the mean flow results, there is almost no change in the length of potential core due to forcing at this mode and temperature (Fig. 3.3.1). As the temperature increases, the amplitudes of both the transverse and longitudinal variations increase. The low velocity waist regions become significantly more pronounced. Additionally, the effect of forcing with this mode on the potential core length increases substantially. Combining inspection of Figs. 3.3.1, 3.3.5b, and 3.3.6, the decrease in potential core length due to $m = 0$ forcing is about: 1, 4, and 4.5 x/D in order of increasing temperature. These results support a significant change in jet characteristics as was discussed in the mean flow results (Fig. 3.3.2).

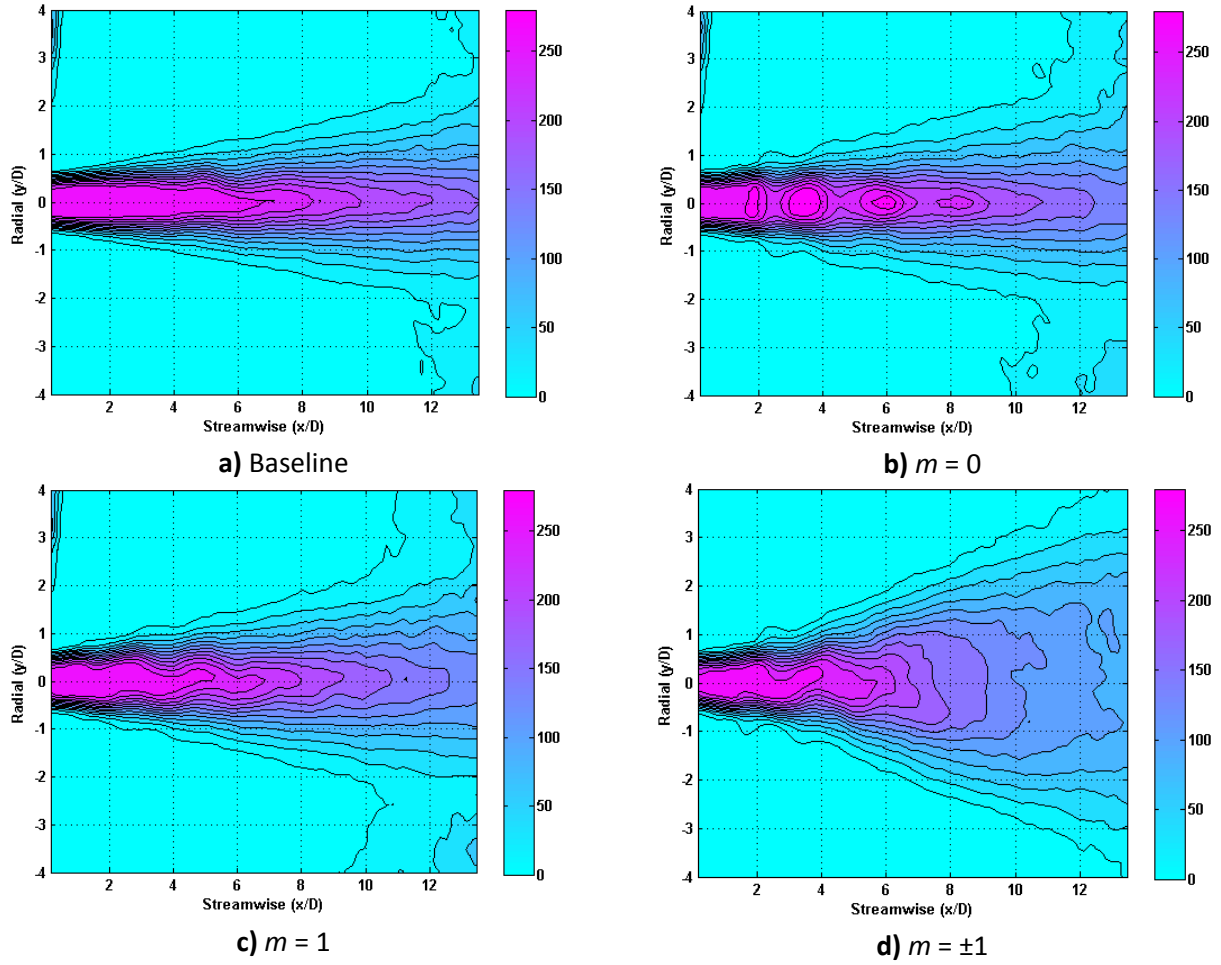


Fig. 3.3.5 Conditionally averaged streamwise velocity fields for $T_o/T_a = 1.0$.

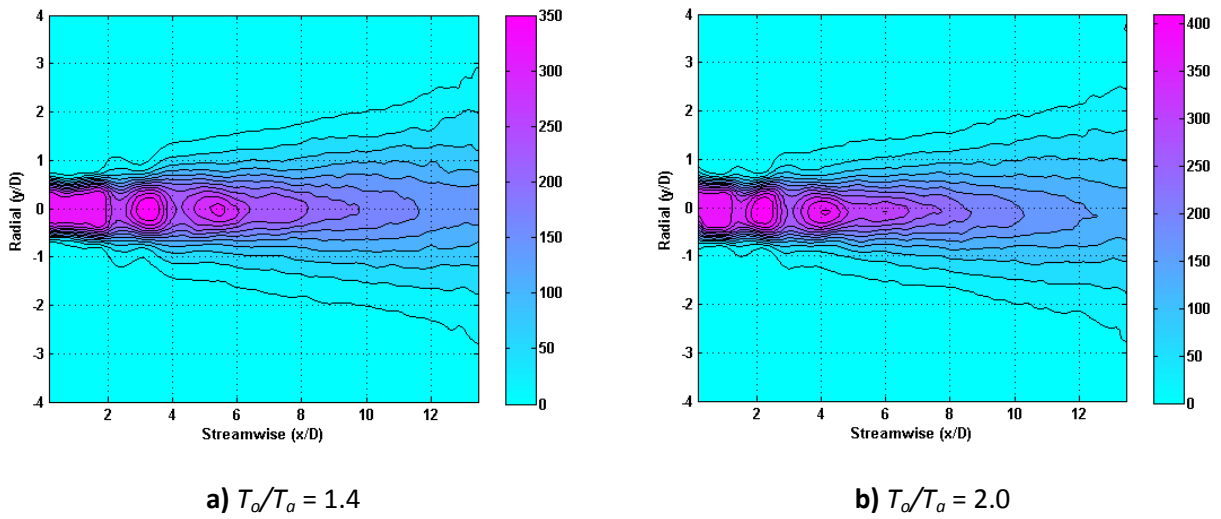


Fig. 3.3.6 Conditionally averaged streamwise velocity fields for $m = 0$.

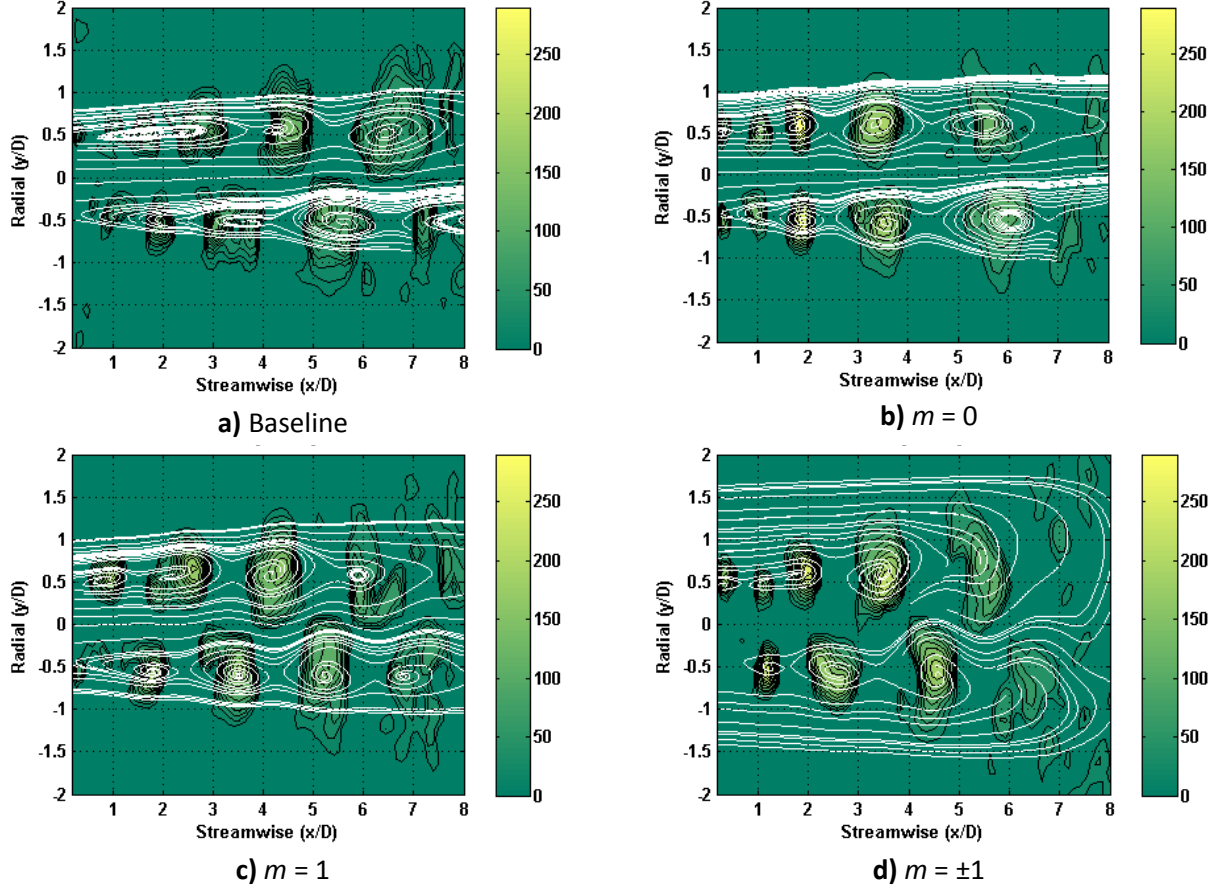


Fig. 3.3.7 Swirling strength (Hz) and Galilean streamlines for $T_o/T_a = 1.0$.

Figures 3.3.7 and 3.3.8 show the conditionally-averaged images using two vortex identification methods. The primary tool used to discuss structures in this paper is known as the swirling strength method – originally developed by Chong et al. [1990]. This vortex identification method uses the imaginary component of the eigenvalues of the velocity gradient tensor to locate regions of rotating fluid while ignoring regions of pure shear. Compared to vorticity, swirling strength is a superior tool in flow structure analysis due to the elimination of sheared flow contributions. For two-dimensional imaging, the essence of this technique is that regions of swirl obey the following condition for the product of the two shear components.

$$u_y v_x < \frac{-(u_x + v_y)^2}{4} \quad (3.3.1)$$

where u and v are the x- and y-components of the velocity, respectively, and a subscript indicates a derivative with respect to that variable. The most important result of this inequality is that the imaginary component of the eigenvalues will be non-zero only if this product is negative, which only occurs in regions where the flow is rotating. The imaginary component is shown as a contour plot in the following figures and has units of inverse seconds – swirling strength is a measure of the rotational rate of the fluid structure.

The peaks in swirling strength are used to calculate several empirical values for describing the structures in the flow – these values are shown in Table 4. The peak values for the set of structures in a given plot are averaged to produce the Peak Swirling Strength (PSS). The U-component of the velocity at each peak is averaged to determine the average convective velocity (U_C). This convective velocity is used to determine the Galilean decomposition and to produce the streamlines shown in the figures. Lastly, the peak coordinates are used to calculate the spacing between structures.

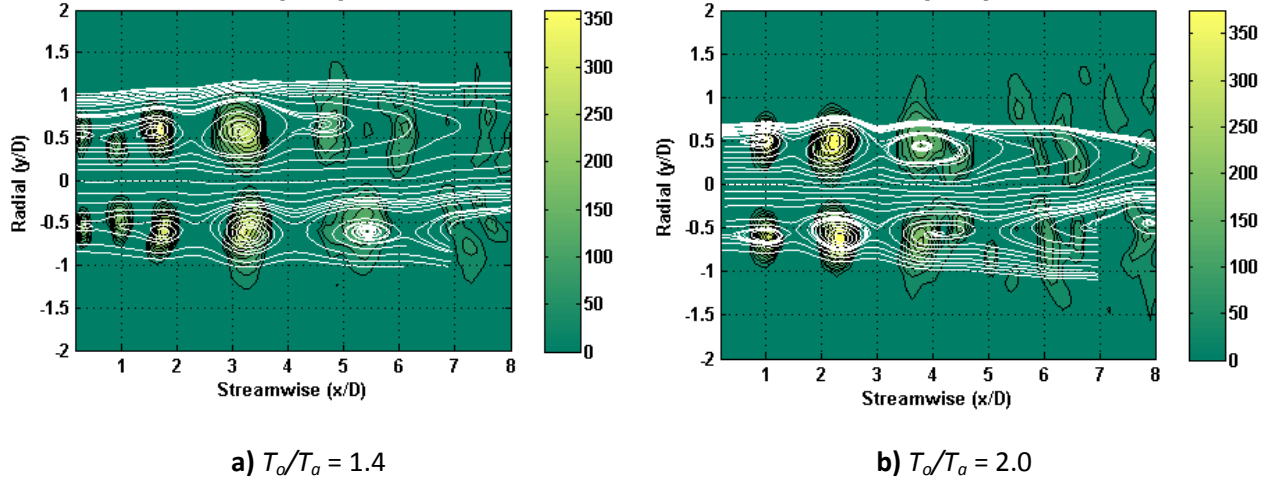


Fig. 3.3.8 Swirling strength (Hz) and Galilean streamlines for $m = 0$ in heated jet.

The flow structure plots for the unheated jet are shown in Fig. 3.3.7. The Galilean streamlines show good agreement with the identified swirling regions, and also provide additional information on the shape of the structures. Furthermore, the streamlines indicate that some swirling regions are not vortex centers. These regions are most likely non-physical artifacts of finite PIV grid resolution and the low number of images used in conditional-averaging. As expected, the structures in the forced cases are more organized, and are apparent almost immediately downstream of nozzle exit. Baseline structures are less organized, flattened, and don't become significantly organized until farther downstream compared to those in the forced cases. The symmetric nature of mode 0 is immediately apparent. The other two modes have a similar appearance, but their distinctions are borne out by the data in Table 4. The similarity of the forced case structure spacing to the unforced cases shows that the frequency chosen is indeed close to the natural instability frequency of the jet. All of the forced cases have higher PSS than the baseline. Mode ± 1 is observed to have the strongest PSS.

The similarity of the baseline and $m = 1$ structure patterns warrants additional discussion. First, as mentioned above, the correlation level of the baseline velocity field (~ 0.22) is much lower than forced cases (~ 0.55) so the structures analyzed are less representative of the average jet behavior. Next, previous work by Tinney et al. [2008] on the azimuthal mode composition of an unforced Mach 0.85 jet shows that low order helical modes are dominant in the jet. All azimuthal modes produce a structure pattern which is either staggered or symmetric – any single helical mode will produce a staggered structure pattern. Since conditional-averaging will seek out a pattern no matter how weak, it is reasonable to expect the algorithm to find one of these patterns. Additionally, in a study conducted by Moore [1977] in high subsonic jets,

large scale structures in an unforced jet were observed. By synchronizing schlieren images with the arrival of structures on one side of the jet as determined by a microphone, he was able to create a conditionally averaged image of the jet structures. What he found was that the structures on the other side of the jet were absent from this averaged image. When he examined individual frames he saw that the structures were sometimes symmetrically arranged and in other frames they were staggered. Since the conditional-averaging used in the present paper operates over the whole jet cross-section, it makes sense that one structural pattern would be isolated. Lastly, while the baseline structures shown in Fig. 3.3.7 may not be representative of the jet in an average sense, they are (by the nature of the conditional-averaging routine) representative of the strongest structures present in the jet.

As before, the mode 0 case is presented alone in Fig. 3.3.8 due to the general similarity of other cases over the temperature range. Comparing Fig. 3.3.7b and Fig. 3.3.8, it is apparent that, as the temperature increases, the organized structures become confined to a smaller region closer to the nozzle exit. The decreasing region of organized structures reinforces the conclusions drawn from the mean flow and velocity results discussed in the previous sections – a significant change takes place in jet characteristics with increasing temperature.

When the temperature ratio is raised to 1.4, there are several observable changes in the flow structures. The basic flow patterns of each of the four cases stay the same, but the amplitude, spacing, and streamwise extent of the structures change. The PSS increases for each case. The PSS of the forced cases continues to be significantly higher than the baseline case. The most interesting change is that the PSS of mode 0 is now slightly greater than that of mode ± 1 . At the temperature ratio of 2.0, the same trends observed in 1.4 continue and now mode 0 clearly has the largest PSS.

The behavior of the convective velocity merits some discussion. According to theoretical equations for convective velocity such as those cited in Thurow et al. [2008], the non-dimensionalized convective velocities for the three temperature ratios under discussion are: 0.53, 0.48, and 0.44 (in ascending order of temperature). While there is fairly good agreement with theory in the unheated cases, there is a significant departure from theory in the elevated cases. According to theory, the ratio of convective velocity to exit velocity should decrease with increasing temperature, but the data collected shows that this ratio is increasing, except for the $m = 0$ case. Soteriou and Ghoniem [1995] observed that convective velocity decreased as density ratio decreased. In those experiments, the velocity ratio (jet velocity to ambient velocity) was constant (~ 1.5). Performing a linear fit with temperature ratio as the independent variable, the slope of the velocity ratio, using a small constant velocity for the ambient flow, in these experiments (~ 23) is greater than the slope of the ratio of convective velocity to the ambient (~ 15). It is concluded that the convective velocity is, qualitatively, in agreement with Soteriou and Ghoniem's observations. The decrease in non-dimensionalized convective velocity in mode 0 at a temperature ratio of 1.4 cannot be explained at this time, but a likely suspect is the significant increase in structure strength. Unfortunately, the extreme environment of heated, high Reynolds number jets makes it difficult to acquire data on this subject, which limits the number of papers published in the literature on the subject and, consequently, the conclusions which can be drawn here.

The trends in PSS are made clearer by non-dimensionalizing the data. Generally, the strength of the vortices is directly correlated to the jet exit velocity as evidenced by the consistency of the non-dimensional PSS. This indicates that the forcing mechanism on average is not changing as the

temperature changes – at least for this Strouhal number. The notable exception to this consistency is mode 0. At a temperature ratio of 1.0, mode 0 strength is comparable to mode 1. At the temperature ratio 1.4, the strength of mode 0 has risen and is comparable to mode ± 1 . This suggests a change in the receptivity of the jet to forcing at this mode and Strouhal number. As was discussed previously, increasing mode 0 energy with increasing temperature relative to other modes has been observed [Suzuki and Colonius 2006] so it is reasonable to expect an increase in structure strength.

Table 4 Structure information for all cases.

Mode	T_o/T_a	U_c/U_j	Conditionally Averaged: λ/D	Peak Swirling Strength (Hz)	$\frac{D * PSS}{U_j}$
Baseline	1.0	0.57	1.61	119	0.011
Baseline	1.4	0.58	1.55	130	0.010
Baseline	2.0	0.55	1.36	168	0.011
0	1.0	0.51	1.55	177	0.016
0	1.4	0.45	1.46	286	0.022
0	2.0	0.54	1.36	324	0.020
1	1.0	0.52	1.67	175	0.016
1	1.4	0.52	1.52	221	0.017
1	2.0	0.60	1.46	249	0.016
± 1	1.0	0.54	1.65	221	0.020
± 1	1.4	0.56	1.62	270	0.020
± 1	2.0	0.59	1.49	294	0.019

A decrease in structure spacing is expected because of the changing ratio of convective velocity to exit velocity $\lambda = U_c D / (U_j St_{DF})$. Using the theoretical values for convective velocity, the structure spacing is 1.66, 1.50, and 1.36 x/D in order of increasing temperature ratio. While at first this may look promisingly related to the results in Table 4, the data resolution must be remembered. The range of variation in the data is 0.31 x/D , but the data resolution is 0.11 x/D . Due to low resolution relative to the range of variation in structure spacing, the only valid conclusion is that the structure spacing is approximately the same for all cases. The results for the M_j 1.3 unheated jet confirms that the structure spacing is almost the same for all azimuthal modes when the forcing frequency is the same (Fig. 3.2.16).

3.4 Mach 1.65 Cold Jet

Limited experiments are conducted for M_j 1.65 unheated jets from contoured and conical nozzles (referred as contoured and conical jet, respectively). The focus of this section is to find whether the LAFPA's have control authority in a supersonic jet with a high jet Mach number ($M_j = 1.65$) and in a shock containing conical jet. Based on the results in M_j 0.9 and 1.3 jets, azimuthal mode and St_{DF} 's are limited to $m = \pm 1$ and $St_{DF} = 0.18, 0.29, 0.47$, and 1.4. Note that the results for M_j 1.65 jets are very preliminary and investigation is still underway.

Shown in Fig. 3.4.1 are Mach number and TKE along the centerline of M_j 1.65 contoured and conical jets. The centerline Mach number for the contoured jet shows slight undulation although it was operated in the design condition as in the M_j 1.3 perfectly expanded jet (Sec. 3.2). For the conical jet (Fig. 3.4.1c), the centerline Mach number undulates significantly due to stronger shock cell trains in the jet plume compared to the contoured jet as manifested in schlieren images in Fig. 3.4.2. The strong shock trains are expected since the conical nozzle has a sharp throat and a conical diverging section.

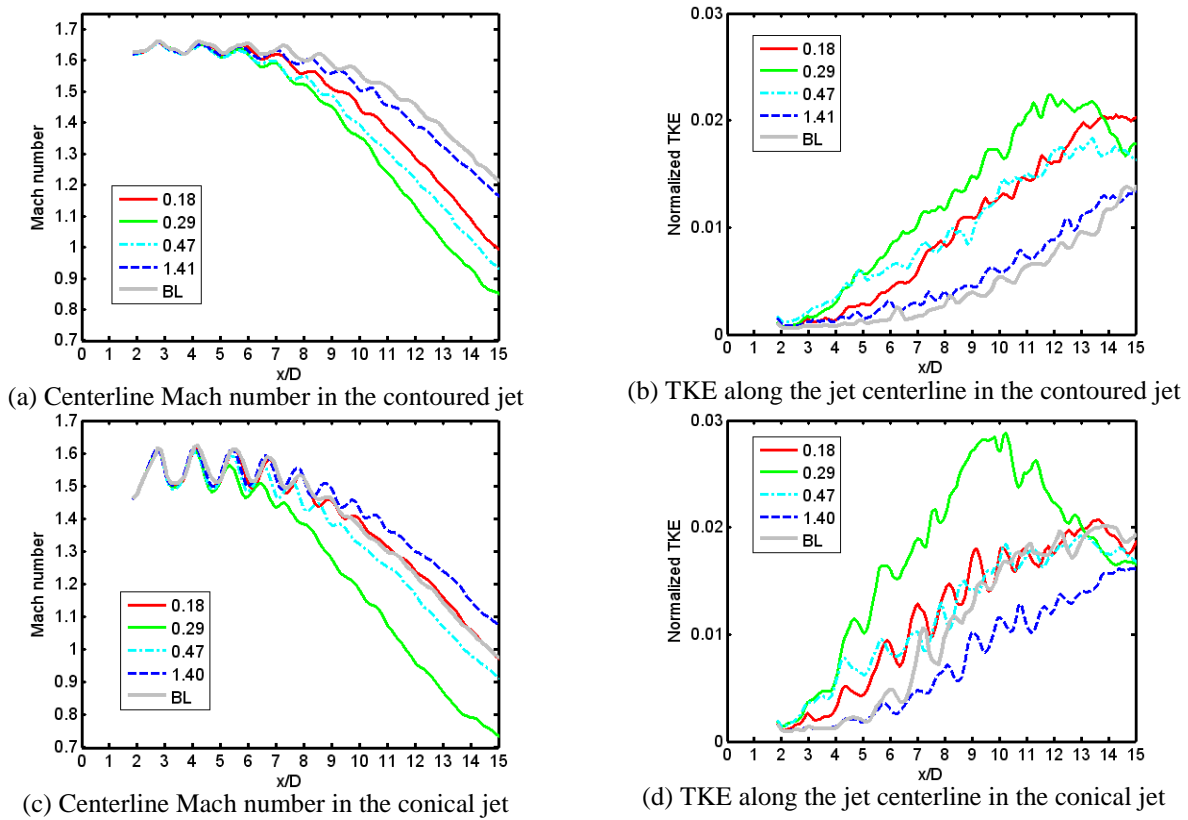
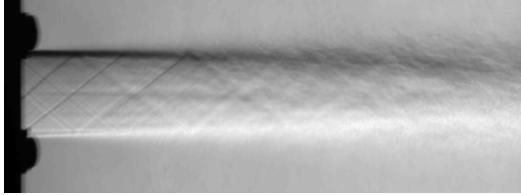


Fig. 3.4.1 Mach number and TKE along the jet centerline in $m = \pm 1$.

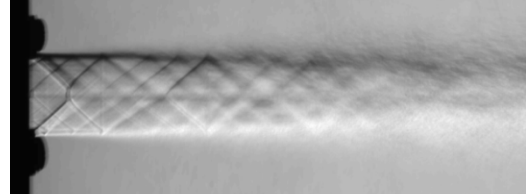
It seems that the centerline Mach number decay in the M_j 1.65 contoured jet is qualitatively similar to that in M_j 0.9 subsonic (Fig. 3.1.7) and M_j 1.3 perfectly-expanded (Fig. 3.2.8) jets, although comparison is not straightforward since the potential core length and Mach number are not the same. The optimum St_{DF} , producing maximum jet spreading, is about 0.3 similar to those in M_j 0.9 and 1.3 jets. The effects of forcing decrease as the St_{DF} increases – also similar to what was observed in M_j 0.9 and 1.3 jets. The TKE level significantly increases at low St_{DF} 's, but the saturated TKE level is much lower than those

observed in M_J 0.9 and 1.3 jets (Figs. 3.1.9 and 3.2.13, respectively). This implies that the forcing in M_J 1.65 contoured jet is slightly less effective than that in low M_J jets.

It is expected that forcing in the M_J 1.65 conical jet to be similar to that in M_J 1.2 overexpanded and M_J 1.4 underexpanded jets (Sec. 3.2), since there will be naturally-amplified structures in the M_J 1.65 conical jet as in the over- and under-expanded jets. In M_J 1.2 overexpanded and M_J 1.4 underexpanded jets, the centerline Mach number decay was not enhanced by forcing (Figs. 3.2.10 and 3.2.12). However, the centerline Mach number decay is significantly enhanced in the M_J 1.65 conical jet, especially at $St_{DF} = 0.29$ (Fig. 3.4.1c). As a result, the TKE level is also significantly increased as shown in Fig. 3.4.1d. The effects of forcing at other St_{DF} 's are limited or minimal as seen in centerline Mach number and TKE. At a high St_{DF} , the centerline Mach number decay is retarded and TKE level is reduced by forcing. Again, this is similar to what was observed in M_J 1.2 overexpanded and M_J 1.4 underexpanded jets (Sec. 3.2). This similarity suggests that the forced structures prevail at intermediate St_{DF} 's while naturally-amplified structures do at low and high St_{DF} 's as can be inferred from Figs. 3.2.19 and 3.2.21. The competition between these two types of structures seems to be responsible for the reduced effectiveness of forcing in the conical jet.



(a) Contoured jet



(b) Conical jet

3.4.2 Time-averaged schlieren images for the baseline/unforced jets.

4. CONCLUDING REMARKS

Active flow control of jets with Localized Arc Filament Plasma Actuators (LAFPA) was conducted over a wide range of the fully expanded jet Mach numbers (M_j). The jet Mach numbers covered in the present research are 0.9 (with a converging nozzle), 1.2 (overexpanded), 1.3 (perfectly expanded), and 1.4 (underexpanded) with a design Mach number 1.3. Additionally, limited experiments were carried out for an $M_j = 1.65$ perfectly-expanded jet with both contoured and conical nozzles. The exit diameter is 2.54 cm (1 inch) for all cases and eight LAFPA are equally distributed on the perimeter of a boron nitride nozzle extension. The performance of LAFPA was evaluated using the centerline Mach number decay, jet width and TKE developments, calculated from two-dimensional PIV results.

The jet spreading was strongly dependent on duty cycle, forcing frequency, and azimuthal modes. The effects of duty cycle was investigated at $m = \pm 1$ for several forcing frequencies in M_j 0.9 jet. At each fixed forcing frequency, the maximum jet spreading occurred at the smallest duty cycle producing stable plasma arc (referred as optimum duty cycle). A relationship between the optimum duty cycle and forcing frequency was determined from the extensive results in the M_j 0.9, and this relation was used for all experiments. In M_j 0.9 subsonic and M_j 1.3 perfectly-expanded jets, very extensive experiments were conducted to find the effects of forcing frequency and azimuthal modes. The forcing Strouhal number ranged from 0.09 to 3.0 and the azimuthal modes investigated were $m = 0 - 3, \pm 1, \pm 2$, and ± 4 , only available modes with eight actuators. The performance of LAFPA was also dependent on the stagnation temperature of the jet and jet Mach number. The effects of stagnation temperature were investigated for 1.0, 1.4, and 2.0 the ambient temperature only in M_j 0.9 jet for very limited azimuthal modes and St_{DF} . In an M_j 1.65 perfectly-expanded jet, the control authority of LAFPA was investigated for only $m = \pm 1$ and $St_{DF} \sim 0.3$.

The jet spreading increased with decreasing duty cycle as long as there were a minimal number of misfires in the plasma actuators. Thus, the optimum duty cycle for each forcing frequency was determined to be the lowest value which ensured stable plasma generation. Extensive experiments in M_j 0.9 subsonic and 1.3 perfectly-expanded supersonic jets showed that the jet spreading was significantly enhanced reaching the maximum at about $St_{DF} = 0.3$ for most azimuthal modes. The most and least effective azimuthal modes were $m = \pm 1$ and ± 4 respectively. The results also showed that the effects of forcing were very similar in M_j 0.9 subsonic and 1.3 perfectly-expanded supersonic jets in a qualitative sense. The generated structure spacing was solely determined by forcing frequency, while the strength and pattern of structures depended on both forcing frequency and azimuthal mode.

The turbulent kinetic energy along the jet centerline also increased significantly near $St_{DF} = 0.3$ for most azimuthal modes. The trend of TKE amplification was similar to that of centerline Mach number decay, implying more amplification for enhanced jet spreading. Thus the maximum TKE amplification was observed in $m = \pm 1$ and at a St_{DF} near 0.3.

The results in the heated M_j 0.9 jet showed that the effects of forcing increase with increasing stagnation temperature. In addition, the jet spreading in $m = 0$ increased relatively more significantly and was comparable to that in $m = 1$ at an elevated stagnation temperature while it was one of the less effective modes in an unheated jet. Possible reasons for the improved actuation effectiveness are discussed

In off-design conditions of $M_J = 1.2$ (overexpanded) and 1.4 (underexpanded), the forcing was less effective compared to the perfectly-expanded case of $M_J = 1.3$. Flow visualization, via Galilean streamlines, shows that there are naturally-amplified flow structures (generated by a natural feedback mechanism) in addition to the structures generated by forcing, especially at low and high forcing Strouhal numbers. The competition of energy between these two structures seemed to be responsible for the reduced effectiveness of forcing.

The performance of LAFPA's in a high M_J supersonic jet ($M_J = 1.65$) was investigated at several St_{DF} 's near 0.3 for $m = \pm 1$. The results showed slightly reduced forcing effectiveness at this high jet Mach number compared to those in M_J 0.9 and 1.3 jets. It has not been determined if the reduction in effectiveness is due to a lack of LAFPA control authority or increased flow compressibility.

REFERENCES

- Ahuja, K. K., Lepicovsky, J. C. K., Tam, W., Morris, P. J., and Burrin, R. H., "Tone-Excited Jet: Theory and Experiments," NASA CR 3538, 1982.
- Ahuja, K. K., Lepicovsky, J., and Brown, W. H., "Some Unresolved Questions on Hot-Jet Mixing Control Through Artificial Excitation," AIAA Paper 1986-1956, 1986.
- Bechert, D. W., and Stahl, B., "Excitation of Instability Waves in Free Shear Layers. Part 2. Experiments," J. Fluid Mech. **186**, 63, 1988.
- Bridges, J. and Wernet, M.P., "Turbulence Measurements of Separated Flow Nozzles with Mixing Enhancement Features," AIAA Paper No. 2002-2484, 2002.
- Bridges, J., "Effect of Heat on Space-Time Correlations in Jets," AIAA Paper No. 2006-2534, 2006.
- Cho, S.K., Yoo, J.Y., and Choi, H., "Vortex pairing in an axisymmetric jet using two-frequency acoustic forcing at low to moderate Strouhal numbers," Experiments in Fluids, Vol. 25, pp. 305-315, 1998.
- Chong, M. S., Perry, A. E., and Cantwell, B. J., "A general classification of three-dimensional flow fields," Phys. Fluids A **2** (5), 765, 1990.
- Cohen, J. and Wygnanski, I., "The evolution of instabilities in the axisymmetric jet. Part 1 the linear growth of disturbances near nozzle," J. Fluid Mech. **176**, 191, 1987.
- Corke, T.C., Shakib, F. and Nagib, H.M., "Mode selection and resonant phase locking in unstable axisymmetric jets," Journal of Fluid Mechanics, Vol. 223, pp. 253-311, 1991.
- Corke, T.C. and Kusek, S.M., "Resonance in axisymmetric jets with controlled helical-mode input," Journal of Fluid Mechanics, Vol. 249, pp. 307-336, 1993.
- Crow, S.C. and Champagne, F.H., "Orderly Structure in Jet Turbulences," Journal of Fluid Mechanics, Vol. 48, pp. 547-591, 1971.
- Chong, M. S., Perry, A. E., and Cantwell, B. J., "A general classification of three-dimensional flow fields," Phys. Fluids A **2** (5), 765, 1990.
- Elliott, G. S. and Samimy, M., "Compressibility effects in free shear layers," Phys. Fluids A **2** (7), 1231, 1990.
- Freymuth, P., "On Transition in a Separated Laminar Boundary Layer," J. of Fluid Mech., V. 25, pp. 683-704, 1966.
- Ginevsky, A.S., Vlasov, Y.V., and Karavosov, R.K., *Acoustic Control of Turbulent Jets*, Springer-Verlag, Germany, 4-5, 2004.
- Gutmark, E. and Ho, C.M., "Preferred Modes and the Spreading Rate of Jets," Phys. Fluids, Vol. 26, No. 10, pp. 2932-2938, 1983.
- Ho, C. M., Hsiao, F. B., "Evolution of coherent structures in a lip jet," Structure of Complex Turbulent Shear Layers, ed. R. Dumas, L. Fulachier, pp. 121-136. Berlin/Heidelberg/New York : Springer, 1983.
- Ho, C-M, and Huerre, P., "Perturbed Free Shear Layers," *Ann. Rev. Fluid Mech.*, Vol. 16, pp. 365-424, 1984.
- Huerre, P. and Monkewitz, P. A., "Local and Global instabilities in spatially developing flows," *Ann. Rev. Fluid Mech.* **22**, 473, 1990.
- Jendoubi, S. and Strykowski, P. J. "Absolute and Convective Instability of Axisymmetric Jets with External Flow," Phys. Fluids **6** (9), 3000, 1994.

Kastner, J, Kim, J.-H., and Samimy, M., "Toward Better Understanding of Far-Field Radiated Noise Mechanisms in a High Reynolds Number Mach 0.9 Axisymmetric Jet," AIAA Paper No. 2008-0007, January 2008.

Kearney-Fischer, M., Kim, J.-H., and Samimy, M., "Control of a High Reynolds Number Mach 0.9 Heated Jet Using Plasma Actuators," *Physics of Fluids*, Vol. 21, No. 9, pp. 095101-1 to 095101-14, 2009.

Kibens, V., "Discrete Noise Spectrum Generated by Acoustically Excited Jet," *AIAA Journal*, Vol. 18, No. , 434-441, 1980.

Kim, J.-H., Kastner, and Samimy, M., "Active Control of High Subsonic Jets," *AIAA Journal*, Vol. 47, No. 1, 116-128., 2009a.

Kim, J.-H. and Samimy, M., "Effects of Active Control on the Flow Structure in a High Reynolds Number Supersonic Jet, Vol. 1, No. 2, 99-117, 2009b.

Kline, S. J. and Robinson, S. K., "Quasi-coherent structures in the turbulent boundary layer. I - Status report on a community-wide summary of the data," *Near-wall turbulence : 1988 Zoran Zaric Memorial Conference*, Edited by S.J. Kline, N.H. Afgan, 1990.

Konstantinidis, E., Balabani, S., and Yianneskis, M., "Conditional averaging of PIV plane wake data using a cross-correlation approach," *Experiments in Fluids*, Vol. 39, pp. 38-47, 2005.

Lepicovsky, J., "An Experimental Study of Tone-Excited Heated Jets," *J. Propuls. & Power* **2** (2), 149, 1986.

Lepicovsky, J., "Effects of Nozzle Exit Boundary-Layer Conditions on Excitability of Heated Free Jets," *AIAA J.* **27** (6), 712, 1989.

Lepicovsky, J. "An experimental investigation of nozzle exit boundary layers of highly heated free jets," *ASME Paper* 1990-gt-255, 1990.

Lepicovsky, J., "Experimental research on mixing enhancement in heated free jet flows," *ASME Paper* FEDSM99-7247, 1999.

Lesshafft, L., Huerre, P., and Sagaut, P., "Frequency selection in globally unstable round jets," *Phys. Fluids* **19**, 054108, 2007.

Michalke, A., "On Spatially Growing Disturbances in an Inviscid Shear Layer," *Journal of Fluid Mechanics*, Vol. 23, pp. 521-544, 1965.

Michalke, A., "Instability of compressible circular free jet with consideration of the influence of the jet boundary layer thickness," *NASA TM* 75190, 1977.

Monkewitz, P., Bechert, D., Barsikow, B., and Lehmann, B., "Self-excited oscillations and mixing in a heated round jet," *J. Fluid Mech.* **213**, 611, 1990.

Moore, C. J., "The role of shear-layer instability waves in jet exhaust noise," *J. Fluid Mech.* **80** (2), 321, 1977.

Petitjean, B.P., McLaughlin, D.K., and Morris, P.J., "An Experimental Investigation of Density Gradient Fluctuations in High-Speed Jets Using Optical Deflectometry," *AIAA Paper* No. 2006-2533, 2006.

Plaschko, P., "Helical instabilities of slowly divergent jets," *Journal of Fluid Mechanics*, Vol. 92, p. 209-215, 1979.

Robinson, S. K., Kline, S. J., and Spalart, P. R., A review of quasi-coherent structures in a numerically simulated turbulent boundary layer, *NASA technical memorandum*, 102191, 1989.

Samimy, M., J., Kim, Kastner, J.-H., Adamovich, I., and Utkin, Y., "Active Control of a Mach 0.9 Jet for Noise Mitigation Using Plasma Actuators," *AIAA Journal*, Vol. 45, No. 4, pp. 890-901, 2007a.

Samimy, M., Kim, J.-H., Kastner, J., Adamovich, I., and Utkin, Y., "Active Control of High Speed and High Reynolds Number Jets Using Plasma Actuators," *Journal of Fluid Mechanics*, Vol. 578, pp. 305-330, May 2007b.

Soteriou, M. C., and Ghoniem, A. F., "Effects of the Free-Stream Density Ratio on Free and Forced Spatially Developing Shear Layers," *Phys. Fluids* **7** (8), 2036, 1995.

Strykowski, P. J., and Russ, S., "The effect of boundary-layer turbulence on mixing in heated jets," *Phys. Fluids A* **4** (5), 865, 1992.

Suzuki, T., and Colonius, T., "Instability waves in a subsonic round jet detected using a near-field phased microphone array," *J. Fluid Mech.* **565**, 197, 2006.

Tinney, C. E., Glauser, M. N., and Ukeiley, L. S., "Low-dimensional characteristics of a transonic jet. Part 1. Proper orthogonal decomposition," *J. Fluid Mech.* **612**, 107, 2008.

Thurrow, B. S., Jiang, N., Kim, J.-H., Lempert, W., and Samimy, M., "Issues with measurements of the convective velocity of large-scale structures in the compressible shear layer of a free jet," *Phys. Fluids* **20**, 066101, 2008.

Troutt, T.R. and McLaughlin, D.K., "Experiments on the Flow and Acoustic Properties of a Moderate-Reynolds Number Supersonic Jet," *Journal of Fluid Mechanics*, Vol. 116, pp. 123-156, 1982.

Wernet, J. H. and Wernet, M. P., "Stabilized Alumina/Ethanol Colloidal Dispersion for Seeding High Temperature Air Flows," NASA technical memorandum, 106591, 1994.

Zaman, K.B.M.Q. and Hussain, A.K.M.F., "Turbulence Suppression in Free Shear Flows by Controlled Excitation," *J. Fluid Mechanics*, Vol. 103, 1981, pp. 133-159.